UNIVERSITY OF CALIFORNIA,
IRVINE

Development of optical Doppler interferometry for the visualization of ocular elasticity and ciliary activity

DISSERTATION

submitted in partial satisfaction of the requirements
for the degree of

DOCTOR OF PHILOSOPHY

in Biomedical Engineering

by

Youmin He

Dissertation Committee:
Professor Zhongping Chen, Chair
Professor William Tang
Professor Matthew Brenner

2019

TABLE OF CONTENTS

LIST OF FIGURES

Page

LIST OF TABLES

Page

TABLE OF ABBREVIATIONS

OCT	Optical coherence tomography
OCE	Optical coherence elastography
SEIM	Spectrally-encoded interferometric microscopy
US	Ultrasound
AMD	Age-related macular degeneration
CT	Computed tomography
MRI	Magnetic resonance imaging
TDOCT	Time domain optical coherence tomography
FDOCT	Fourier domain optical coherence tomography
SSOCT	Swept source optical coherence tomography
SDOCT	Spectrometer based optical coherence tomography
FFT	Fast Fourier Transform
2-D	Two-dimensional
3-D	Three-dimensional
GRIN	Gradient refractive index
FWHM	Full width at half maximum
SNR	Signal to noise ratio
fps	frames per second
RPE	Retinal pigment epithelium
ARF	Acoustic radiation force
SLD	Superluminescent diode
CMOS	Complementary metal-oxide-semiconductor

CCD	Charge-coupled device
GM	Galvanometer mirrors
PSF	Point spread function
RFA	Radiofrequency amplifier
FG	Function generator
MPE	Maximum permissible exposure
PBS	Phosphate-buffered saline
H&E	Hematoxylin and eosin
LED	Light-emitting diode
MI	Mechanical index
UV	Ultraviolet
CWE	Compressional wave elastography
SWE	Shear wave elastography
SE	Static elastography
CW	Broadband
SS	Swept source

ACKNOWLEDGMENTS

I would like to thank my adviser, Professor Zhongping Chen, for his unconditional support throughout my Ph.D. studies. He taught me what it means to be a researcher and a mentor. He has been a role model for me both in the laboratory and in the outside world. I could not have accomplished any of this without his guidance, and am extremely grateful for his patience and understanding.

I would like to thank my committee members, Professor William Tang and Professor Matthew Brenner, for their valuable input and dedication to my studies. I really appreciate your taking the time out of your busy schedule for me.

I would like to thank our collaborators from USC, particularly Professor Qifa Zhou, for the fruitful collaborations that resulted in this dissertation.

I am grateful for all my friends and colleagues that helped make this project possible. I want to thank Dr. Joe Jing, Dr. Jiawen Li, and Dr. Jiang Zhu for teaching me the ropes when I first joined the lab. I want to thank my fellow labmates that helped me get through each day and make failed experiments seem not too bad. I am grateful to have gotten to know many wonderful people and to work alongside them.

I would like to thank my mother and father in law for their undying support and always being the first to step up and offer their generous help. Thank you for teaching me life lessons that will stay with me forever. I truly enjoy your company and hope you both can come join us in Portland. Thank you to my sister in law for accompanying us through this journey and always having a positive attitude.

I would like to express my deepest gratitude to my parents and grandparents for their love and never ending support. My father has always selflessly provided me with the resources and opportunities to reach for my dreams. My mother often offers her cheerful attitude and kind words to get me through difficult times. My grandparents have been rooting for me since the beginning of elementary school, and their encouragements have been crucial during my 24 years of school. I am deeply grateful.

Finally, I need to thank my wife, Rachel, who is also my favorite lab mate and my best friend for life. I am so grateful to have found you, ironically, through our Ph.D. studies. Thank you for your loving support during times of struggles, and for proofreading everything that I write (I know that is painful sometimes). Thank you for your patience not only during my Ph.D. studies, but also during my job hunting process. Last but not least, thank you for giving us our wonderful daughter, Kimi, who is the most adorable toddler ever. You two are my world.

CURRICULUM VITAE

Youmin He

2011 B.S. in Electronics and Information Engineering, Beijing Jiaotong University

2014 M.S. in Electronics and Information Engineering, Beijing Jiaotong University

2017 M.S. in Biomedical Engineering, University of California, Irvine

2019 Ph.D. in Biomedical Engineering, University of California, Irvine

FIELD OF STUDY

Biophotonics and Biomedical Imaging

PUBLICATIONS

1) **Youmin He**, Yueqiao Qu, Joseph C. Jing, and Zhongping Chen. "Characterization of oviduct ciliary beat frequency using real time phase resolved Doppler spectrally encoded interferometric microscopy." *Biomedical optics express* ***(In press)***.

2) Yueqiao Qu, **Youmin He**, Yi Zhang, Teng Ma, Jiang Zhu, Yusi Miao, Cuixia Dai, Qifa Zhou, Mark Humayun, Qifa Zhou, Zhongping Chen. "Quantified elasticity mapping of retinal layers using acoustic radiation force optical coherence elastography." *Biomedical optics express* 9 (9), 4054-406. ***(Co-first)***

3) **Youmin He**, Yueqiao Qu, Jiang Zhu, Yi Zhang, Arya Saidi, Teng Ma, Qifa Zhou, and Zhongping Chen. "Confocal Shear Wave Acoustic Radiation Force Optical Coherence Elastography for Imaging and Quantification of the In Vivo Posterior Eye." *IEEE Journal of Selected Topics in Quantum Electronics* 25, no. 1 (2018): 1-7. ***(First author)***

4) Yueqiao Qu, **Youmin He**, Arya Saidi, Yihang Xin, Yongxiao Zhou, Jiang Zhu, Teng Ma, Ronald H. Silverman, Donald S. Minckler, Qifa Zhou, Zhongping Chen. "In-vivo elasticity mapping of posterior ocular layers using acoustic radiation force optical coherence elastography." *Investigative ophthalmology & visual science* 59, 455-461 (2018). ***(Co-first)***

5) Yan Li , Zhikai Zhu , Joseph C. Jing , Jason J. Chen , Andrew Emon Heidari , **Youmin He** , Jiang Zhu , Teng Ma, Mingyue Yu, Qifa Zhou, and Zhongping Chen. "High-Speed Integrated Endoscopic Photoacoustic and Ultrasound Imaging System." *IEEE Journal of Selected Topics in Quantum Electronics* 25, no. 1 (2018): 1-5.

6) Jiang Zhu, Junxiao Yu, Yueqiao Qu, **Youmin He**, Yan Li, Qiang Yang, Tiancheng Huo, Xingdao He, and Zhongping Chen. "Coaxial excitation longitudinal shear wave measurement for quantitative elasticity assessment using phase-resolved optical coherence elastography." *Optics Letters* 43, 2388-2391 (2018).

7) Yueqiao Qu, Teng Ma, **Youmin He**, Mingyue Yu, Cuixia Dai, Jiang Zhu, K. Kirk Shung, Qifa Zhou, Zhongping Chen. "Miniature probe for mechanical properties of vascular lesions using acoustic radiation force optical coherence elastography." *Scientific Reports,* 7, 4731 (2017). ***(Co-first)***

8) Wesley J. Moy, Erica Su, Jason J. Chen, Connie Oh, Joe C. Jing, Yueqiao Qu, **Youmin He**, Zhongping Chen, Brian JF Wong. "Association of Electrochemical Therapy With Optical, Mechanical, and Acoustic Impedance Properties of Porcine Skin." *JAMA facial plastic surgery* 19, 502-509 (2017).

9) Jiang Zhu, Yusi Miao, Li Qi, Yueqiao Qu, **Youmin He**, Qiang Yang, and Zhongping Chen. "Longitudinal shear wave imaging for elasticity mapping using optical coherence elastography." *Applied Physics Letters* 110, 201101 (2017).

10) Yueqiao Qu, Teng Ma, **Youmin He**, Jiang Zhu, Cuixia Dai, Mingyue Yu, Shenghai Huang, Fan Lu, K. Kirk Shung, Qifa Zhou, and Zhongping Chen. "Acoustic Radiation Force Optical Coherence Elastography of Corneal Tissue." *Selected Topics in Quantum Electronics, IEEE Journal of* 22, 1-7 (2016).

11) Jiang Zhu, Li Qi, Yusi Miao, Teng Ma, Cuixia Dai, Yueqiao Qu, **Youmin He**, Yiwei Gao, Qifa Zhou, and Zhongping Chen. "3D mapping of elastic modulus using shear wave optical micro-elastography." *Scientific Reports* 6, (2016).

12) Jiawen Li, Teng Ma, Dilbahar Mohar, Earl Steward, Mingyue Yu, Zhonglie Piao, **Youmin He**, K. Kirk Shung, Qifa Zhou, Pranav M. Patel & Zhongping Chen. "Ultrafast optical-ultrasonic system and miniaturized catheter for imaging and characterizing atherosclerotic plaques in vivo." *Scientific reports* 5 (2015): 18406

ABSTRACT OF THE DISSERTATION

Development of optical Doppler interferometry for the visualization of ocular elasticity and ciliary activity

By

Youmin He

Doctor of Philosophy in Biomedical Engineering

University of California, Irvine, 2019

Professor Zhongping Chen, Chair

Functional optical imaging techniques have become increasingly important due to their high resolution and non-invasive nature, and have been used to address many unmet needs in the biomedical imaging field. In the area of ophthalmology, mechanical properties have been shown to be an early indicator of retinal disease, but current imaging modalities are unable to provide high resolution in-vivo imaging to capture the minute changes in the elasticity of thin tissue layers at the back of the eye. For respiratory diseases, the ciliary cell function inside the airway have been discovered to play an important role in respiratory health and the onset of disease. Similarly, current techniques are not equipped to image and characterize the cellular level changes in in-vivo tissues. Phase-resolved Doppler (PRD) imaging is a technology developed by our F-OCT lab, primarily for visualizing blood flow and angiography. Recently, it has been determined that the PRD technique is able to provide high phase sensitivity, which can be used to obtain the tissue displacement as well as particle motions. Using this principle, we developed two types of imaging systems: confocal acoustic radiation force optical coherence elastography (ARF-OCE) and spectrally-encoded interferometric microscopy (SEIM). Using the confocal

ARF-OCE system, we present the first spatially mapped elasticity imaging in a live animal retina, and obtained a better understanding of the elasticity of different retinal layers. With the SEIM system, we introduced a novel method of spatially tracking ciliary activity in real-time of in vitro tracheal and oviduct tissues. We demonstrate that the SEIM system can image and quantify ciliary beating frequency and ciliary beating pattern with high speed and large field of view. While both these technologies use the PRD technique, the optical system has been optimized for the respective applications. The results in this dissertation serve as a stepping stone to the optimization and ultimately, the clinical translation of the PRD technique to diagnostic imaging. The developed technology has great potential for clinical diagnosis and management of a number of ocular disease, such as age related macular degeneration, glaucoma, presbyopia and myopia, as well as airway diseases such as asthma.

CHAPTER 1

Introduction

1.1 Retinal diseases

Age-related macular degeneration (AMD) is a progressive disease of the retina, and is the leading cause of severe vision loss in the western population over 50 years of age (1). AMD most often refers to drusen formation in the dry form, and neovascularization in wet AMD. Drusen is present in more than half of the population over 70 years of age, and often acts as an early sign of AMD (2). Neovascularization occurs when excess blood vessels leak into the layers of the retina, signifying a later stage of disease. Although age is the primary factor that contributes to AMD, there are a number of environmental and genetic factors that are also associated and contributes to the onset and progression of AMD, including smoking, obesity, sunlight exposure, etc (3). The retina consists of many different layers that work to sense the light signal and transmit the relevant information to the brain via the optic nerve, which is demonstrated in figure 1.1.

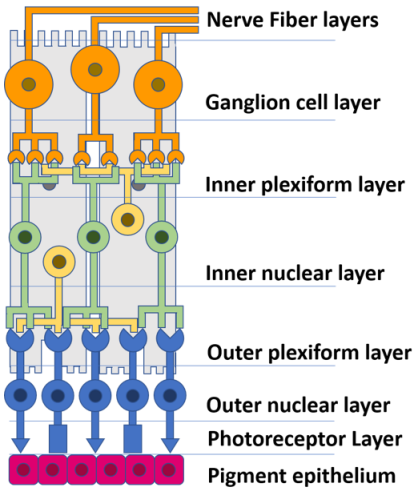

Figure 1.1 Schematic of the Retina Layers

When there is damage to the retina, most often damage to the rod and cones, and the optic nerve, vision impairment occurs, sometimes even leading to blindness. Current methods of diagnosis include fundus photography, which provides surface structural information of the retina, and fluorescein angiography, which is used to visualize blood vessels if neovascularization is suspected (4). For more accurate visualization of the entire depth of the retinal layers, optical coherence tomography (OCT) is used for non-invasive optical imaging (5). OCT angiography is also used to detect the blood vessel formations and diagnose any abnormal regions. Once AMD is diagnosed, there is currently no known cure, so disease management is necessary in various forms, including antiangiogenic drugs, radiation and laser treatments, and photodynamic therapy (6). Since it is important to slow down the progression of the disease through treatment, early diagnosis is essential. With current methods, it is possible to see anatomical changes that occur with drusen formation and neovascularization. However, it is often difficult to diagnose in the early stages, before structural changes are evident.

Recent studies show that the mechanical properties of the posterior eye also change with the onset of disease, such as in the case of angiogenesis or retinal degeneration (7, 8). In particular, the mechanical stress on the retina gets altered during the early stages when drusen deposits begin to form, and also later when blood vessels infiltrate. Since it is often difficult to visualize drusen when the deposits are on the micron level, it would be helpful to use an alternate means of diagnosis (9). In addition, since the layers of the posterior eye are made of a tight network of cells and tissues, the elasticity of different layers is expected to differ (8, 10). These changes could also be critical in detecting retinal diseases.

As the second leading cause of blindness worldwide, glaucoma affects over 2.2 million people in the United States (11, 12). Due to the aging population, the estimated number of people suffering from glaucoma is expected to reach over 80 million worldwide, with 11 million ultimately becoming bilaterally blind (13). Research show that glaucomatous vision loss is due to damage to the retinal ganglion cell axons within the lamina cribrosa (LC) of the optic nerve head (OHN). Recent studies further support the explanation by revealing significant microarchitecture changes within the LC at the early onset of glaucoma (14). Since the vision loss is irreversible in most instances, early detection is crucial for disease management.

Intraocular pressure (IOP) related vision loss has been well documented in human retinal studies, providing fundamental information for the disease diagnosis and management. Specifically, elevated IOP, as the major risk factor, can induce mechanical insult on the retina and optic nerve head (ONH) and initiate retinal ganglion cell apoptosis that often leads to glaucoma. This idea inspired the development of traditional early diagnosis methods that focus on the monitoring and prediction of the IOP level. However, it has been shown that an elevated IOP might induce glaucoma on one eye but not affect the other in the case of ocular hypertension, which is counter-intuitive. In other cases such as normal tension glaucoma, the disease may even develop on eyes with normal IOP. The individualized sensitivity to IOP has greatly complicated the understanding of the pathophysiology and attracted extensive interests in the research of glaucoma.

Recent studies (14-20) have suggested that tissue biomechanics may determine the ONH resistance to IOP. Moreover, several ex-vivo animal studies have revealed that the mechanical properties of the ONH tissue are variable across different stages of glaucoma (21, 22), and across

other risk factors such as age (13, 23, 24) and race (25). Decades of discoveries indicate that the biomechanical characteristics of ONH tissues may determine their robustness against the IOP-induced force and deformation, and particularly, the glaucomatous related deformation on the lamina cribrosa (LC) as well as the peripapillary sclera (ppSC) surrounding it. (15, 16, 18, 26-28) While ex-vivo studies allow for immediate access to the optic nerve head tissues, the tissue extraction and manipulation procedures both compromise the measurement accuracy. It is also clinically infeasible to investigate ocular tissue using ex-vivo methods.

1.2 Elasticity imaging

Thanks to the notable advances in the field of medical imaging, elastography is becoming a useful technique to map out the mechanical properties of soft tissues in-vivo. In general, elastography measures tissue mechanical properties by (i) inducing tissue displacement with an external or internal excitation, (ii) detecting tissue response with a specific imaging modality, and (iii) quantifying tissue elasticity based on the elastic theory and tissue displacement in response to the excitation (29-32) .

A variety of techniques can be utilized for these three steps in elastography and has been shown by table 1.1 below. Although the basic notion has not changed over the past two decades, the elastography techniques have integrated a variety of excitation, detection, and quantification methods to accommodate different applications.

Excitation		Detection	Parameter estimation
External	Internal	Magnetic Resonance Ultrasound Optical	Qualitative Quantitative
Dynamic	Static		

Table 1.1 Elastography in three steps.

Internal excitations, generated by pressure inside the organ or voluntary motion of live beings, are not suitable for quantitative assessment of ocular elasticity since the elastic responses of these internal stimulations are difficult to predict. Numerous techniques for external excitation, including piezoelectric elements (33), air puff devices (34, 35), ultrasonic acoustic radiation force (ARF) (34, 36-44), or even freehand compression (45, 46), have been applied to deform the tissue. While these methods can readily generate controllable forces onto the sample surface, ARF is the only one that is able to penetrate and deform to subsurface tissues directly. Furthermore, the beam width of ARF can be focused within 1 mm (42), which allows for precise perturbation on small regions of interest (ROI). Given that the eye is composed of many small biological units, ARF is the most suitable technique to generate focused displacements on the ROI so as to minimize the influences of surrounding components.

Depending on the mechanism of the excitation force, elastography can be classified as static or dynamic (29, 31, 32). In the case of static elastography (SE), a stepped compression force is applied on the sample, and the strain of the sample will be mapped out as the manifestation of stiffness. The interpretation of the outcome is very straight forward in that a low strain indicates

stiff components and vice versa. It can also be readily integrated into existing imaging modalities since simple methods, such as freehand compression, can be used to induce the excitation force. However, current clinical SE systems cannot generate quantitative results due to the lack of stress measurements of the force (47). In contrast to SE elastography, dynamic elastography (DE) applies a time-varying force on the tissue to generate mechanical waves, which consist of parameters that are indicative of tissue elasticity. The force, which can be a modulated waveform at fixed frequency, a transient pulse, or multiple pulses focused at successive locations, can generate both compressional and shear waves within the sample. Since the speed of shear wave is directly related to the shear modulus, tissue density, and the Poisson ratio, it is possible to yield the quantitative elasticity by making several assumptions (36, 43, 44, 48-52). Compressional wave induces axial vibrations, but its speed is much faster than that of shear wave, and thereby exceeds the imaging speed of current imaging modalities. However, recent studies analyze the amplitude and resonance frequency of the axial vibration, from which quantitative elastograms can be generated (39-41). In general, SE offers easy and fast qualitative screening, while DE allows for quantitative measurements but requires extensive computation.

Regardless of the excitation mechanism, displacement detection methods are able to independently determine the imaging range, spatial resolution, and sensitivity. Common detection modalities include ultrasound, magnetic resonance imaging (MRI), and optical coherence tomography (OCT). In comparison, MRI has the widest imaging range, OCT the highest resolution, and ultrasound in the middle (53, 54). In measuring the biomechanics for glaucoma, pilot studies use ultrasound imaging to detect the elasticity of the ONH and ppSC in-vivo (45, 46, 55, 56). Both static and shear wave based elastography (SWE) were successfully

utilized to evaluate the elasticity of ocular tissue and differentiate glaucomatous eyes from healthy ones using several metrics. Although most of these studies agree that the mean elasticity of the ONH is stiffer for glaucomatous eyes than healthy ones, they are not able to identify the elastic alterations of the LC within the ONH complex. Additionally, several studies concluded that SE may be limited due to the interference of the fluid components in the vitreous with the transduction of the compressional force to the ONH; SWE using ARF is free of this limitation (55, 57).

As the gold standard for clinical ophthalmic imaging, optical coherence tomography (OCT) has the capability to visualize ocular tissue with micron-scale resolution, which far surpasses the resolution of ultrasound imaging (53, 54). Optical coherence elastography (OCE) is becoming the frontier in characterizing mechanical properties, where Doppler OCT (DOCT) is used to detect tissue displacement. Phase resolved Doppler OCT (PRD-OCT), a functional extension of OCT (58-61), takes advantage of pico-meter displacement sensitivity and allows for the detection of tissue displacements under a minute excitation force (36, 40). Therefore, functional OCT is intrinsically suitable for the in-vivo elasticity assessment of ocular tissues including the ONH and LC. Extensive studies have been performed to map out and analyze the elasticity of the anterior segment of the eye globe with various excitation mechanisms, including air puff devices and cylindrical ultrasound transducers (34, 35, 62, 63). However, the posterior eye is difficult to access using these configurations, and in-vivo ONH elasticity imaging has not been possible to date. Specifically, air puff cannot penetrate through the anterior eye, while a co-alignment of the optical beam and the ARF beam generated by a solid cylindrical ultrasound transducer is extremely challenging. Fortunately, recent studies (36, 40), reporting on a collaborative effort

between UCI and USC, have opened up the possibility of measuring the mechanical properties of the retina in-vivo using confocal ARF-OCE techniques.

1.3 Ciliary diseases

The human airway serves not only as a passage for oxygen intake, but also as the first line of defense to protect the lungs from harmful foreign particulate. The main defense mechanism is the mechanical clearance of mucus through ciliary activity and regulation of airway surfaces (64). Specifically, ciliary beat frequency and amplitude are considered the main factors that determine the maximal transportation speed of the mucus from the lower airway to the pharynx, and hence affect the mucociliary clearance rate (MCR) (65). In addition, it was reported that the ciliary beating synchronicity would also contribute to the MCR. Dysfunction of cilia, caused by ciliary defects such as primary ciliary dyskinesia (PCD), virus, toxins, or trauma will usually result in ineffective mucociliary clearance and lead to lung damage (66). Although the damage caused by ciliary defects such as PCD cannot be fully treated, previous studies indicate that it is possible to maintain sufficient lung function through appropriate respiratory care (67). Therefore, it is important to monitor the spatial ciliary beat frequency (CBF) and the ciliary beat pattern (CBP) in human airways for disease diagnosis and management.

The traditional procedure to analyze airway ciliary activity involves three steps: sample preparation, recording, and CBF measurement. A biopsy using a cytology brush is usually performed to harvest the ciliated cells from human respiratory tracts for cell culture (68, 69). Many techniques, based on the photoelectric method (70) and video cameras, were reported to be capable of evaluating ciliary activity. Due to the microscopic nature of ciliary structure and

movement, a high resolution and high sensitivity imaging modality is essential to visualize the CBP and beat frequency. Optical microscopy is useful in resolving single cilia movements but sufficient imaging speed is also required to obtain quantitative results of CBF and record the entire beating cycle. This leads to the utilization of high speed digital camera microscopy system (68, 71). However, conventional digital camera system cannot investigate ciliary functions *in-vivo*, and thereby diminishes the effectiveness of the measurement in physiological settings.

Tubal transport is an essential process for successful spontaneous pregnancy by controlling the interaction between gametes as well as delivering the fertilized ovum to the uterus for implantation (72-74). Dysfunctions in tubal transport, such as failure to capture the oocytes or transport the ovum, can induce infertility or life-threatening ectopic pregnancy (75-77). Within the oviduct, the two major effectors for tubal transport include the smooth muscle contractions and the coordinated ciliary beats (78, 79). Pilot studies further indicated that ciliary activity plays a dominant role in the transportation of the fertilized ovum (80, 81). Particularly, the synchronized beating of the cilia generates the driving force to move the fluid as well as the ovum through the oviduct (77). Therefore, it is of great significance to study the frequency and synchronicity of oviduct ciliary activity to better understand the etiology of fallopian tube related ectopic pregnancy or infertility.

Over the past several years, bright field microscopy has been the core technique to visualize the ciliary activity and measure the CBF using the light fluctuations induced by ciliary beats (82-91). However, bright field microscopy is currently incapable to investigate the ciliary activity of *in-vivo* tissues due to the tradeoff between the size and resolution of its endoscope. The resolution

of white light endoscopy relies on the number of fiber bundles or the pixel size of digital cameras, and it is thereby difficult to achieve micron scale resolution with a sub-millimeter probe diameter (92). Recently, optical coherence tomography (OCT) has been utilized to assess the *in-vivo* mouse oviduct (93-95). The depth resolved imaging capabilities of OCT allows for access to the inner cavity of the fallopian tube through the open abdominal cavity, and the CBF is measured by analyzing the intensity fluctuations at ciliated sites (93, 94). Although endoscopic OCT has the potential for *in-vivo* oviduct CBF imaging, it is still insufficient to visualize the complex patterns and synchronicity of ciliary behavior due to the limited resolution in resolving the ciliary strokes on the micron level (96, 97).

1.4 Ciliary activity imaging

The vast majority of studies involving ciliary activity uses a combination of high-speed digital camera and bright field microscopy. However, bright field microscopy is not feasible for in-vivo applications because of the tradeoff between its spatial resolution and the size of the endoscope. If a miniature camera is mounted on the distal end of the probe, the pixel size of the camera will be the bottleneck for insufficient resolution. In other cases where the camera is mounted on the proximal end, it would be difficult for endoscopes with small diameters (~1 mm) to encompass a large enough field of view to visualize sufficient amounts of fiber bundles and achieve micron level resolution at the same time. Although ex-vivo studies could reveal the ciliary response under various factors, it is usually not feasible in studying gradual changes in ciliary activity during the progression of respiratory or reproductive disease. Additionally, ex-vivo tissue biopsies are uncomfortable for patients and often cause extended damage to the fragile ciliated tissue. Therefore, it is essential to have an *in-vivo* imaging modality to non-invasively probe the

ciliary changes to better understand its role in different pathology and provide a possible tool for the early diagnosis of relevant diseases.

In order to overcome these limitations and perform in-vivo studies, optical coherence tomography (OCT) (98) was recently applied on ciliary motion imaging, taking advantage of its micron scale resolution, real time imaging capability, and potential for endoscopic imaging. Given these powerful features, the study of ciliary functions moves from the dish plate to its natural environment, and demonstrates the feasibility of using OCT to investigate ciliary activity in-vivo (93, 99). Specifically, a high resolution OCT endoscope is inserted into either the respiratory or uterus cavity to perform continuous acquisition at one cross sectional site, so that the intensity fluctuations caused by ciliary activity can be visualized over time. Although CBF can be estimated from the variations in OCT intensity, the synchronicity between different cilia cannot be easily investigated to study CBP.

To further expand the effectiveness of using an OCT system in imaging ciliary activity, our group used a phase resolved Doppler optical coherence tomography (PRD-OCT) technique to probe the beating direction and speed of cilia. PRD-OCT is well known for its capability of measuring microscopic particle movement with pico-meter sensitivity (36, 40-42, 100), and is proven to be a powerful tool in visualizing accurate ciliary dynamics by providing not only its transient position but also the relative speed and direction of the ciliary beat (96). Therefore, the beating phase of different cilia can be simultaneously monitored to study their synchronicity and beating patterns. In addition, the velocity imaging capability of PRD-OCT also benefits ciliary studies by enhancing the contrast of moving cilia versus other stationery tissue components, and may

possibly aid in locating the ciliated area within the entire cavity during in-vivo experiments. However, to visualize spatial-temporal cilia activity using OCT requires a two dimensional beam scan (101). Because the rate of the spatial scan must be at least two times greater than the CBF for effective measurements according to the Nyquist theory, there is a limitation on the number of scanning points, which limits the lateral FOV.

A spectrally encoded interferometer (SEI) is capable of lateral 2-D imaging with a single axis beam scan (102, 103), which allows for en face imaging at a speed comparable with OCT B-Scans. We report on a swept source spectrally encoded interferometric microscopy (SS-SEIM) system to obtain the enface image of cilia beating frequency and pattern at high speed. With a swept souce laser of 100kHz, we are able to achieve 100 frames per second (fps) over an enface image area up to 1 mm^2. To achieve similar en-face imaging speed, traditional D-OCT image would require swept source laser with a swept rate over 100 MHz, which is not currently available. This is the first study to map the spatial-temporal ciliary activity using a SS-SEIM system to the best of our knowledge, and opens up the possibility of investigating spatial ciliary beating frequency and pattern in-vivo.

1.5 Summary of chapters

In this dissertation, we explore functional optical imaging methods to diagnose and detect diseases at their early stages, with the aim to provide a novel clinical means to evaluating the condition. We primarily target respiratory and ophthalmic disorders that have an unmet need on the market today. By utilizing our foundations on Doppler OCT, we evolved the technique to perform phase-resolved Doppler imaging, which is able to probe for various functional

parameters such as the elasticity and cellular motions. We present the development of two such optical systems and their optimization processes for targeting the diseases of interest.

Chapter 2 introduces the principles behind the proposed imaging systems. First, we discuss the fundamentals of Fourier-domain OCT, including both SD-OCT and SS-OCT. Then we delve into the principles of phase-resolved Doppler imaging, and how those concepts can be utilized to do elasticity imaging and cellular activity imaging. Finally the basic ideas behind ARF-OCE and SEI are discussed, as well as current disadvantages in both respective systems. We conclude with the proposed optimization and improvement ideas for a novel system and where they may prove to be useful in the medical industry today.

Chapter 3 presents the confocal shear wave ARF-OCE system development and optimization methods for posterior eye imaging and disease diagnosis. The novel processing and segmentation algorithm is discussed in detail. Both ex vivo and in vivo rabbit ocular samples were studied and the elasticity of the layered retinal structure is quantified and spatially mapped.

Chapter 4 discusses the motivations for converting from an SD-OCT to an SS-OCT system for functional imaging, with advantages primarily being the imaging speed and higher SNR. Then we present a novel method of quantifying the phase stability of different lasers in order to select the most optimal source for our phase-resolved Doppler applications. Lasers from different makers were tested and the results were promising, leading us to building the phase-resolved Doppler SEI system with an SS laser.

Chapter 5 focuses on the development of the SEIM system, which is able to provide high speed, high resolution en face imaging with motion detection and large FOV. This system aims to study the ciliary activity in the respiratory and reproductive systems in real time, and provide a means of detecting changes in ciliary function during disease onset and progression. We present the novel processing algorithm as well as the experimental results for tracheal and oviduct tissues under different external conditions, such as temperature changes and drug administration. The spatial ciliary activity maps that resulted from this system can offer insight into the ciliary function and diseases.

Chapter 6 summarizes the work that has been presented in this dissertation from the general motivation, to system and algorithm development, to experimental results that can serve as preliminary data for translation into clinical studies. Last, future research directions include an endoscopic imaging design for in vivo imaging, an ocular OCE project to evaluate the optical nerve head elasticity, and a single-shot shear wave OCE system to provide fast imaging with minimum patient exposure.

CHAPTER 2

Principles of Phase-resolved Doppler Imaging

In this chapter, we introduce the basic concepts of the optical coherence tomography and its functional imaging methods. First we cover the principles of optical coherence tomography in section 2.1. In section 2.2, the methods of phase-resolved Doppler imaging are discussed. Next, the principles of acoustic radiation force optical coherence elastography using an extension of the phase-resolved Doppler method is presented in section 2.3. Then section 2.4 covers the principles of spectrally-encoded optical coherence microscopy, which also utilizes the Doppler principles. Last, the chapter ends with a summary in section 2.5.

2.1 Principles of optical coherence tomography

OCT is a developing optical imaging technique in the biomedical industry and can noninvasively resolve cross-sectional tissue structures at the micron resolution (104, 105). It uses near infrared light, which is non ionizing and extremely safe for use on human tissues (106, 107). It also has the capability to be incorporated into a sub-millimeter endoscope and can perform high speed real-time imaging for in-vivo applications (105, 106, 108, 109). Moreover, OCT takes advantage of optics, and while it is often described as "ultrasound with light," it does not need a transduction medium like ultrasound (108-110). Due to these unique features, OCT has been utilized in recent years to solve for unmet needs in the field of biomedical imaging (108, 110-113).

Traditional optical imaging technique uses the intensity of back scattered light to visualize the tissue structure only at the focal plane, because they does not have sufficient acquisition speed to

temporally resolve the light beams reflected from different imaging depths (105, 114). Other non-optical imaging techniques such as ultrasound can resolve the echo or transmission signals from different depth locations but cannot provide the equivalent level of resolution due to the utilization of longer wavelengths(115, 116). OCT utilizes an interferometric setup to differentiate the back-scattering light beams from different axial positions in the tissue, and thereby simultaneously achieves micron resolution and depth resolved imaging capabilities (98, 105).

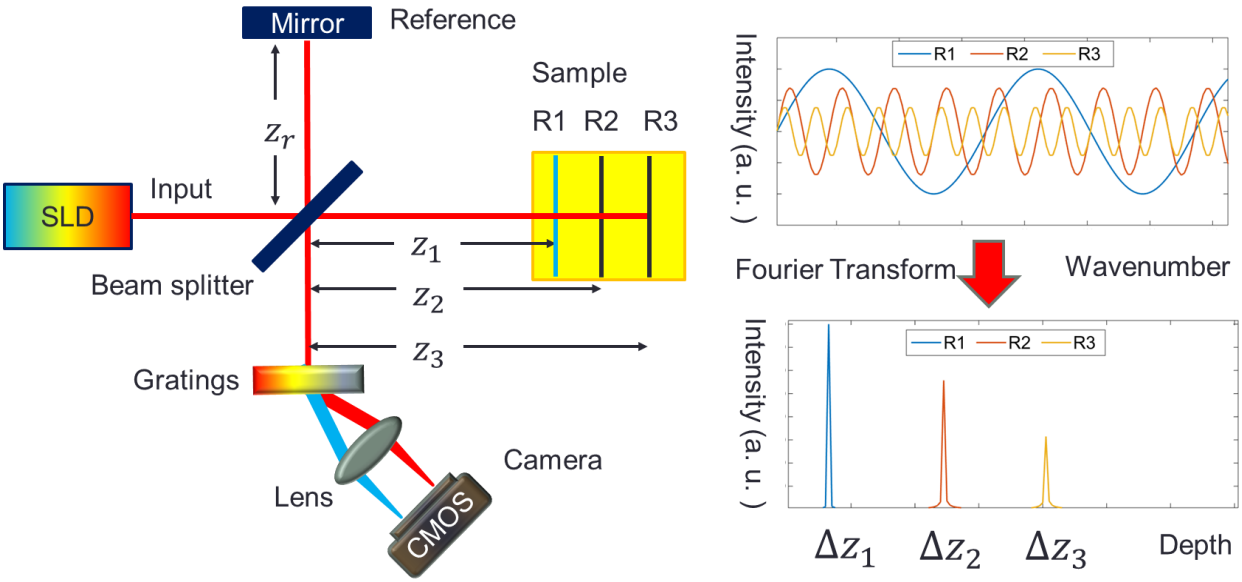

Figure 2.1 Schematic of the principle of OCT. a) schematic of a typical OCT system. b) interference signal from different scattering particles. c) depth profile of sample structure. SLD: superluminescent diode.

Figure 2.1a demonstrates a schematic diagram of a typical OCT system (104, 105), where a broad band laser, or low coherence laser, is used as the light source. A beam splitter splits and delivers the illumination energy to a mirror in the reference arm and the tissue or phantom in the sample arm, respectively. The reflections from the sample and the reference mirror then return to

the beam splitter and generate interference that can be converted to electrical signal by the photodetector. Finally, the electrical interference signal will be digitized and registered in a digital device for data analysis. According to the theory of interference, the optical path length difference between the sample and reference reflectors will form constructive and destructive interference along different wavenumbers, *k,* and modulates the laser spectrum with a cosine wave as shown in figure 2.1b (98, 104, 105, 114). The derivation of the cosine wave interference pattern will be discussed in detail. In general, a Fourier transform can be applied on the cosine modulations to obtain the axial location and reflectivity at different axial positions in the sample and thereby reconstruct the depth profile plotted in figure 2.1c.

$$E_r(k,w) = \sqrt{c}S(k,w)\sqrt{r_r}e^{j(2kz_r - wt)} \quad \text{(Eq. 2.1)}$$

$$E_s(k,w) = \sqrt{(1-c)}S(k,w)\sum_{n=1}^{N}\sqrt{r_s(z_n)}e^{j(2kz_n - wt)} \quad \text{(Eq. 2.2)}$$

The light reflected from the scattering particles in the sample and the reference mirror can be described in the form of an electric field as shown by equations 2.1 and 2.2, respectively. E_r and E_s denotes the back scattered light from the reference and sample respectively, c denotes the ratio of light that is transferred from the laser to the reference, z_n and z_r represent the optical path length that the light has propagated in the sample and reference arms respectively, and n denotes the resolvable reflectors within the sample. Variables k and w are wavenumber and angular frequency of the light, respectively. Based on the superposition principle of the electric field, the power of an interference signal can be obtained and represented by equation 2.3. In the equation, $r_s(z_n)$ and r_r represent the reflectivity of the sample at depth z_n and the reference mirror respectively. The interference signal will then be fed to the photodetector, which converts its intensity to the electrical signal as shown by equation 2.3.

$$\mathrm{I(k,w)} = \rho\langle|\mathrm{E_s} + \mathrm{E_r}|^2\rangle$$

$$=\rho\langle(E_s + E_r)(E_s + E_r)^*\rangle \quad \text{(Eq. 2.3)}$$

Where ρ is the responsivity of the detector, $I(\mathrm{k}, \mathrm{w})$ denotes the intensity of the output electrical current from the photodetector for wavenumber k and angular frequency w, and $\langle \quad \rangle$ represents the average of the interferogram over response time of the photodetector. Equation 2.3 can be further elaborated as equation 2.4 by incorporating equation 2.1 and 2.2 to 2.3.

$$\mathrm{I}(\mathrm{k}, \mathrm{w}) = \rho\left\langle\left|\sqrt{c}S(k,w)\sqrt{r_r}e^{j(2kz_r - wt)} + \sqrt{(1-c)}S(k,w)\sum_{n=1}^{N}\sqrt{r_s(z_n)}e^{j(2kz_n - wt)}\right|^2\right\rangle \text{(Eq. 2.4)}$$

Since the light waves are oscillating at a much higher frequency than the cutoff frequency of the photodetector, the oscillations and the angular frequency, w, are converted to constant electrical current and eliminated from the interference signal as shown in equation 2.5.

$$I(k) = \rho[cS(k)r_r + (1-c)S(k)\sum_{n=1}^{N} r_s(z_n) \quad \text{(a)}$$

$$+\sqrt{c(1-c)}S(k)\sum_{n=1}^{N}\sqrt{r_s(z_n)r_r}\,cos\,2k(z_n - z_r) \quad \text{(b)}$$

$$+(1-c)S(k)\sum_{m\neq n=1}^{N}\sqrt{r_s(z_n)r_s(z_m)}\,cos\,2k(z_n - z_m)] \quad \text{(c)}$$

(Eq. 2.5)

Three different components contribute to the power of the interference signal. The DC term in equation 2.5a represents the summation of the optical power from both arms, which does not contain any structural information and needs to be removed. The auto-correlation (AC) term in equation 2.5c refers to the self-interference that occurs in between sample reflections from different axial positions. The power of the AC term is often very small and it is difficult to extract the structural information from it directly. The cosine modulation is primarily given by the cross-correlation (CC) term in equation 2,5b, where at different depth z_n, the cosine wave will have a frequency proportional to its difference from the reference path length, z_r. Additionally, the power of the CC term is also correlated to the square root of the product of the sample and reference reflectivity, written as $\sqrt{r_s(z_n)r_r}$. Therefore, by eliminating the AC and DC

terms, and then performing the Fourier transform on the CC term only, the position and reflectivity of the axial reflectors in the sample can be obtained and thereby the depth profile can be reconstructed.

$$I(z) = \rho\mathcal{F}^{-1}(\sqrt{c(1-c)}S(k)\sum_{n=1}^{N}\sqrt{r_s(z_n)r_r}\,cos\,2k(z_n - z_r))$$

$$= \rho\sqrt{c(1-c)}S(z)\otimes\sum_{n=1}^{N}\sqrt{r_s(z_n)r_r}\left(\delta(z + 2z_n - 2z_r) + \delta(z - 2z_n + 2z_r)\right)$$

(Eq. 2.6)

Where S(z), the point spread function of the system, is the Fourier transform of the light source spectrum. The Fourier transform applied on the CC term will convert the signal from the wavenumber or k space to depth or z space as shown by equation 2.6. Specifically, each cosine modulation in k space corresponds to a δ function in the z space, where the magnitude of the reflectivity is calculated along the axial position. Since the CC term is the convolution of the point spread function $S(z)$ and the depth profile of the sample, the axial resolution of OCT will be defined by the profile and the bandwidth of the spectrum. If the profile of the laser spectrum S(k) is a Gaussian function, the axial resolution can be derived as shown in equation 2.7.

$$L = \frac{2ln2}{\pi}\frac{\lambda_0^2}{n\Delta\lambda} = 0.44\frac{\lambda_0^2}{n\Delta\lambda} \quad \text{(Eq. 2.7)}$$

Where λ_0 and $\Delta\lambda$ are the center wavelength and the bandwidth of the laser respectively, and n denotes the refractive index in the sample. Similar to traditional light microscopy, the lateral resolution (Δx) of an OCT system depends on the wavelength (λ) as well as the focal length and aperture diameter of the focusing lens, which is shown in equation 2.8 below.

$$\Delta x = \frac{4\lambda}{\pi}\frac{f}{d} \quad \text{(Eq. 2.8)}$$

Based on the sampling theory, a discrete sampling system can only resolve frequencies lower than half of its sampling frequency. Since OCT system discretely samples the spectrum, its

ability to resolve high frequency signals, or interference signals generated by deep scatters, will also be constrained by its sampling interval, or spectral resolution. The spectral resolution, expressed by the resolution of the wavenumber or wavelength, is determined by the number of pixels on the spectrometer and the instantaneous linewidth of the laser source for SD-OCT and SS-OCT respectively. Theoretically, the discrete spectral signal $I^*(k)$, shown by equation 2.9 ,can be defined as the convolution of the continuous interferogram $I(k)$ and a Gaussian function with a narrow full width half maximum (FWHM) equals to δk, the resolution of the wavenumber.

$$I^*(k) = I(k) \otimes e^{\frac{-4\ln(2)k^2}{(\delta k)^2}} \quad \text{(Eq. 2.9)}$$

After Fourier transform over wavenumber k, the convolution $\otimes$ will be converted to multiplication, and the narrow Gaussian function will be converted to relatively wide Gaussian function in depth domain as shown in equation 2.10.

$$I^*(z) = I(z) \cdot e^{-(4z^2)\frac{(\delta k)^2}{4\ln(2)}} \quad \text{(Eq. 2.10)}$$

Apparently the width of the z domain Gaussian function will determine the imaging depth of OCT in that the profile of the Gaussian function results in a sensitivity roll off over depth. More specifically, 6dB sensitivity roll off in the depth direction z_{6dB} can be defined as a function of either wavenumber resolution δk or wavelength resolution $\delta \lambda$ as shown by equation 2.11.

$$z_{6dB} = \frac{2\ln(2)}{\delta k} = \frac{\ln(2)}{\pi}\frac{{\lambda_0}^2}{\delta \lambda} \quad \text{(Eq. 2.11)}$$

Where $k = \frac{2\pi}{\lambda}$, and λ_0 denotes the center wavelength. It is also important to note that the sampling interval of the digital system should be smaller than the spectral resolution of the optical system to ensure the integrity of the digitized signal and maximized image depth as shown by equation 2.12.

$$N \geq \frac{\Delta\lambda}{\delta\lambda} \qquad \text{(Eq. 2.12)}$$

Where the digital system samples the entire spectrum into N points and the value of N should be no smaller than the bandwidth of the system $\Delta\lambda$ divided by its wavelength resolution $\delta\lambda$. While the spectral resolution determines the maximum imaging depth, the amounts of photons that are reflected from different depths rely on the depth of focus (DOF) and the scattering characteristics of the tissue. Generally, optical penetration can be enhanced by using a long DOF objective or a long wavelength light source. However, increasing the DOF or the wavelength could also compromise the spatial resolution, especially the lateral resolution which is solely dependent on these two parameters. The scattering characteristics of the tissue is also very important to the imaging depth in that a highly scattering sample can reflect a greater amount of photons than a relatively less scattering sample.

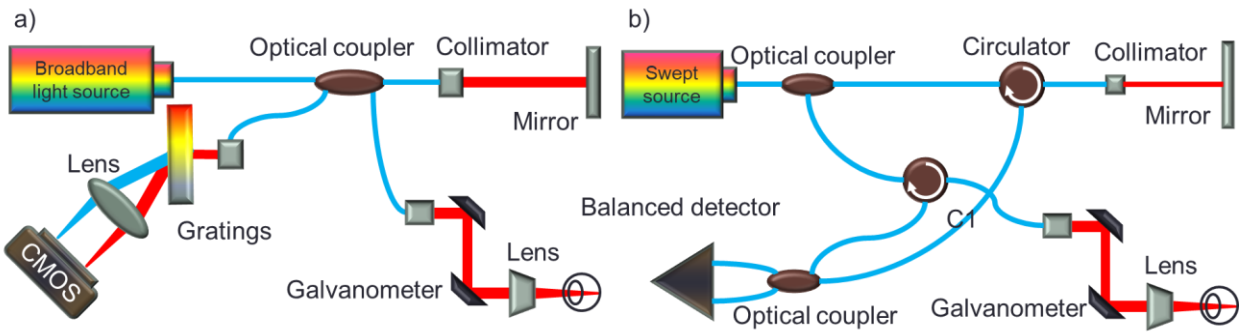

Figure 2.2 Schematic of the two primary OCT Systems. a) SD-OCT driven by broadband laser. b) SS-OCT driven by swept source laser. OC: optical coupler, CO: collimator, M: mirror, SL: scan lens, GM: Galvanometer mirror, G: diffraction gratings, L: lens, C: optical circulator, S: sample, PD: photodetector, SS: swept source laser

There are two major types of OCT systems using different laser sources and detection methods. The basic setup can be illustrated in Figure 2.2 (108, 117). The spectral domain (SD) OCT system, as shown in figure 2.2a, utilizes a broadband laser as the light source, an optical coupler to split and collect the energy, and a spectrometer to chromatically disperse the interference light and spatially register the spectrum using a line-scan camera. Figure 2.2b shows a general setup for SS-OCT, where a pulsed swept source laser is utilized to drive the system across a range of wavelengths, and a photodetector is used to acquire the interference patterns emitted by the laser discretely over time.

According to previous literature, SD-OCT is known for its capability in measuring the phase of the interference signal with high sensitivity, since the system continuously emits and registers all the wavelengths at once and so the phase of the light is very stable over time (118, 119). Since the pulsed laser in the SS-OCT system often emits and registers wavelengths across the full bandwidth in a discrete and repetitive manner, theoretically the phase of the light has inherent instability due to inconsistency between repetitions (120). However, the SD-OCT is usually not as fast as SS-OCT due to the speed limitation of camera (119). In fact, the SS-OCT typically has a faster acquisition speed and a relatively higher signal to noise ratio (SNR) than SD-OCT systems when reconstructing tissue structures (121). Recent studies further indicate that the longer exposure time required for a SD-OCT system could make it vulnerable to the fringe washout phenomenon that will degrade the SNR of the signal and reduce the overall imaging quality (122)..

Another major advantage of the SS-OCT is that most of the current swept source lasers provide an electrical clock to accurately time with the emission of each wavenumber and ensures that the interference fringe is digitized at equal wavenumber interval. For SD-OCT, since the spectrum is not linearly dispersed onto the camera sensors, the interference signal is registered at changing wavenumber intervals and requires resampling, or in another word, calibration. A typical SD-OCT calibration involves three steps: 1) registers an interference fringe with single frequency component. 2) generates a group of coefficients that indicates the location of wavenumbers at equal interval. 3) uses the coefficients to interpolate the raw interference signal at wavenumbers with equal interval. For step 1, a single frequency interference signal will have a phase term changing linearly with the wavenumber, and we can thereby extract the phase and use it to resample the signal at same phase interval and by association same wavenumber interval. Traditional calibration method uses a mirror to generate a single frequency fringe but could be unreliable because the transduction medium mismatch between the reference and the sample arm can broaden the frequency bandwidth of the interference signal and compromise the precondition of calibration. To solve for this issue, our group has used a cover slip to generate self-interference signal and ensures the phase of the signal is changing in a constant rate (123). For step 2, OCT typically uses Hilbert transform to extract the phase, and then locates the lateral coordinates that can linearly resample the entire signal at equal phase interval. Lastly, the coordinates will be saved as the coefficients and used in step 3 to calibrate the interference signal immediately acquired from the digitizer. Failure to perform the calibration will result in a compromise in resolution because a distorted cosine wave modulation will have a dispersed shape in its frequency domain. Additionally, since the alignment of the spectrometer can change over time, it is necessary to recalibrate the system periodically. In short, SD-OCT is believed to

be superior for applications that require high phase stability, while SS-OCT is a more suitable candidate for fast structurally imaging with high SNR and allows for a simple processing scheme that does not require calibration.

To summarize the discussion in this section, OCT is a non-invasive, non-ionizing, and high-speed imaging modality that can resolve the depth profile of thin biological tissues with micron scale resolution. The imaging parameters of OCT primarily depends on the laser source, objective lens, as well as the digitizer, but it is also critical that all the other components have sufficient specifications to ensure compatibility of the entire system. Since different parameters rely on and affect each other, it is always important to consider the tradeoff between them and make the best selection after carefully analyzing the requirements of the targeting application. Overall, OCT provides promising potential for the *in-vivo* studies of millimeter thick tissue structures and can be a powerful tool for disease tracking and diagnosis in clinics.

2.2 Principles of phase-resolved Doppler method

The phase resolve Doppler (PRD) method is a functional extension of OCT that is able to detect the changes in the interference signal in response to the movements of scattering particles in the sample (59, 106, 107, 124, 125). PRD-OCT is able to visualize the axial motions of all the particles that can be resolved in the OCT structural image without additional hardware or image acquisition (59, 125). The measurement accuracy of PRD mainly relies on the inherent stabilities of the system, where slight internal variations could introduce errors to the phase measurement (120). This method is extremely sensitive to motion as represented by large shifts in the interferogram (51, 113, 117, 126). More specifically, the phase stability of the laser and the

signal to noise ratio (SNR) determines the accuracy of PRD measurements, and sub-nanometer displacement sensitivity can be achieved with an appropriate setup (118, 127).

Based on the principle of interferometry, the movement of the particles could induce the Doppler effect on the interference signal (107). This means that the phase of the interference will change with the detected movements as demonstrated by figure 2.3.

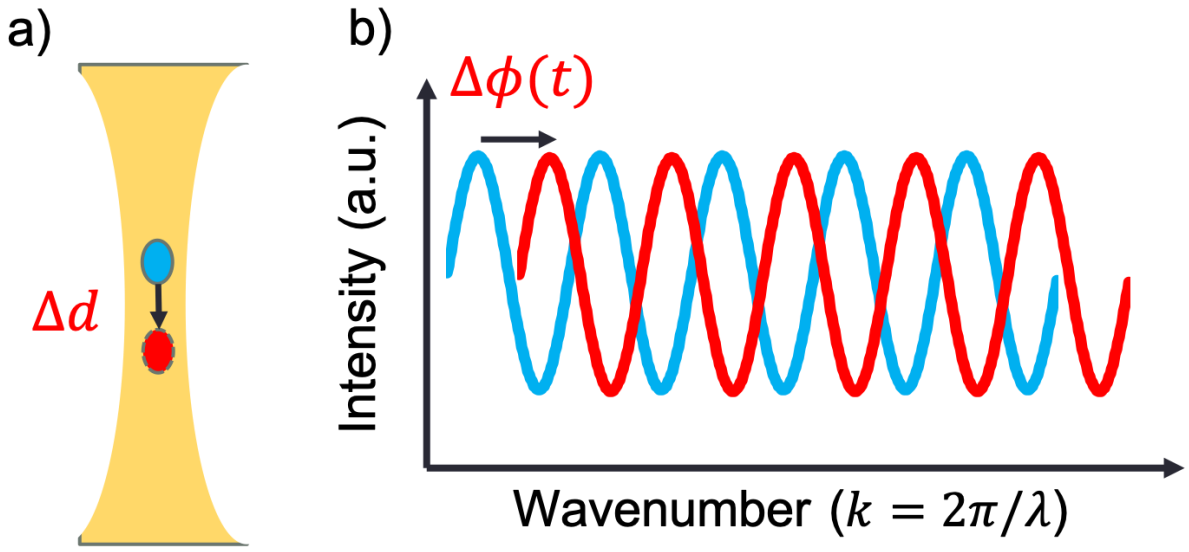

Figure 2.3 Demonstration of PRD principle. a) scatter motion between two consequent detections. b) Doppler induced phase change in the interferogram of the scatter.

The axial displacement of the scattering particles in figure 2.3a may induce a Doppler frequency shift and thereby change the phase of the corresponding cosine modulation as shown in figure 2.3b. Indeed, the average Doppler frequency shift is proportional to the phase change over time, and the relationship between phase change $\Delta\phi$ and Doppler frequency shift f_d can be show by the equation 2.13 (128).

$$f_d = \frac{\Delta \phi}{2\pi \Delta t} \quad \text{(Eq. 2.13)}$$

Where Δt denotes the time interval between two interferograms. According to equation 2.6, the phase term can be obtained from the Fourier transform of the interference signal by performing cross-correlations between subsequent interferograms or A-lines in equation 2.14,

$$\Delta \phi = \arctan \frac{Im(A_{x+1,z})Re(A_{x,z}) - Im(A_{x,z})Re(A_{x+1,z})}{Re(A_{x+1,z})Re(A_{x,z}) + Im(A_{x,z})Im(A_{x+1,z})} \quad \text{(Eq. 2.14)}$$

Where $A_{x,z}$ denotes the complex number at lateral location x and axial location z which is generated by Fourier transforming the raw interference signal. Additionally, the average phase change over multiple A-lines can be calculated using equation 2.15.

$$\Delta \bar{\phi} = \arctan \frac{\sum_{x=1}^{X} \sum_{z=1}^{Z} [Im(A_{x+1,z})Re(A_{x,z}) - Im(A_{x,z})Re(A_{x+1,z})]}{\sum_{x=1}^{X} \sum_{z=1}^{Z} [Re(A_{x+1,z})Re(A_{x,z}) + Im(A_{x,z})Im(A_{x+1,z})]} \quad \text{(Eq. 2.15)}$$

Where X and Z respectively denotes the size of the averaging window in the A-line and depth directions respectively. Increasing the size of the averaging window can effectively enhance the SNR for phase measurement and increase the sensitivity, but will possibly sacrifice either the spatial resolution or the detection speed. With the phase change over time, the Doppler frequency shift can be obtained by combining the equation 2.13 and 2.14, and allows for the quantification of the velocity v using the principle of Doppler theory defined in equation 2.16.

$$f_d = \frac{2v\cos\theta}{\lambda_0} \quad \text{(Eq. 2.16)}$$

Where λ_0 is the center wavelength of the detection beam and θ is the angle between the light beam and the particle movement direction. It is obvious that this Doppler based method can only detect motion in the beam direction, and thereby maximum sensitivity is achieved only when the detector and the movement directions are in parallel (107, 112). Incorporating the equation 2.16 into 2.13, the relationship between the phase change and the speed can be achieved and demonstrated in equation 2.17.

$$v = \frac{\lambda_0}{4\pi n cos\theta} \frac{\Delta\phi(t)}{\Delta t} \quad \text{(Eq. 2.17)}$$

According to equation 2.17, the speed of the sample v, is proportional to the rate of the phase change, $\Delta\phi(t)$, in the interference signal. In the equation, λ_0 is the center wavelength, n denotes the reflective index of the medium, and Δt represents the interval between the subsequent A-lines. Additionally, the direction of the movement can be obtained from the positive or negative phase change, $\Delta\phi(t)$ .After calculating the velocity of the sample, we can obtain the displacement, Δd, by integrating the expression with respect to time as shown in equation 2.18.

$$\Delta d = \int \frac{\Delta\phi(t)\lambda_0}{\Delta t 4\pi n cos\theta} dt \quad \text{(Eq. 2.18)}$$

From the equations, we can see that the resolution of the displacement or the velocity measurement depends on the ability to resolve minute changes in the phase. This parameter is primarily determined by the voltage resolution and the sampling frequency of the digitizer, but is also heavily affected by noise in the interferogram. According to equation 2.17, the dynamic range of the velocity detection is determined by the detection interval since the range of the phase variation is limited to ($-\pi$, π), and the maximum detectable velocity is thereby proportional to the reciprocal of the interval as shown in equation 2.19.

$$v_{max} = \frac{\lambda_0}{4n cos\theta} \frac{1}{\Delta t} \quad \text{(Eq. 2.19)}$$

Where the $\Delta\phi(t)$ term in equation 2.17 is substituted with π, the maximum phase change, and cancels out the π term in the denominator. Although increasing the detection speed can widen the dynamic range, it will result in a smaller phase change over velocity ratio, and therefore sacrifice the sensitivity. Since there is a tradeoff between the dynamic range and the sensitivity for PRD detection, it is essential to find a balance for the most suitable combination depending on the imaging application.

Although sensitivity is primarily determined by the detection speed, the bottle neck for sensitivity enhancement is the noise in the phase term (118, 127, 129). A motion induced phase change that is smaller than the variant noise will not be successfully identified by the PRD algorithm (118, 127, 129). There are many risk factors that contribute to noisy variations in the phase term of the interference signal. Random fluctuations in the optical path lengths of the reference and sample arms may introduce unwanted phase shifts in the interferogram, while variations in the voltage supply of the electrical system can also add noise to the interference signal through the digitizer (118). Meanwhile, the inherent instability of the laser source could impose variations directly on the phase measurements over the entire bandwidth (118, 127). Therefore, it is important to mechanically stabilize the optical system, utilize a relatively stable power source for the digitizer, as well as carefully select and verify the specifications of the laser source.

Broadband lasers have dominated phase sensitive OCT systems in the past decade, because they provide highly stable phase performance and by association excellent displacement detection sensitivity at ~34 pm as reported in (127). However, compared to the SS laser, the CW laser cannot provide the same level of fast detection speed and is thereby inferior in terms of its dynamic range (127). Pulsed SS lasers were believed to have inferior phase stability compared to CW lasers because their wavelengths are not emitted and detected simultaneously, and the timing inconsistency over time will result in instability (120). Additionally, the majority of SS lasers provide a trigger for each laser repetition and a high frequency clock to precisely time the trigger with the emission of each wavelength. The timing jitters in the electrical trigger can also lead to variations in the phase of the interferogram and thereby deteriorate the performance of the PRD

measurements (118). However, recent studies have reported many optimization methods to enhance the phase stability of SS lasers and have demonstrated promising displacement sensitivity with the PRD algorithm using SS-OCT (118, 129-133). With these optimization techniques, SS-OCT may prove to be a better candidate than SD-OCT for certain applications that require sensitive displacement measurements.

The PRD algorithm can be readily adapted to an OCT system and provides ultra-sensitive real time displacement detection for all the scatterers within the region of interest (ROI). The sub-nanometer displacement sensitivity has enabled many functional imaging techniques that require motion detection, such as optical coherence angiography (OCA), optical coherence elastography (OCE), and Doppler spectrally encoded optical interferometry (DSEOI). Recently, we have further utilized the principles of the PRD algorithm to develop an ARF-OCE system and an SE-OCM system for the sensitive detection of ocular elasticity and ciliary activity, which will be described in detail in later chapters.

2.3 Principles of acoustic radiation force optical coherence elastography

The ARF-OCE technique follows the general principles of traditional elastography that includes excitation, detection, and parameter estimation, but utilizes a novel strategy that integrates them together to provide a high speed, ultra-sensitive, high resolution, and non-invasive elastic imaging system for in-vivo applications (34, 38, 39, 100, 112, 113, 117, 126). For excitation, the ARF-OCE system uses an external dynamic excitation method based on ARF, which in this case uses a ring-shaped ultrasound transducer to exert focused sound waves (34). The focused ARF beam is able to noninvasively penetrate into the tissue and is designed to induce an elastic

response only on the region of interest (38). A confined excitation region is essential in order to study the elasticity of structurally complex tissues, such as the posterior eye, since the elastic responses from various components may affect each other and make it difficult to distinguish the elasticity of different tissue structures (46). By placing the tightly focused ARF beam only at the region of interest and controlling for the power of the excitation, we can ensure that the elastic wave properties are dependent solely on the specific structures that are targeted. Additionally, the axial focal length of the transducer is designed to be much longer than the imaging depth of the OCT, so that a uniform excitation in the axial direction can be assumed within the FOV (113, 117, 126). The uniform ARF excitation deforms the scatterers in the axial direction so that the PRD-OCT detection can achieve the maximum sensitivity and allows for the visualization of deformations that are induced by a small ARF force (112).

According to the elastic theory, a dynamic excitation is able to generate elastic waves propagating in two different directions: the compressional wave or "p" wave propagates in the direction of the force and the shear wave or "s" wave propagates in the perpendicular directions (111, 134, 135). Both waves are able to induce displacement in the direction parallel to the force. We have previously developed a compressional wave elastography technique (CWE) (40) that analyzes the displacement amplitudes and the resonance frequency to yield quantitative mechanical contrast for the in-vivo rabbit retina. However, the quantification method requires many phantom calibrations and in turn could compromise the accuracy of the elastic measurements.

In order to improve on previous elastic imaging technology, we proposed to analyze the shear wave to quantitatively assess the elasticity of ocular tissues while using the novel confocal setup. The principle of shear wave elastography is governed by equation 2.20 (29, 48, 50, 51, 112).

$$E \approx 3\mu = 3\rho {C_s}^2 \quad \text{(Eq. 2.20)}$$

Assuming that the tissue density, ρ, is known, the equation approximates the shear modulus, μ, as the product of the density and the square of the shear velocity, C_s. Assuming that the tissue is incompressible, the Young's modulus, E, can be approximated to be three times of the shear modulus. This method is free of phantom calibrations and thereby is expected to have better accuracy than the CWE method in its elasticity measurements. Specifically, we control the ultrasound transducer to apply a pulsed ARF on the sample in the axial direction and induce a shear wave that propagates in the transverse direction in the sample. Since the excitation is considered uniform in the axial direction, the wave will propagate laterally along the retina and the lateral speed of propagation can be extracted for shear wave elasticity analysis. In order to quantitatively assess the elasticity, or Young's modulus, distribution within the tissue, it is necessary to obtain the spatial shear wave speed at each location in the sample and use a segmentation algorithm to estimate the spatial shear wave speed.

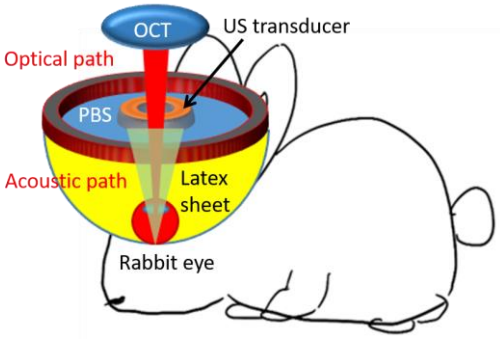

Figure 2.4 Schematic of confocal excitation and detection.

In a preliminary work, a confocal ARF-OCE technique was recently presented by our group to probe the mechanical contrast of the posterior eye in-vivo (113). Acoustic radiation force (ARF) was first used to induce an elastic wave that propagates inside the tissue. Then PRD-OCT was used to detect the wave response and quantitatively assess the elasticity by analyzing the response based on the elastic theory. The primary advantage of this set up is that the ARF-OCE system utilizes the PRD-OCT algorithm to detect deformation on the nanometer scale, and therefore a small excitation dosage is sufficient for imaging, making it safe to use on in-vivo tissues. The novelty of this design was to place the optical detection and the ultrasound excitation in parallel on the same side of imaging. The optical beam travels through the center aperture of the ring-shaped transducer and ensures confocal alignment as shown in figure 2.4 (113). Other studies have also tried to combine ultrasound excitation with optical detection but placed them on opposite sides and is thereby infeasible for in-vivo ocular applications since OCT cannot penetrate through thick tissues (48).

In summary, ARF-OCE utilizes dynamic acoustic force to induce deformation inside the sample, visualizes the spatial wave response using optical interferometric detection, accurately traces the spatial wave speed using segmentation algorithm, and finally map out the Young's modulus based on the shear wave principle. This embodiment takes advantage of the uniform penetration of ARF, micron scale spatial resolution, and sub-nanometer displacement sensitivity of PRD-OCT. These concepts will be discussed in detail in a later chapter.

2.4 Principles of spectrally encoded interferometric microscopy system

Spectrally encoded interferometry (SEI) is also an adaption of OCT that aims to perform high speed line-scan imaging at a rate equivalent to that of the OCT point scan (136, 137). The technology is able to visualize the volumetric structures of biological sample at a much faster imaging rate than OCT (138). Figure 2.5a shows a traditional SEI design,

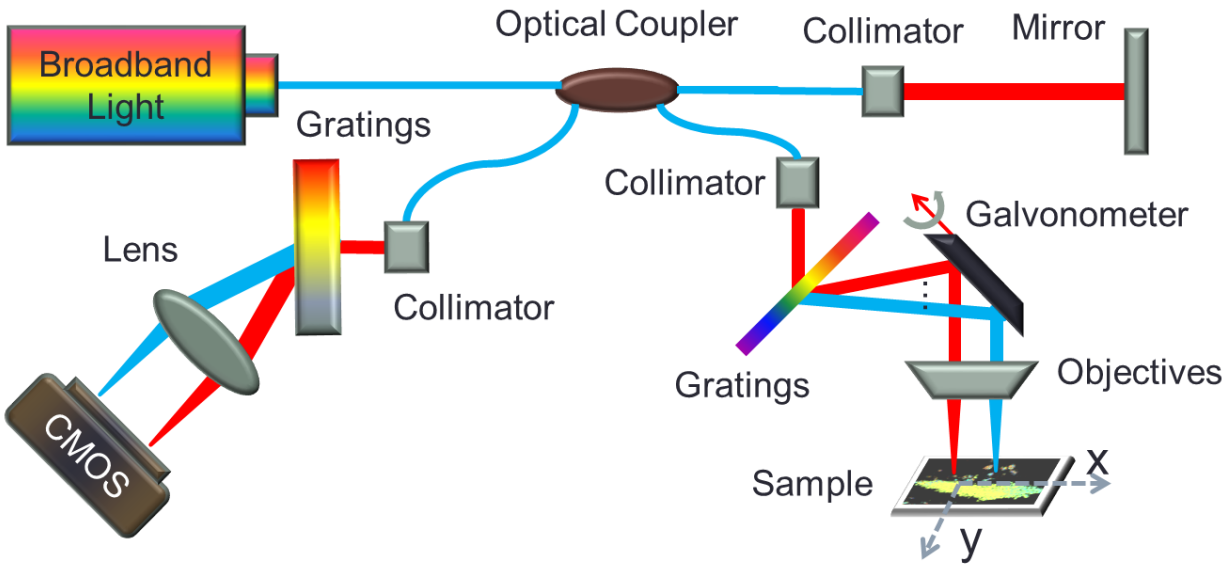

Figure 2.5 SEI based on CW laser. a) system schematic, b) line scan scheme. OC: optical coupler, CO: collimator, M: mirror, SL: scan lens, G: Galvanometer mirror, DG: diffraction gratings, L: lens, S: sample.

Where a CW laser is used to drive the system, and the interferogram is registered using a camera based spectrometer. The major difference between SEI and OCT is in the configuration of the sample arm (101). The SEI utilizes diffraction gratings (GR) to chromatically disperse the broadband laser spectrum into a line of light based on the different wavelengths (137, 139). The sample is then illuminated with the line of focused light where each wavelength encodes

structural information at each corresponding location as illustrated by figure 2.5b. By using a 1D scanner (G) to scan the line of light across the sample, the structural and displacement information can be obtained within the volumetric imaging region (140, 141).

Since SEI spatially separates the wavelengths into a line, it will have limited bandwidth at each point (138). According to the principles of interferometry and OCT, this means that the SEI trades off its axial resolution to achieve a fast scanning speed. In addition, the energy is also reduced at each scanning location since the light is dispersed into a line, so the depth of imaging may also be limited. Although the axial resolution is relatively lower for SEI, some applications do not require high axial resolution, and rather focus more on the lateral information and imaging speed. The figure 2.6 below demonstrates a typical processing algorithm to obtain the structural and displacement information from the interferogram generated by the SEI system (101, 140).

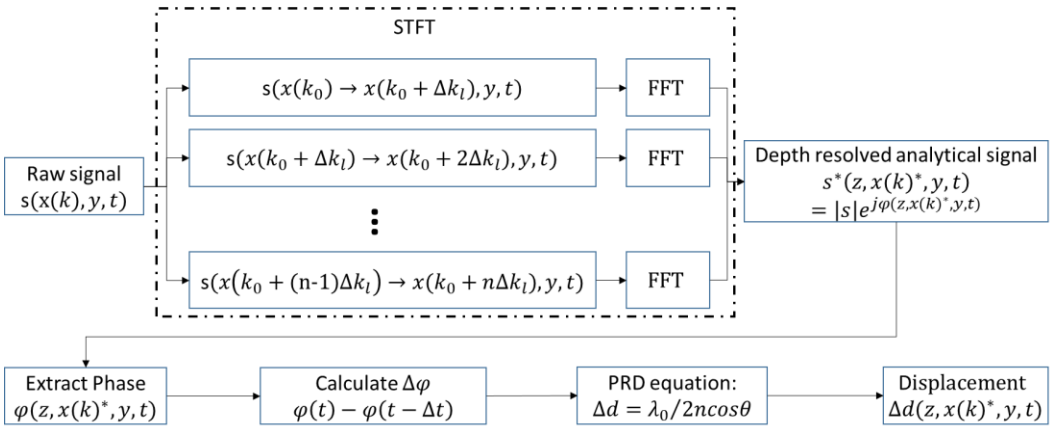

Figure 2.6 Processing algorithm for volumetric SEI. t: time, φ: phase, d: displacement, s: raw signal, x(k): fast scan axis as a function of wavenumber k, z: depth axis, y: slow scan axis, n (n=1,2,3…): index of sub-sections, Δk_l: window size of the STFT (short time Fourier transform).

In the flow chart shown in figure 2.6, the raw interferogram, S, is first divided into small sections between wavenumber $k_0 + (n-1)\Delta k_l$ and $k_0 + n\Delta k_l$ that correspond to reflections from neighboring points within the line scan, where $k_0$is the initial wavenumber, Δk_l denotes the size of each section or the spectral width distributed to each lateral location n. Next a Fourier transform over wavenumber k will be performed on every section over the spectral axis to convert the interference from wavenumber space to depth space and obtain the two dimensional intensity and the phase by analyzing the analytical signal S^*. This process is also known as a short time Fourier transform (STFT), which divides the signal into subsections and performs Fourier transform on each of them. The cross-sectional tissue structure can then be reconstructed from the depth resolved intensity profile, $|S^*|$, obtained from the STFT, while the displacement information can be mapped out by feeding the temporal phase change into the PRD equations. Again, the temporal phase change can be obtained using cross-correlation as show by equation 2.21.

$$\Delta\phi = \arctan\frac{\sum_{x=1}^{X}\sum_{z=1}^{Z}[Im(S_{x+1,z})Re(S_{x,z}) - Im(S_{x,z})Re(S_{x+1,z})]}{\sum_{x=1}^{X}\sum_{z=1}^{Z}[Re(S_{x+1,z})Re(S_{x,z}) + Im(S_{x,z})Im(S_{x+1,z})]} \qquad \text{(Eq. 2.21)}$$

The phase extraction of SEI is analogous to that of the OCT, the complex number in SEI $S_{x,z}$ is generated from the Fourier transform, the X and Z defines the averaging window size in the lateral and axial direction, and there is a tradeoff between the phase measurement quality and the spatial resolution. In addition to the tradeoffs in phase measurement, there is also a tradeoff between the axial and lateral resolutions during the processing of the SEI signal where the window size, Δk_l, is positively correlated to the axial resolution but inversely correlated to the lateral resolution. In applications where the lateral resolution is most important and axial information is relatively trivial, it is feasible to sacrifice the axial resolution to obtain en face images with the highest possible lateral resolution. However, this means that the processing

algorithm must be modified and optimized compared to the traditional SEI method, as demonstrated in figure 2.7.

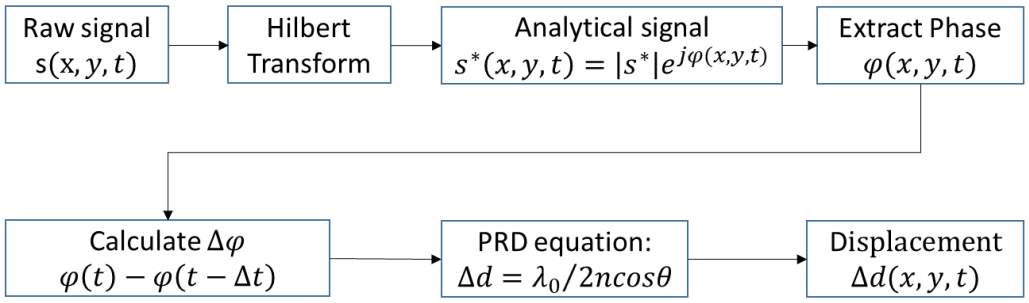

Figure 2.7 Processing algorithm for en face SEI. t: time, φ: phase, d: displacement, s: raw signal, x: fast scan axis, z: depth axis, y: slow scan axis.

Figure 2.7 demonstrates the processing algorithm that can be implemented to yield in the highest lateral resolution for an established SEI system. Instead of using the STFT to convert the interferogram to depth space, it uses a Hilbert transform to convert the interference signal to its analytical form. Each point in the analytical signal will encode the reflectivity and displacement information of its corresponding location where it focuses the light but does not have depth information due to the minimal bandwidth allocated to each location. By analyzing the phase and intensity of the analytical signal point by point, the SEI system is able to obtain the information only on a single axial focal plane but with maximum lateral resolution.

By optimizing the lateral resolution in a traditional SEI system, our group recently developed the spectrally encoded interferometric microscopy (SEIM) system to visualize the cellular activity on the tissue surface in real time. The utilization of the spectrally encoded interferometry allows for volumetric imaging that is approximately a thousand times faster than that of a traditional

OCT system. To identify the biological structures at the cellular level, the SEIM system incorporates a microscopy design that enables a flat imaging plane with a resolution around one micron. With the integration of the PRD algorithm, the SEIM system is able to identify the cellular level biological structures, detect their sub-nanometer motion dynamics, and visualize the spatial pattern of the cellular scale motion in real time.

To further enhance the lateral resolution, we have incorporated a microscopy setup and achieved close to 1 micron lateral resolution, which is much higher than the resolution of previous SEI systems. The microscopy setup uses a high NA objective lens to support for high lateral resolution and a tight focal plane in the axial direction. It also contains two optical telescopes to magnify the image and ensure a flat imaging plane on the sample, which are essential to resolve the small bundles of cilia and encompass the transversal ciliary beats. We have further optimized the design by using a swept source laser as the light source, which provides the capability to achieve much higher imaging speed than traditional SEI systems that use the CW laser. To achieve similar en-face imaging speed, traditional OCT image would require swept source laser with a swept rate over 100 MHz, which is not currently available. With a combination of these improvements, we were able to use the novel SEIM system to visualize the spatial ciliary motion patterns and dynamics for the first time. Details on this imaging technique will be discussed in a later chapter.

2.5 Summary

In summary, we have discussed the basic principles of the optical imaging systems that will be developed and optimized in this dissertation. In general, the concepts of OCT and the PRD

method have been strategically combined to develop the confocal shear wave ARF-OCE and SEIM imaging devices. These are novel functional imaging modalities that aim to solve an unmet need in the ophthalmic and respiratory fields, but also have the potential to serve other applications as well.

CHAPTER 3

Confocal shear wave ARF-OCE

This chapter discusses the preliminary results obtained using our novel confocal shear wave acoustic radiation force optical coherence elastography to study the biomechanics of the posterior eye. First we introduce how the elasticity can aid in the early diagnosis of retinal diseases in section 3.1. Then we demonstrate the setup of the imaging system in section 3.2. In section 3.3, the unique segmentation and data analysis methods that are implemented into the ARF-OCE system is discussed. Finally, we present our ex vivo and in vivo results using rabbit eye samples in sections 3.4 and 3.5 respectively. Finally, we end the chapter with a brief summary in section 3.6.

3.1 Introduction

Retinal diseases, such as age-related macular degeneration (AMD), are the leading cause of blindness in the elderly population. Since no known cures are currently present, it is crucial to diagnose the condition in its early stages so that disease progression is monitored. Recent advances show that the mechanical elasticity of the posterior eye changes with the onset of AMD. In order to measure the mechanical elasticity of the posterior eye, *ex vivo* testing methods have been popular, as well as computer modeling (8, 10, 142). Elastography methods based on magnetic resonance imaging, ultrasound, and optical coherence tomography, have been widely used in determining the elasticity of tissues (29, 143-146). Optical coherence elastography (OCE) has the advantage in ocular imaging due to its high resolution (<10 um) and the transparency of ocular tissues (117, 134, 147, 148). ARF-OCE is a method of OCE that uses ultrasound pressure for excitation, and has been advantageous in its penetration into sub-surface tissues (34, 38, 39). Although *in-vivo* corneal elastography studies have been performed, due to the

difficulty in penetrating to the posterior globe, combined with the need for high sensitivity and resolution, *in-vivo* measurements of the retinal stiffness has yet to be studied, to the best of our knowledge.

In this study, a shear wave (SW) ARF-OCE system has been developed, with synchronized ultrasound excitation and B-M mode optical detection. A custom segmentation algorithm was implemented to isolate individual retinal layers and the shear wave propagation speed at each location and depth were calculated. An *ex-vivo* porcine retina was first imaged, and the elasticity map of the central retina was obtained. In order to verify the feasibility of *in-vivo* imaging using this technology, a rabbit model was measured, and the elasticity of the different retinal layers were identified in increasing stiffness from the ganglion side to the photoreceptor portions.

3.2 System setup

A custom SD-OCT system with a central wavelength of 890 nm and bandwidth of 144 nm was used for shear wave detection for all the experiments presented here, and the spectrum of the laser is obtained from an optical spectrometer and shown in figure 3.1c. A 4.5 MHz ring ultrasound transducer is used for pulsed tissue excitation. The excitation duration was limited to 1-2 ms while the optical detection speed was 50 kHz. The optical setup and the *ex-vivo* sample setup are shown in figure 3.1a. The light emitted from the superluminescent diode is filtered through the optical isolator, and split with an optical coupler. For the safety purpose of *in-vivo* retinal imaging, 20% of the light is transmitted to the sample, which is well within the ANSI safety limits, and 80% is redirected to a reference mirror. Glass imaging windows are placed in the stationary reference arm for dispersion compensation. In the sample arm, galvo mirrors are used for B-M mode scanning, and a scan lens is used with a focal length of 54 mm to penetrate

through the ring transducer and into the posterior eye globe. The scattering signal from the sample arm is coupled together with the reflected reference arm signal and sent to the detector arm. The interference signal is separated by wavelength with a diffraction grating, and focused onto a line scan CMOS camera. The signal is processed and transformed into depth resolved intensity and phase information.

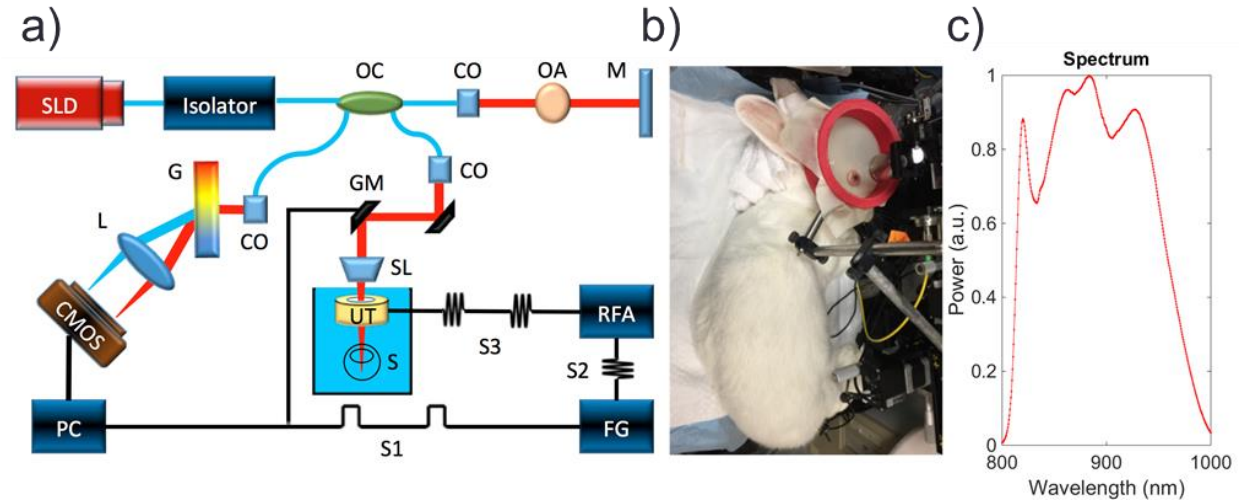

Figure 3.1. System set up for ARF-OCE. a) OCE system schematic with ex-vivo sample. b) In-vivo experimental setup. c) Laser spectrum. SLD: superluminescent diode, OC: optical coupler, CO: collimator, OA: optical attenuator, M: mirror, GM: galvanometer mirrors, SL: scan lens, UT: ultrasound transducer, S: sample, RFA: radiofrequency amplifier, FG: function generator, G: grating, L: lens, S1: baseband signal, S2: modulated signal, S3: amplified modulated signal.

A phosphate buffered saline (PBS) bath is used as the medium for ultrasound propagation as well as preservation of ocular tissue. For *in-vivo* experiments, the PBS bath is replaced with a rubber drape as shown in figure 3.1b. The ultrasound transducer was removed in figure 3.1b in order to visualize the ocular proptosis of the rabbit. The drape system imitates the steridrapes that are

widely used in clinical ultrasound. PBS is added to the draped once again to serve as the medium for propagation, as well as for lubrication of the rabbit eye.

For the shear wave excitation, a baseband signal (S1) is given by the PC to the function generator, which converts it into a modulated pulse signal. This pulse is amplified by approximately 42dB and fed to the ultrasound transducer. A pressure is applied onto the sample, initiating the propagation of the shear wave from the focal region to the peripheral areas. The detection scanning scheme is shown in figure 3.2a, where the excitation beam is given at location P0 and B-M mode detection occurs along the lateral direction from P1 to Pn. At each location, an excitation pulse of 1-2 ms is given and a series of 400 A-lines, which corresponds to 8.8 ms, is obtained in M mode before the galvanometer moves to the next location. The number of A-lines is chosen such that the entire duration and progression of the shear wave can be captured.

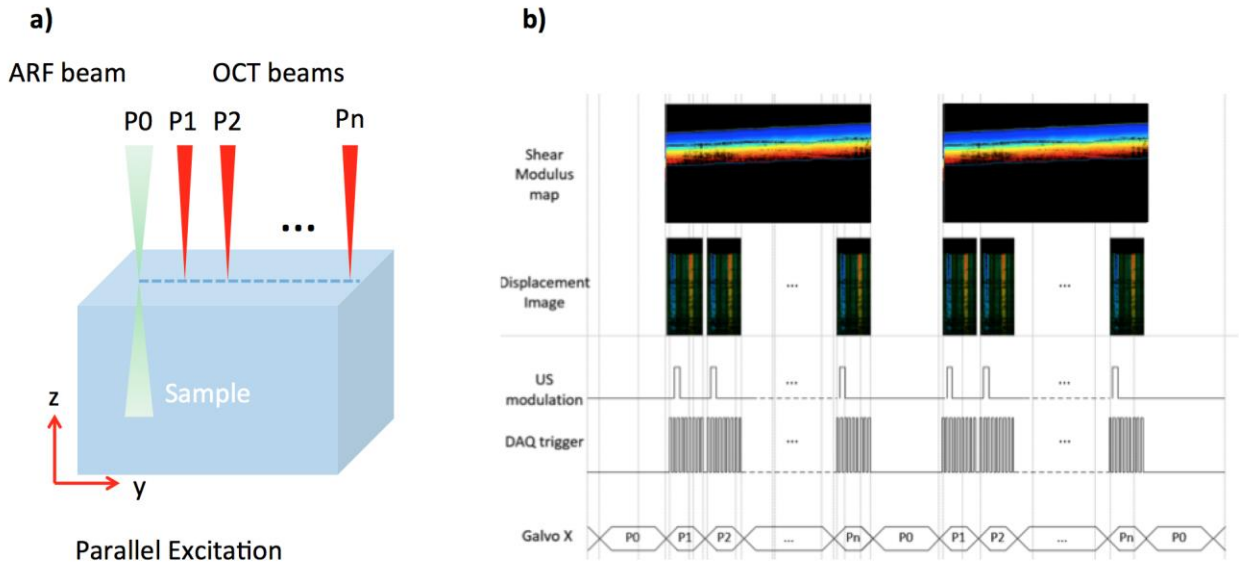

Figure 3.2. Scanning scheme. a) Scanning scheme of SW-ARF-OCE system. b) Timing diagram.

In order to achieve efficient and effective imaging, the entire excitation and detection process must be synchronized. The timing diagram is shown in figure 3.2b. To obtain a B-scan showing the full lateral scanning area, an ultrasound modulation pulse is given for every 400 A-lines while the camera DAQ trigger is given for each A-line to capture the intensity and phase information at each location for 8.8 ms total, in increments of 22 us. After detection is completed, the galvanometer moves to the next location in increments of 1.5 um, which is well within the lateral resolution of the optical system. The M-mode displacement image is obtained at every B-scan location, and the phase-resolved displacement is post-processed to obtain the shear modulus map.

Within the 400 A-lines in M-mode at each location, the entire shear wave propagation through that point can be captured. In figure 3.3a-c, a sample raw data for the porcine retina is shown, where it is apparent that different locations on the retina correspond to different propagation speeds. The transducer focal area is on the left side of the images, and propagation is to the right. For example, the bottom most layer propagates the fastest, and corresponds to a stiffer tissue component. It is also important to note that the ultrasound wave intensity decreases at regions of stiffer tissue, and the intensity of the displacement is not considered in the velocity calculations.

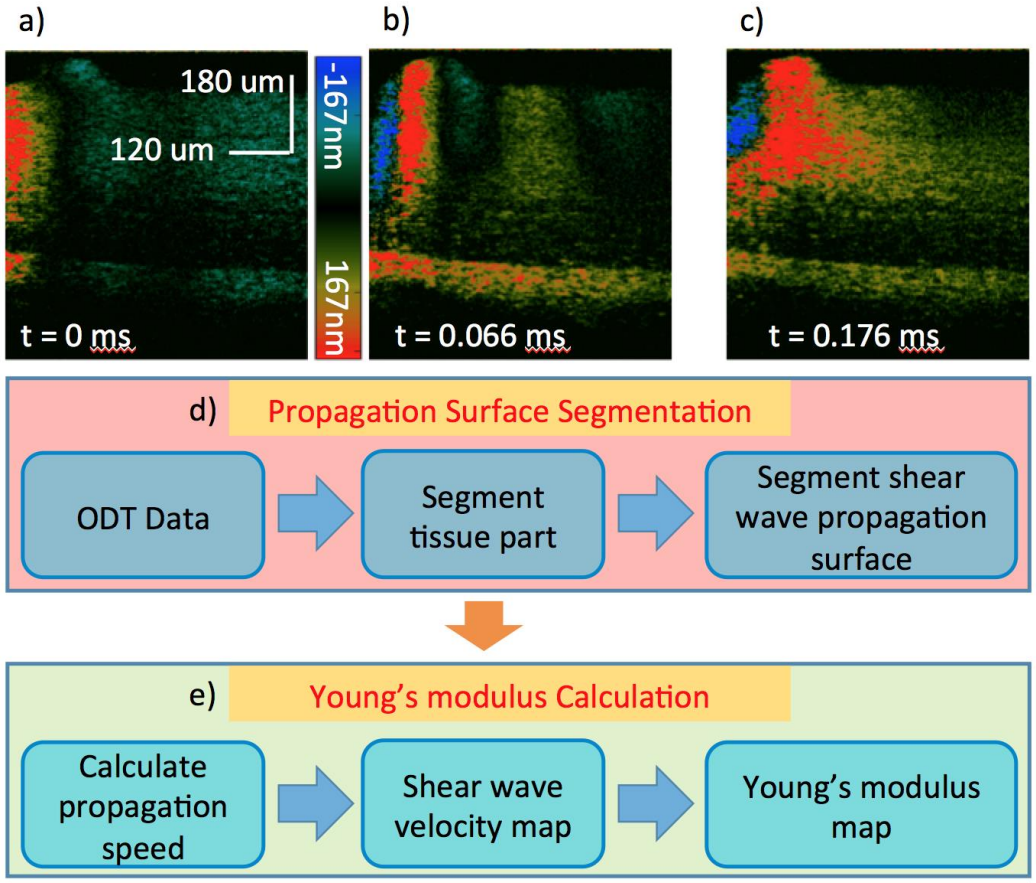

Figure 3.3. Demonstration of shear wave and analysis flow chart. a-c) Raw data showing wave propagation of retinal layers at different time points. d-e) Flow diagram demonstrating post-processing of raw data.

After the raw data is obtained, post-processing is performed to segment the layers and calculate the shear wave propagation speed. As shown in figure 3.3 d-e, the OCT intensity and Doppler phase data is first obtained, and the OCT image is segmented based on a custom segmentation algorithm to isolate different retinal layers. Then the segmented layers are applied to the displacement map, where the shear wave propagation surfaces for each layer is segmented as well. Next, the propagation speed is calculated for each location based on the slope of the segmented wave propagation for each layer. The velocity is based on the change in location over

the time period, and the shear wave velocity map can be obtained. Figure 3.4 shows the flow chart to map out the spatial shear wave speed using segmentation algorithm.

First, we use the algorithm to identify and isolate the data of different retinal layers as shown by figure 3.4a. Then, we segment and reslice the data of each layer along the depth direction, and generate images showing the spatial temporal shear wave propagation shown in figure 3.4b. After, the segmentation algorithm is utilized to trace shear wave propagation and achieve the arrival time of shear wave to each y position. Finally, we can map out the spatial shear wave speed in figure 3.4c by estimating the slope of the segmented shear wave trace as shown in the green line of figure 3.4b.

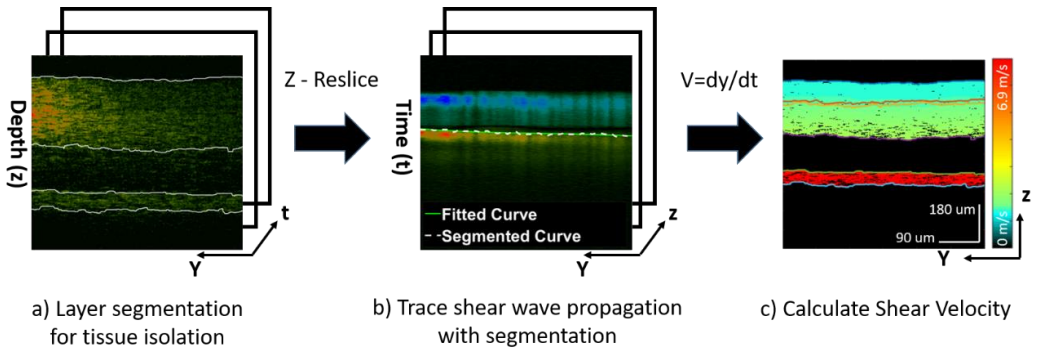

Figure 3.4 Flow chart of using segmentation to trace shear wave propagation. a) layer segmentation to isolate data from each retinal layer. b) Using segmentation to achieve the times when a shear wave reaches to different positions in y axis. c) Calculate the spatial shear wave speed by estimating the slope of the shear wave trace identified by the segmentation in (b).

The relationship between the velocity, C_s, and the shear modulus, μ, can be described with the equation, $\mu = \rho {C_s}^2$, where ρ is the tissue density of approximately 1 kg/m^3. The elastic modulus

is approximately 3 times the shear modulus as demonstrated by previous literature (149), and can be calculated and mapped out. The segmentation and data analysis method will be discussed in detail in the next section.

3.3 Segmentation and data analysis method

Under the context of 3-D segmentation with dynamic programming, the problem of edge detection is resolved by searching for the shortest pathway within a graph constructed upon the images of interest. The general principle of this segmentation algorithm, including the graph construction, search region define and the shortest path search, has been explained in previous publications (150). In this dissertation, we have optimized the traditional 3-D DP algorithm and developed a threshold free search region method as show by figure 3.5.

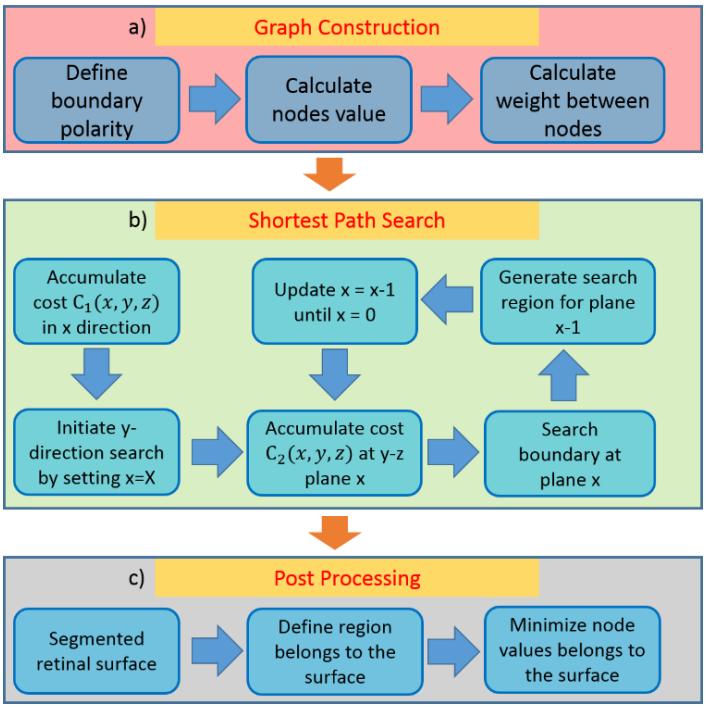

Figure 3.5 3-D DP segmentation algorithm with adaptive search region.

Assuming that $V(x, y, z)$ is the normalized axial gradient of the volumetric OCT data with dimensions $X \times Y \times Z$, where $X, Y, \text{and } Z$ represent the data pixels in the directions of the fast scan, slow scan, and the axial depth. The variables shown in figure 3.5 can be defined as below.

$$C_1(x, y, z) = \min_{-d_1 \le i \le d_1}\left(C_1(x-1, y, z+i) + \alpha_1|i| + w(i, x, y, z)\right) \quad \text{(Eq. 3.1)}$$

$$C_2(x, y, z) = \min_{-d_2 \le i \le d_2}(C_1(x, y-1, z+i) + \alpha_1|i|) \quad \text{(Eq. 3.2)}$$

$$I(x, y, z) = \quad \operatorname{argmin}_{-d_2 \le i \le d_2}(C_1(x, y-1, z+i) + \alpha_1|i|) \quad \text{(Eq. 3.3)}$$

$$w(i, x, y, z) = 2 - G(x, y, z) - G(x-1, y, z+i) + w_{\min} \quad \text{(Eq. 3.4)}$$

$$B(x, Y) = \operatorname{argmin}_{1 \le z \le Z} C_2(x, Y, z) \quad \text{(Eq. 3.5)}$$

$$G(x, y, z) = V(x, y, z) \quad \text{(Eq. 3.6)}$$

As a graph based method, the algorithm specifies the $V(x, y, z)$ values as the nodal value, $G(x, y, z)$, and measures the length between adjacent nodes using the weight function, $w(i, x, y, z)$, as shown in equation 3.4. In addition, the connectivity between nodes is defined so that each node is only accessible to pixels immediately before and after the node of interest in the searching direction. Parameters d_1 and d_2 determine the number of available adjacent voxels during the x and y directional path searches respectively. Other parameters such as α_1 and α_2 are used to control the smoothness of the segmented surface.

$$w(i, x, y, z) = 2 - G^*(x, y, z) - G^*(x-1, y, z+i) + w_{\min} \quad \text{(Eq. 3.7)}$$

$$G^*(x, y, z) = \begin{cases} P \times V(x, y, z) & \text{if } P \times G(x, y, z) > 0 \\ A \times P \times V(x, y, z) & \text{if } P \times G(x, y, z) \le 0 \end{cases} \quad \text{(Eq. 3.8)}$$

$$P = \begin{cases} 1 & \text{when segmenting positive gradient surface} \\ -1 & \text{when segmenting negative gradient surface} \end{cases} \quad \text{(Eq. 3.9)}$$

Different OCT intensities in each layer result in different gradient polarity values for each boundary, which allows for further separation between the positive and negative gradient boundaries. Accordingly, we modify the graph construction method to consider the gradient

polarity as shown in equations 3.7-3.9. Parameter P defines the polarity of the boundary and the sign of the nodal values, $G^*(x, y, z)$, so that only the nodes with either positive or negative values are selected at one time during the search. In essence, the nodes on boundaries with an opposite polarity value will result in a higher path cost to the weight function than the ones on the boundary of interest, and will not yield in the shortest path. It is possible to add an arbitrary constant, A, to magnify the punishment from going through unwanted boundaries during the search.

3-D DP is used to solve for the shortest path through breaking down the optimization process into iteratively small steps where the path cost to each consecutive voxel is always minimized. The algorithm starts by searching through the volumetric data in the x direction, generating the shortest path cost to reach each voxel as denoted by $C_1(x, y, z)$. Then, this cost function is utilized to search for the shortest path cost in the y direction, represented by $C_2(x, y, z)$, through each individual voxel. Equations 3.1 and 3.2 illustrate the searching process for each voxel, where the DP algorithm generates the shortest path by pairing it with the backward voxel that yields in minimum accumulative cost. Additionally, the path cost is accumulated simultaneously within all the planes that are parallel to the searching direction. The axial index of the paired voxel is stored in matrix $I(x, y, z)$, so that path way can be retrieved once the terminal is established. The algorithm finishes at plane y = Y, where the terminal of the overall shortest path can be generated by finding the location of the axial minimums from the cost function $C_2(x, y = Y, z)$ in the y direction as described in equation 3.5. All other boundaries can be generated by back tracing the connected voxels within matrix I as shown by equation 3.10.

$$B(x, y) = I(x, y + 1, B(x, y + 1)),\ 1 \le x \le X, 1 \le y \le Y - 1 \qquad \text{(Eq. 3.10)}$$

Since the searching algorithm does not prevent the shortest path from going through several different boundaries, a rough region must be defined before starting a search. Previous publications use thresholds to isolate different boundaries, but different imaging conditions greatly limit the effectiveness of the predefined thresholds. Therefore, we proposed a novel addition to the algorithm by defining and adapting the search region based on the searching history. More specifically, the y-direction cost accumulation and boundary detection, which was previously performed in parallel within each y-z plane, will be accomplished in a preset order so that the first segmented boundaries can serve as references to define the search region for the following boundaries.

While searching for the shortest path with this method, the boundary at the y-z plane where x = X will be segmented first and used as a reference. Since the corresponding cost function, $C_2(x = X, y, z)$, is accumulated through the entire volumetric data, the shortest path will most likely converge to a single boundary. Given that the inter-frame distance is on the micron scale, we can assume that the layer boundary in the adjacent y-z plane where $x = X - 1$ resides in a small region that is centered by the reference boundary. Therefore we can constrain the search region for this boundary and all other boundaries within a single surface by performing this process iteratively.

After one surface is segmented, the gradient values of the surrounding regions must be minimized to prevent them from interfering with the segmentation of other surfaces. We find that the axial gradient profile across a boundary tends to have a skewed Gaussian distribution, with a peak at the boundary position. Therefore, we can split the profile based on the peak position and

then fit them to two Gaussian functions to obtain the corresponding FWTM (full width tenth maximum). Finally, the gradient values are attenuated within this region by a factor of K. The thickness of the segmented boundary is given by the FWTM of the fitted curve.

Using this method, we are able to segment the 1st, 2nd, 4^{th}, and 7th positive gradient surfaces first and then the other three surfaces in between. Since we are not using the threshold method to limit the search region prior to the segmentation, it is computationally extensive to calculate the cost functions when searching across the entire volumetric graph. In order to adapt the automatic segmentation method for clinical translations, it is crucial to improve the processing speed of the algorithm. One solution was to accelerate the dynamic programming method by incorporating a Graphics Processing Unit (GPU). The code has been implemented using CUDA 7.0 (VS 2013) on an NVidia GTX980 GPU card, which yields in a segmentation speed of less than two seconds per surface over a 400x500x600 pixel volumetric data size. Using the accelerated processing system, we successfully segmented the layers of porcine retina.

Overall, the 3D dynamic programming gives out an accurate segmentation method for most layers of the porcine retina, with the exception of the 5th layer. We suspect that this gradient-based segmentation method may be overly sensitive to speckle noise that could overwhelm the boundary gradient of a weak scattering layer. Therefore, we introduce the intensity based random walker segmentation method to refine the boundaries (151). Random walker is a supervised segmentation method that requires prior knowledge (151). In the context of retinal segmentation, the segmented boundaries from 3D dynamic programming are used to generate seeds for the random walker segmentation. Seeds are pixels that are labeled to specific layers, which can be

used by the segmentation algorithm to identify all other unlabeled pixels. The figure 3.6 below shows the segmentation results before and after random walker refinement, where dotted lines represent seeds.

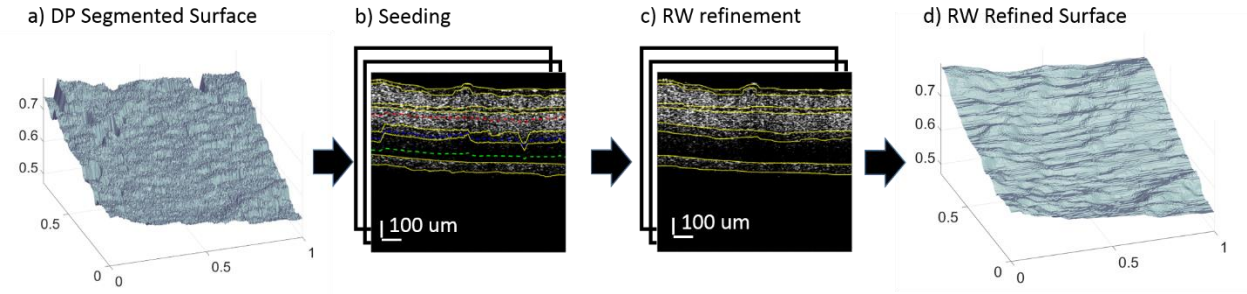

Figure 3.6 Flow chart of Random walker refinement.

The segmentation algorithm allows for the isolation of individual layers and analysis of the elasticity of each layer. We have validated the segmentation algorithm by using it to aid for the analysis of compressional wave based elastography. The cross sectional elastography using compressional wave has been illustrated in our previous publication, but the elasticity distribution in transversal directions has not been studied. Figure 3.7 demonstrates a processing method that is able to map out the transversal distribution of the mechanical property in each retinal layer based on the segmentation algorithm discussed in this section.

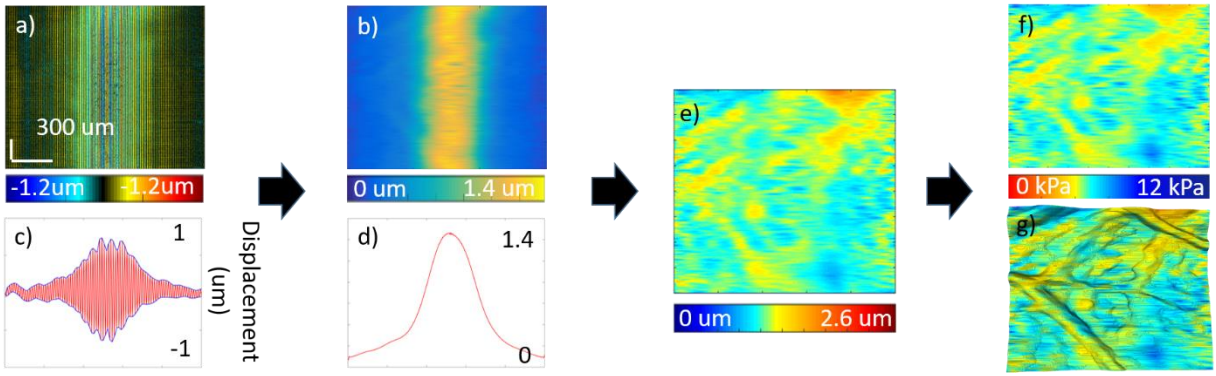

Figure 3.7 Flow chart for layer specific elasticity analysis algorithm

Figure 3.7a shows the raw en face PRD images obtained using the CWE method, where the modulated excitation as well as the bulk motion within the PRD data overshadows the useful information. In order to eliminate the unwanted modulation and noise caused by bulk motion, we extract the envelope of every horizontal OCE data. This allows us to eliminate both the bulk motion and modulation by estimating the envelope amplitude at each point. The envelope was achieved by linearly interpolating the peak points in the horizontal OCE data as illustrated by figure 3.7c.

The modulation free OCE image is shown in figure 3.7b, where the lateral ultrasound focal region is limited and results in a non-uniform displacement distribution in the transverse direction. In order to estimate the relative elasticity within the entire field of view, calibration must be performed. This can be accomplished by dividing every horizontal line of data by the vertically averaged displacement profile, assuming that the averaged profile is proportional to the excitation force distribution in the horizontal direction. We can further improve the calibration accuracy by using the actual ultrasound force field instead of the averaged displacement profile.

The calibrated en face image allows for the layer specific elasticity analysis over the transversal direction, indicating the presence of a mechanical elasticity difference between different biological components. By overlaying the en face elasticity map on the segmented surface with visual tool kits 7.0.0, we are able to relate the anatomical structures of the retinal layers to their mechanical properties as shown in figure 3.7g. For example, healthy regions of the retina tend to have lower displacement values than diseased regions with lipid formation or neovascularization in the posterior eye, meaning that the healthy regions have stiffer elastic properties.

An ex-vivo porcine eye was used to validate the feasibility of the automatic 3D segmentation algorithm, where 400x500x600 volumetric OCT data were taken from the central retinal region with dimensions of 1.5 mm by 2.4 mm. The porcine sample was held in place by a gelatin phantom, and the anterior segment of the eye was removed before imaging. The 3D structure of the retina was visualized by the OCT detection and rendered in figure 3.8a. To analyze the layer specific mechanical and structural characteristics, segmentation was performed using the proposed method. The segmented surfaces were rendered in figure 3.8b, where seven different layers can be identified and distinguished. To compare the performance of the segmentation results before and after the random walker refinement, results for 3 OCT images that are 300 um apart from each other are shown in figures 3.8c-3.8h. Specifically, figures 3.8c-3.8e show the segmentation results from the DP algorithm alone, while figures 3.8f-3.8h show the effects of the boundary refinement with the random walker segmentation on a same set of images. It is clear that the random walker refinement method yields in relatively smooth boundaries and tends to be more robust at layers with weak scatterers, as indicated by the boundaries between layers 4, 5, 6

and 7. On the other hand, the DP algorithm seems to be more sensitive to local geometrical variations and produces reliable segmentation at some boundaries.

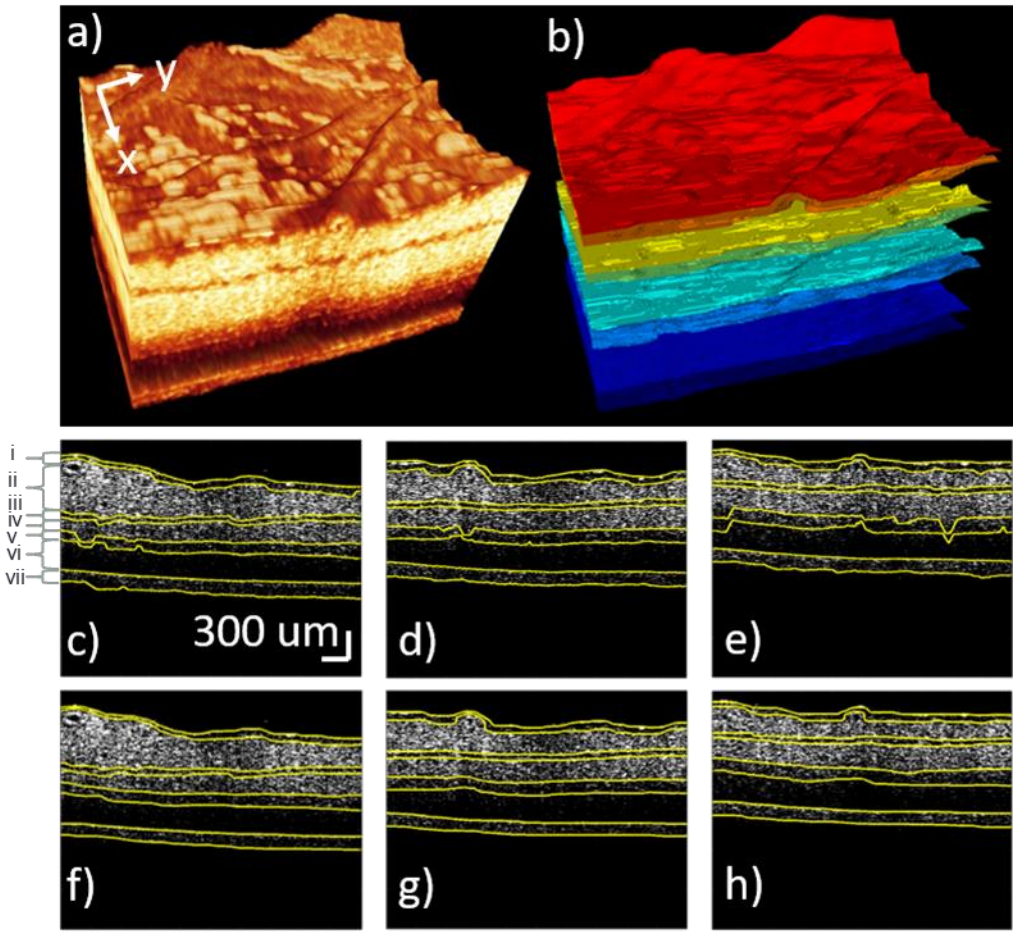

Figure 3.8 Segmented Retinal layers before and after random walker refinement. a) Volumetric render of retinal OCT data, b) Segmented retinal surfaces, c-e) Segmentations obtained with dynamic programming algorithm. f-h) segmentations obtained with random walker algorithm at corresponding locations in c-e). i) nerve fiber layer, ii) ganglion cell layer, iii) inner plexiform layer, iv) inner nuclear layer, v) Outer plexiform layer, vi) Outer nuclear layer, vii) photoreceptor inner/outer segments.

The layer specific elasticity analysis algorithm can then be performed on the volumetric PRD data of each isolated layer to obtain calibrated displacement measurements. Furthermore, the calibrated displacement and thickness of all retinal layers, together with the bulk modulus, can be fed to the spring model described in previous publications (126), and yields in quantified Young's modulus maps of each individual layer. Lastly, the overlaid elasticity map for all seven layers can be generated, where the layer specific elastograms are drawn on the 3D rendered images of the segmented surface. As shown in figures 3.9a-3.9f, the morphology of each layer can be clearly visualized, and the retinal layers gradually increase in stiffness from the top ganglion layer to the bottom photoreceptor layer. The overlaid elastogram allows for spatial correlation of retinal structures and compositions with their mechanical properties. In the overlaid elastogram, localized elastic variations were observed mostly around the retinal blood vessels and indicate that the surrounding retinal tissue is stiffer than the blood vessels.

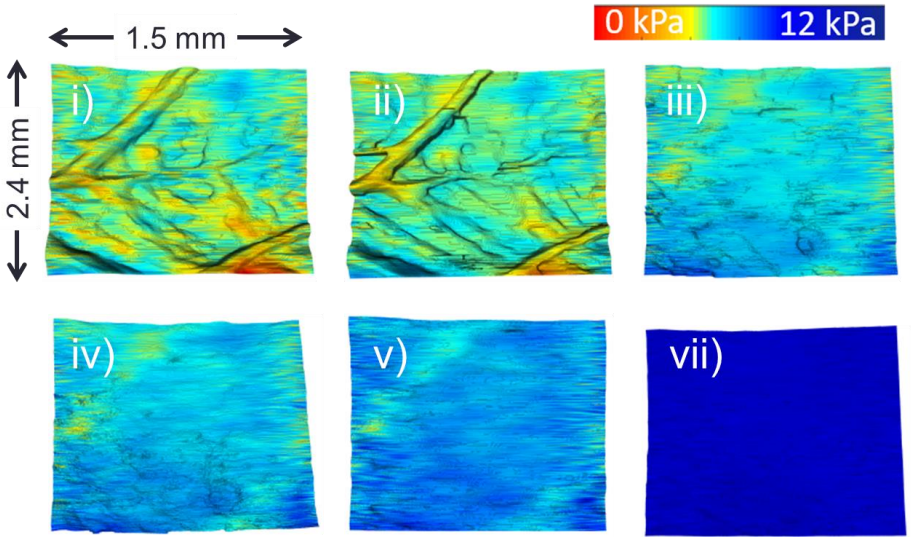

Figure 3.9 Spatial distribution of elasticity of different retinal layers. i) nerve fiber layer, ii) ganglion cell layer, iii) inner plexiform layer, iv) inner nuclear layer, v) Outer plexiform layer, vii) photoreceptor inner/outer segments. layer vi is omitted due to low OCT scattering signal.

We can summarize the layer specific elasticity in Table 3.1. The elasticity increased from approximately 5 kPa on the ganglion side to over 30 kPa on the photoreceptor side. Since the photoreceptor side is close to the sclera of the eye globe, it is expected to be stiffer. The close-knit structure of the retinal layers most definitely interferes with the mechanical elasticity for each layer and is demonstrated by the gradual gradient increase in the elasticity over the layers. Using this segmentation method, we progressed to additional retinal imaging experiments with the novel confocal shear wave ARF-OCE system.

Layer	Mean	Std
i	4.62	0.62
ii	4.66	0.51
iii	5.42	0.86
iv	5.83	0.96
v	6.88	1.3
vi	N/A	N/A
vii	30.06	5.96

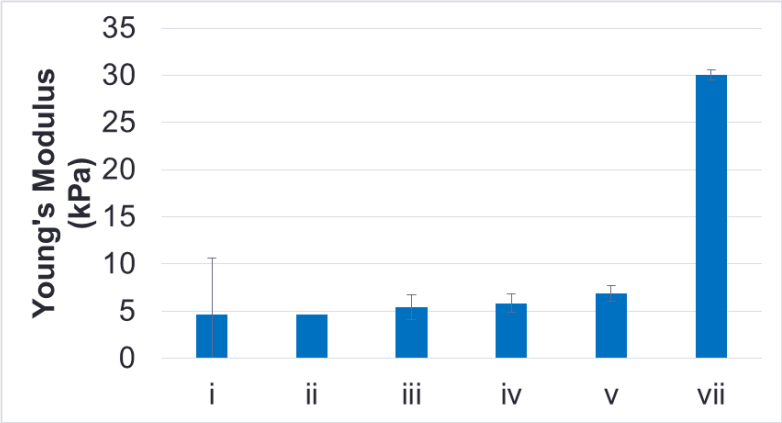

Table 3.1 Summarized layer specific elasticity. i) nerve fiber layer, ii) ganglion cell layer, iii) inner plexiform layer, iv) inner nuclear layer, v) Outer plexiform layer, vii) photoreceptor inner/outer segments. layer vi is omitted due to low OCT scattering signal.

3.4 Ex vivo retinal imaging results

As a first step, imaging was performed on an *ex-vivo* porcine retina. The porcine eyeball was obtained within 24 hours of death. Since the eyeball was no longer fully transparent due to fast degradation, the anterior portion of the eye including the cornea and the lens were removed along the iris. The vitreous was still attached to the retina, and was kept in place during imaging to

avoid retinal detachment. A 0.8% agar phantom was molded around the posterior globe and used to keep the eye in place during imaging, as well as to help preserve the shape of the posterior globe and prevent detachment. The sample was kept in phosphate buffered saline during imaging to preserve freshness and as a medium for ultrasound propagation. The eye was fixed in 10% formalin solution directly after imaging and processed for histological analysis.

The central retina region approximately 2 mm from the optic nerve on the temporal side was identified and imaged. The results are shown in figure 3.10. The OCT intensity map is shown in figure 3.10a, where segmentation was performed and 5 different layers were isolated. Next, the corresponding shear wave velocity map and elastogram were calculated according to the above algorithm, and shown in figure 3.10b and 3.10c, respectively. Finally, an H&E histology slide of a porcine retina is shown in figure 3.10d, where the 5 layers could be matched. Layer iv was omitted during the analysis due to low OCT scattering signal in the outer nuclear layer.

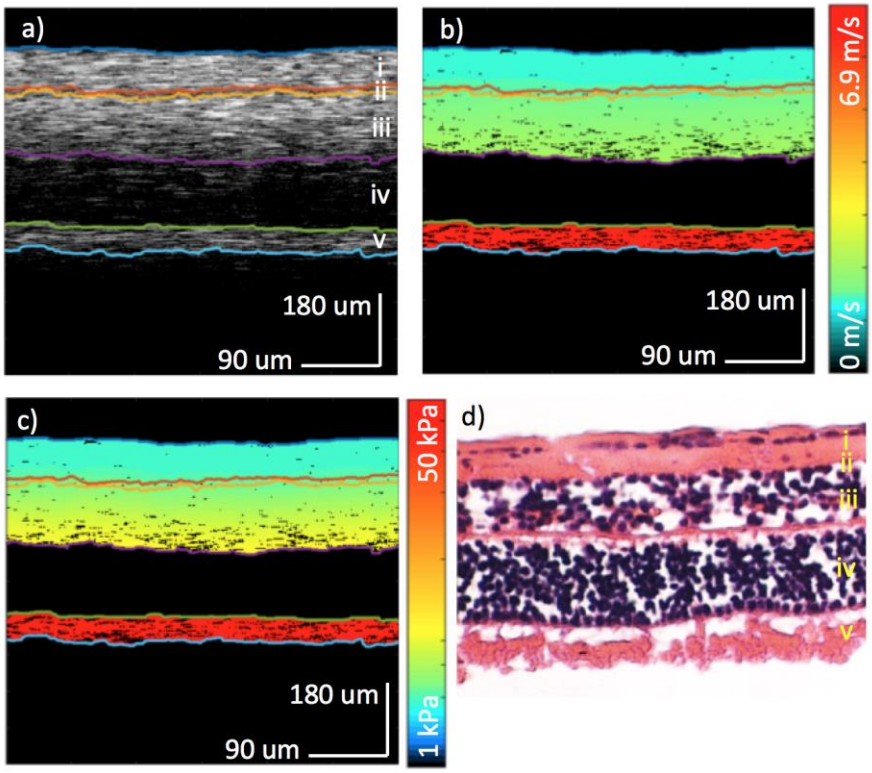

Figure 3.10. Ex-vivo porcine retina results. a) OCT of porcine central retina. b) Velocity map of shear wave propagation. c) Elastogram of corresponding region. d) H&E staining of porcine retinal layers. i: optic nerve fibers & ganglion cell layer, ii: inner plexiform layer, iii: inner nuclear layer & outer plexiform layer, iv: outer nuclear layer, v: photoreceptors.

The elasticity results of the porcine retina are summarized in table 3.2, where the mean and standard deviation for each layer is listed and plotted. The elasticity increased from approximately 6 kPa on the ganglion side to over 140 kPa on the photoreceptor side. Since the photoreceptor side is close to the sclera of the eye globe, it is expected to be stiffer. The close-knit structure of the retinal layers most definitely interfere with the mechanical elasticity for each, and is demonstrated by the gradual gradient increase in the elasticity over the layers.

Layer	Mean	Std
i	1.93	0.098
ii	2.23	0.086
iii	3.33	0.655
iv	N/A	N/A
v	47.5	1.39

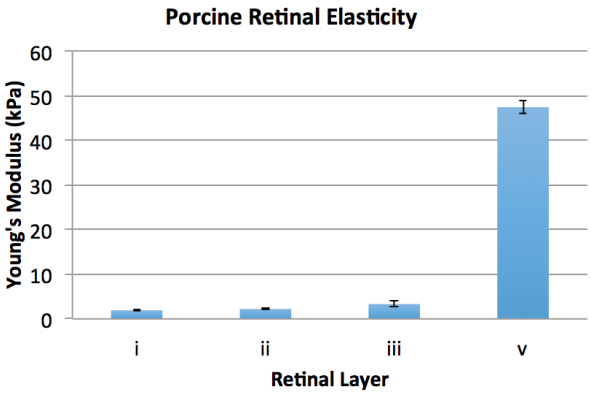

Table 3.2 Summary of *ex-vivo* layered specified elasticity. Layer iv has been omitted due to low OCT signal in the outer nuclear layer.

3.5 In vivo retinal imaging results

Although the elasticity contrast between different retinal layers is apparent in the *ex-vivo* porcine model, the presence of intraocular pressure and blood vessel perfusion is lost. Therefore, it is not an accurate representation of the retinal structure in its natural environment. In order to address these issues, an *in-vivo* rabbit model was designed and imaged. This particular rabbit is used for AMD studies, and a localized portion of the retina was damaged. For this shear wave elastography study, a relatively healthy and unaffected region of the central retina was chosen. The rabbit was put under anesthesia according to protocol and proptosed in the imaging setup as shown in figure 3.1b. All rabbit experiments were performed according to the University of California, Irvine (UCI) Institutional Animal Care and Use Committee (IACUC) protocol.

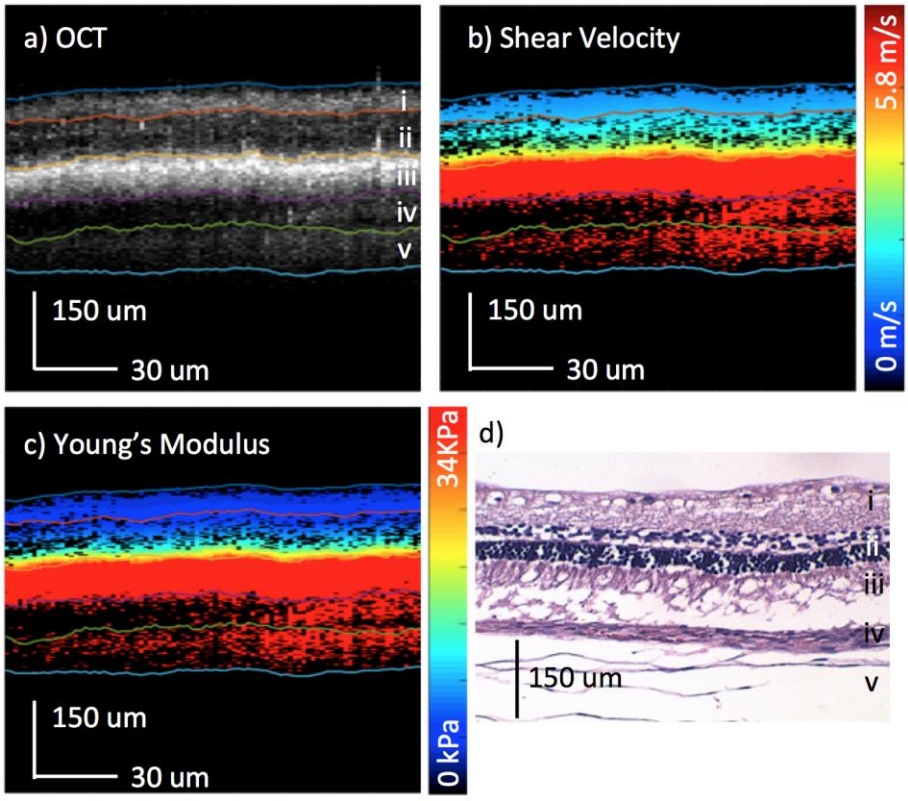

Figure 3.11. *In-vivo* rabbit elastography results. a) OCT of rabbit central retina. b) Shear wave velocity map. c) Elastogram of corresponding region. d) H&E histology, showing some retinal detachment.

Imaging was performed on the central retina approximately 1.5 mm on the temporal side from the optic disc. The same B-M mode scanning scheme was used to capture the shear wave propagation. The OCT intensity image is shown in figure 3.11a, where segmentation was performed to isolate 5 different layers in the posterior globe. The shear velocity map is demonstrated in figure 3.11b and a speed of up to 5.8 m/s can be visualized. The velocity was converted to the Young's modulus in figure 3.11c. The elasticity of the 5 layers from the ganglion side to the photoreceptor side are: 12.6±1.5, 35.7±18.9, 101.1±5.1, 102.3±4.8e-9, 102.3±5.7e-9 kPa. The bottom 2 layers of the eye could not be differentiated due to the fast propagation speed.

According to the histology, the bottom two layers are close to the sclera, and are expected to be stiffer than the retina and have a higher propagation velocity. The shear wave propagated for approximately 135 um in the lateral direction before it was attenuated.

After the rabbit was euthanized, the posterior globe was fixed and processed for histological analysis. H&E staining is shown in figure 3.11d, where the layers of the retina can be corresponded to the OCT figure similar to literature (152). The retinal detachment is likely a fixation artifact, while the swelling in the sclera or layer v is caused by the repeated proptosis procedure. Three layers of the live rabbit retina have been distinguished with different elasticity values. The feasibility of using the SW-ARF-OCE method to probe the mechanical properties of the retina has been confirmed. Further retina studies will be performed to measure the elasticity change with disease progression.

The primary advantages of the system are its non-invasive nature and its adaptability to clinical imaging. OCT and ultrasound are readily used in ophthalmic clinics today. Ultrasound gel and steridrape based waterbath are commonly used in clinics currently to couple ultrasound into the eye, and is easily adaptable in the translation of our technology. This technology will allow researchers and physicians to study the mechanisms behind changes in the mechanical elasticity of the retina during disease onset and progression, which is crucial in both basic pathological research as well as clinical diagnosis.

Although the quantification of retinal mechanical properties has been demonstrated *in-vivo,* a few challenges remain to be addressed before the technology can be translated. First, a higher

imaging speed is necessary to visualize stiffer posterior layers, such as the sclera. A faster line scan camera can easily address this issue. Second, the propagation distance of the shear wave is limited to a few hundred microns due to the fast attenuation of the signal. A larger field of view can be achieved with a high power excitation pulse, or more ideally, the implementation of an array transducer for a larger region of excitation and detection. Last, it is important to study the changes in the mechanical properties using a diseased model and examine its correlation to clinical impairments.

3.6 Summary

In conclusion, we have demonstrated a method of quantifying the mechanical elasticity of the retinal layers using SW-ARF-OCE based on layer segmentation and shear wave analysis. We have first tested the feasibility on an *ex-vivo* porcine model, where 5 different retinal layers have been isolated and the mechanical elasticity was distinguished. In order to validate the feasibility of translating this technology, imaging was performed on an *in-vivo* retina model, where 3 layers of the retina could be analyzed and quantified for different mechanical properties. This study verifies the feasibility of using this technology for the quantification and diagnosis of retinal diseases. An *in-vivo* elasticity map of the retina has been generated for the first time, to the best of our knowledge. This study is a crucial stepping stone to the translation of the SW-ARF-OCE technology for clinical diagnosis and disease studies.

CHAPTER 4

Quantitative Assessment of Phase Stability

In this chapter, we discuss a method of quantitatively measuring and evaluating the phase stability of swept source lasers. This is necessary in order to verify the phase sensitivity of Doppler imaging methods and provides us with additional parameters to optimize in the system. In section 4.1, we will introduce the biomedical motivation behind the study. The system and experimental setup will be discussed in section 4.2. In section 4.3 we will elaborate on the data collection method and processing algorithm. The experimental results will be presented in section 4.4, where several different lasers from different makers were tested and statistically analyzed to optimize the phase stability in our imaging systems. We will end the chapter with a summary in section 4.5.

4.1 Introduction

Optical coherence tomography (OCT) has been widely adapted in various biomedical applications for its depth resolved imaging capability, high spatial resolution, and potential for endoscopic imaging (104, 108, 109). As a light analogue to ultrasound imaging, OCT reveals the light interference patterns to visualize variations in refractive indices within the biological tissue. In the interference fringe, different frequency components correspond to the back scattering at different axial positions, of which the intensity in the frequency domain corresponds to the tissue structure in a micron scale (104). Furthermore, OCT can achieve sub-nanometer displacement sensitivity by monitoring the inter-fringe phase change of the frequency components and has enabled many applications that aim to visualize microscale tissue dynamics (36, 40, 61, 107).

Since the accuracy of the phase measurement relies on the repeatability of the laser source, broadband lasers have dominated the conventional phase sensitive applications (33, 38).

However, recent studies have demonstrated that swept-source (SS) based OCT may be superior to conventional broadband based ones because it has less fringe washout phenomenon, faster imaging speed, and comparable phase stability (122, 153). For the purpose of stable phase measurement using traditional SS-OCT, it is necessary to maintain consistent timing between laser repetitions (129, 154). Over the past several years, many groups have reported quantification and optimization methods for timing jitters overall or at a single wavelength, but timing jitters within the full bandwidth have not been fully investigated or compared (118, 129). A single wavelength evaluation may be insufficient to represent the stability performance if variations exist across the full bandwidth. In spectrally-encoded SS-OCT applications, where different wavelengths are chromatically dispersed to achieve the fast scan axis, time jitters at each wavelength will have direct effects on the phase measurement. and assessing the timing jitters at individual locations might be insufficient as an integral evaluation (139, 140).

In this study, we report a quantification method to assess the timing jitters within the full bandwidth of a SS-OCT system. To eliminate external perturbations during the assessment, a cover glass was used to generate self-interference fringe of which the phase variations were solely from the light source. A Hilbert transform based method was developed to obtain the time jitters at all the wavelengths. Three different SS lasers were assessed in this study. The results have shown that the wavelength dependent timing inconsistency is not only distinctive between lasers, but also varies within the bandwidth of each laser. This study enables the accurate

assessment of timing jitters at individual wavelengths and may serve as a stepping stone for the noise sourcing and optimizing phase measurement of SS-based spectrally-encoding interferometry.

4.2 System setup and processing algorithm

A swept source based standard OCT system was used for data collection and measurement. Figure 4.1 depicts the experimental setup for measuring the timing inconsistency of a SS laser. The light is delivered through the circulator, collimated by the collimator, and focused on the separated surfaces of a microscope slide. The fiber optic coupler then collects the back-reflected interference pattern from the microscope slide surfaces, which generates a sinusoidal fringe signal. Then, a computer system with a waveform digitizer collects the fringe signal in accordance with the timing signals, i.e., the k-clock and the wavelength (λ) trigger from the SS laser. The λ trigger indicates the time to start acquisition, and every single sample point is timed with the k-clock to form an interference profile as a function of wavenumber. The timings of the k-clock and the λ trigger have been optimized to achieve the best possible timing stability of the laser using the method described in (118). Accordingly, timing inconsistency between repetitions result in sampling at inconsistent wavenumbers.

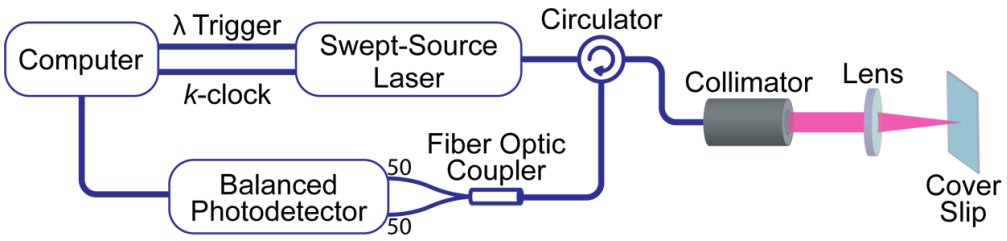

Figure 4.1. System schematic for timing inconsistency quantification. R1, R2: upper and lower surface of the cover plate.

The intensity of the interfere signal is proportional to the cosine of the product of wavenumber, k, and path length difference, z, as shown in Equation 4.1. Since the path length difference remains the same between the two reflective surfaces, the wavenumber variations, Δk, induced by timing jitters will be the sole source of inter-fringe phase variations, $\Delta\varphi$, as shown by Equation 4. 2.

$$I(k) \propto \cos(kz) \quad \text{(Eq. 4.1)}$$

$$\Delta\varphi = \Delta k \times z \quad \text{(Eq. 4.2)}$$

Therefore, we can extract the phase variation and use it to obtain the timing inconsistency. In order to quantitatively assess the timing variation between subsequent laser repetitions, a Hilbert Transform based algorithm, as shown by figure 4.2, is used to achieve the times at which all the wavenumbers are registered.

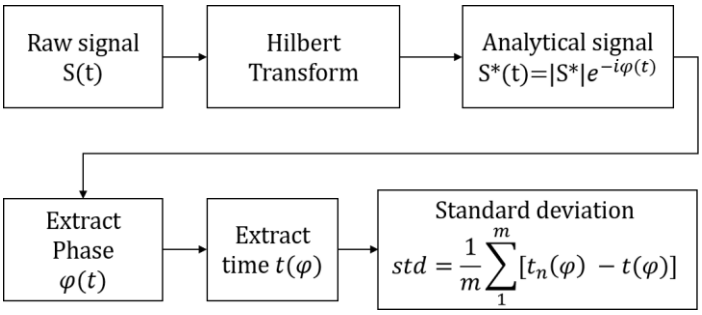

Figure 4.2. Flow chart of timing inconsistency quantification for the full bandwidth. m: number of interferogram within one measurement. (t(φ)): mean time at phase φ over different interferograms.

Figure 4.2 demonstrates the processing algorithm for analyzing the timing consistency at each wavelength. A Hilbert transform extracts the phase profile from a raw interferogram signal, $S(t)$, after which the phase profile was resampled at an equal phase interval to obtain the time, $\varphi(t)$, at

each resampled point. As shown in Equation 4.1, the phase of the fringe increases linearly with wavenumber and, therefore, can be used as an equivalent indicator of the wavenumber. Lastly, the timing inconsistency at the full bandwidth can be determined by calculating the standard deviation of the acquisition time of each wavenumber over subsequent interference fringes.

4.3 Laser testing and statistical analysis

The timing inconsistencies of three SS lasers from different manufacturers were characterized to demonstrate the feasibility of the proposed measurement method. The results are shown in Figure 4.3.

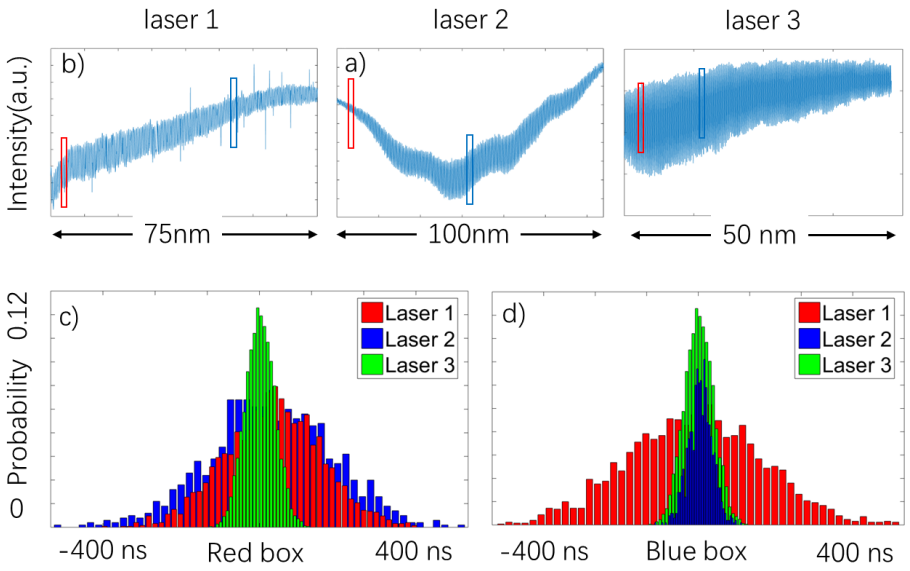

Figure 4.3 Timing consistency at different zero-crossings. (a)(b) Interference fringes of Lasers 1, 2 and 3, respectively. (c)(d) Overlaid histograms showing the centered timing variation at zero-crossings in the red and blue box, respectively. Laser 1 is an all-semiconductor akinetic laser, laser 2 is a vertical cavity surface emitting laser and laser 3 is an Axsun laser.

Figures 4.3 a-c) show the interference fringes of the three lasers obtained using the described method. Based on visual observation, the fringe profile of Laser 2 appears to have more random noise than the others and may be inferred to have a worse timing stability. By collecting the timing information at the two zero-crossings boxed by the red and blue rectangles, timing stabilities at the corresponding locations can be calculated, as shown in Figures 4.3 (c) and (d). Different from our anticipation, the timing stability of Laser 1 in the red box area outperforms that of Laser 2 [Figure 4.3 (c)], but is worse in the blue box [Figure 4.3 (d)]. The laser 3 has relatively good timing stability in both locations. These results indicate that the timing stability of a SS laser is wavenumber-dependent, and full bandwidth quantification is necessary for a comprehensive comparison. To quantitatively evaluate the timing consistency of the full bandwidth, the proposed Hilbert transform based method was performed to generate the profiles shown in Figure 4.4 (a).

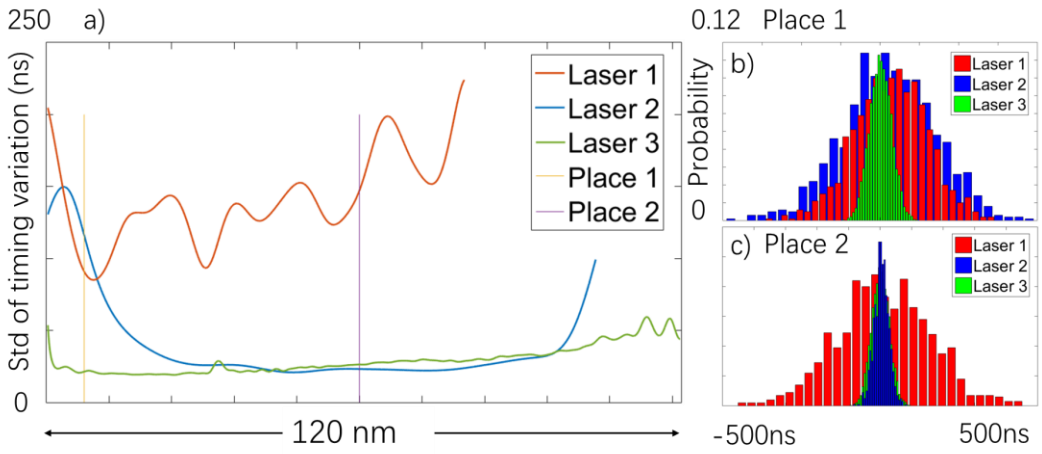

Figure 4.4. Timing consistency of the full bandwidth. (a) Timing consistency profile as a function of wavelength; the y-axis denotes the standard deviation of the timing variation. (b)(c) Histograms showing the timing variations at locations 1 and 2, respectively, in Figure 4.4a.

Figures 4.4 (b) and (c) depict the histograms of timing variations at the two different locations marked in Figure 4.4 (a), which correspond to the red and blue boxes in Figure 4.3. The distributions and the resulting standard deviations are in agreement with the results shown in Figure 4.3, validating the effectiveness of the Hilbert transform based method. As demonstrated in Figure 4.4 (a), Laser 3 seems to have the best phase stability overall, while laser 1 has a comparable timing stability in the middle portion, but the performance at the initial portion of the sweep (i.e., Location 1) is slightly worse than the that of Laser 2 and 3. Laser 2 has a relatively flat power output over different wavelengths, and the average is worse than that of the other two. The peaks in the fluctuating stability profile of Laser 2 is indicating a variant timing clock for different wavelengths shown in Figure 4.3(b). Based on the results, Laser 1 and 3 are more suitable options for phase measurement; specifically, the best phase measurement can be achieved by using the middle portion only.

Using the proposed method, the difference in timing consistency within the full laser bandwidth of two SS lasers from different manufacturers were quantified. The timing stability profiles obtained demonstrate significant different characteristics among the three lasers, as well as variation within the bandwidth of each individual laser. The laser with relatively frequent peak noise appears to have worse overall stability and more fluctuation in the stability profile, whereas the other laser demonstrates a positive correlation between laser power and timing stability.

4.4 Summary

In this study, we have developed a Hilbert transform based quantification method to evaluate the timing stability within the full bandwidth of SS lasers. On the contrary, conventional methods

can only provide a rough estimate of the overall timing stability by evaluating a few points in the interference fringe. Since the accuracy of displacement measurement in SS-OCT is greatly affected by the timing stability, it is of necessity to characterize all the emitting wavelengths quantitatively. The quantification of timing stability profile can provide useful information for SS-OCT applications that require highly accurate phase measurement. Specifically, it can aid the selection of laser for phase sensitive applications and identify the optimal sweep range that yields the highest phase stability. Using this method, we were able to select the most stable swept source laser for cellular activity imaging, superior to broadband lasers, as presented in the next chapter. This method will provide a powerful tool for the development of phase sensitive interferometric system. broadband

CHAPTER 5

Spatial Mapping of Ciliary Activity

In this chapter, we present a spectrally-encoded microscopy system that has been improved and optimized from previous designs in order to detect the activity of ciliary cells in the respiratory and reproductive systems. First we will introduce the significance of such a system as it applies to disease diagnosis and tracking in section 5.1. Then we will go into the details of our system design in section 5.2. In section 5.3, we discuss the Fourier domain analysis method for visualizing and quantifying the spatial ciliary beat frequency, which acts as a measure for the health of ciliary cells. In section 5.4, we present our study of ciliary activity changes that occur with different external stimuli in the respiratory system, such as temperature and drug administration. In section 5.5, we discuss the ciliary function in the female reproductive system and its response to different conditions. Finally we conclude with a summary in section 5.6.

5.1 Introduction:

Ciliary motion in the upper airway is the primary mechanism by which the body transports foreign particulate out of the respiratory system in order to maintain proper respiratory function. Similarly, ciliary cells line the walls of the female fallopian tubes, where they move in a synchronous manner to generate the primary driving force for oviduct tubal transport, which is an essential physiological process for successful pregnancies. Malfunction of the cilium in the fallopian tube may increase the risk of infertility and tubal pregnancy that can result in maternal death. While the physiological function of the cilia differs depending on its location inside the body, in both cases the ciliary beating frequency (CBF) is often disrupted with the onset of disease as well as other conditions, such as changes in temperature or in response to drug

administration. Recent studies show that CBF holds the key to evaluating ciliary health, but current technology is lacking in its detection. While many *ex-vivo* studies have been carried out using bright field microscopy, this technique is not feasible for the *in-vivo* investigation of oviduct ciliary beating frequency.

In order to overcome these limitations and perform *in-vivo* studies, optical coherence tomography (OCT) (98) was recently applied on ciliary motion imaging, taking advantage of its micron scale resolution, real time imaging capability, and potential for endoscopic imaging. Given these powerful features, the study of ciliary functions moves from the dish plate to its natural environment, and demonstrates the feasibility of using OCT to investigate ciliary activity *in-vivo* (93, 99). Specifically, a high resolution OCT endoscope is inserted into either the respiratory or uterus cavity to perform continuous acquisition at one cross sectional site, so that the intensity fluctuations caused by ciliary activity can be visualized over time. Although CBF can be estimated from the variations in OCT intensity, the synchronicity between different cilia cannot be easily investigated to study CBP. Additionally, the limited imaging speed of OCT prevents it from obtaining complex ciliary pattern with a large en-face FOV.

To further expand the effectiveness of using an OCT system in imaging ciliary activity, our group used a phase resolved Doppler optical coherence tomography (PRD-OCT) technique to probe the beating direction and speed of cilia. PRD-OCT is well known for its capability of measuring microscopic particle movement with pico-meter sensitivity (36, 40-42, 100), and is proven to be a powerful tool in visualizing accurate ciliary dynamics by providing not only its transient position but also the relative speed and direction of the ciliary beat (96). Therefore, the beating

phase of different cilia can be simultaneously monitored to study their synchronicity and beating patterns.

In addition, the velocity imaging ability of PRD-OCT also benefits ciliary studies by enhancing the contrast of moving cilia versus other stationery tissue components, and may possibly aid in locating the ciliated area within the entire cavity during *in-vivo* experiments. However, to visualize spatial-temporal cilia activity using OCT requires a two dimensional beam scan (101). Because the rate of the spatial scan must be at least two times greater than the CBF for effective measurements according to the Nyquist theory, there is a limitation on the number of scanning points, which limits the lateral FOV.

A spectrally encoded interferometer (SEI) is capable of lateral 2-D imaging with a single axis beam scan (102, 103), which allows for *en face* imaging at a speed comparable with OCT B-Scans. We report on a swept source spectrally encoded interferometric microscopy (SS-SEIM) system to obtain the enface image of cilia beating frequency and pattern at high speed. Pilot studies have demonstrated Doppler SEI imaging using a broadband laser (155-157), while we have optimized the design by using a high speed swept source laser as the light source. Recent studies have suggested that swept source based low coherence interferometry can provide faster imaging speed, more robustness against fringe washout, comparable sensitivity and resolution when compared to the interferometry based on a broadband laser (119, 121, 158-160). With a swept souce laser of 100kHz, we are able to achieve 100 frames per second (fps) over an enface image area up to 1 mm^2. To achieve similar en-face imaging speed, traditional D-OCT image would require swept source laser with a swept rate over 100 MHz, which is not currently

available. This is the first study to map the spatial-temporal ciliary activity using a SS-SEIM system to the best of our knowledge, and opens up the possibility of investigating spatial ciliary beating frequency and pattern *in-vivo*.

5.2 Spectrally-encoded microscopy system design

The swept source spectrally encoded interferometric microscopy (SS-SEIM) system has been developed using a vertical-cavity surface-emitting laser (VCSEL) based swept source OCT system as shown in figure 5.1.

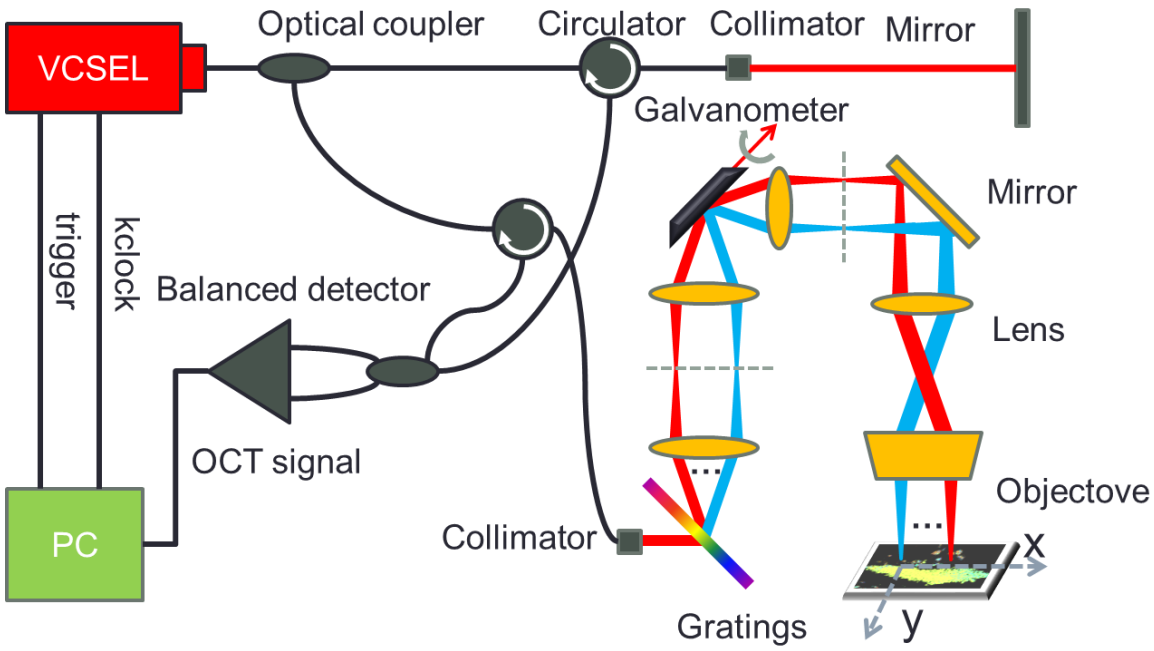

Figure 5.1. System setup for spectrally encoded interferometric microscopy. OC1-OC2: optical coupler, C1-C2: circulator, CO1-CO2: collimator, OA: optical attenuator, M1-M2: mirror, BD: balanced detector, GR: diffraction grating (1145 lines per mm), L1-L4: achromatic lens, L5: 0.4 NA objective lens, G1: galvanometer, FP: focal plane

The center wavelength of the system is 1.3 um, and the A-line rate is 100 kHz. The lateral resolution and displacement sensitivity are measured to be 1.2 um and 0.3 nm, respectively. The sample arm is replaced by a spectrally encoded microscopy setup, which allows for simultaneous sample illumination with a single mode fiber input. The light in the sample arm is first collimated and diffracted by the diffraction gratings, yielding a line pattern as the laser sweeps through its full bandwidth. The 1-D galvanometer mirror G1 scans the wavelength encoded line of light in its perpendicular direction to produce *en face* optical imaging. Two optical relays are employed to center the line of light on to the galvanometer mirror and the back focal point of the objective lens, hence ensuring a flat scanning plane on the sample surface. After, a focused line is illuminated on the sample through the objective, where different wavelengths are focused on different locations of the sample based on their diffraction angles. The collected back scattered light interferes with the reference light to form an interferogram which is detected by a balance detector. The system is capable of real time *en face* displacement imaging at up to 100 fps with 1000 A-lines per image and 2048 pixels per A-line, providing a FOV of approximately 480 x 750 um. The axial displacement sensitivity was measured using the self-interference signal from a 1mm thick microscope slide based on the method described in (127). We have recently evaluated the phase variation of the interference signal and found out that the standard deviation of the phase variation, $\Delta\phi(t)$, is approximately 2 mrad, corresponding to a displacement error of ~0.155nm by using the Doppler equation.

5.3 Fourier domain analysis for spatial ciliary beat frequency

The phase resolved Doppler (PRD) method is able to visualize the ciliary motion by analyzing the interferometric data (96). Specifically, the PRD algorithm defines a linear relationship

between the ciliary displacement, Δd, and the temporal phase change, $\Delta\varphi$, of the interferogram. Equations 5.1 and 5.2 demonstrate the PRD theory to estimate sample displacements within one fast scan using the digitized SEIM signal.

$$\Delta d(x,t) = \frac{\lambda}{4\pi n} * \Delta\varphi(x,t) \quad \text{(Eq. 5.1)}$$

$$\Delta\varphi(x,t) = \varphi(x,t+\Delta t) - \Delta\varphi(x,t) \quad \text{(Eq. 5.2)}$$

Where n denotes the reflective index, λ denotes the wavelength, x denotes the fast axis, and t denotes the time. Since SEIM splits wavelengths in the fast scan axis, λ corresponds to the fast axis, x. In this study, we measure the inter-frame displacement and therefore the frame rate determines the sampling interval, Δt. To fully resolve the periodical activities of the cilia, the system oversamples the ciliated tissue at 100 fps, which allows for frequency measurements of up to 45.5 Hz.

Using the concepts of PRD, the complete processing algorithm follows the flow chart shown in figure 5.2. First, the algorithm utilizes the Hilbert Transform to generate the analytical form of the raw SEIM signal, from which the phase term can be extracted. Second, the PRD algorithm converts the phase value to the displacement information using equation 5.1. By performing these two steps on every spatial position, algorithm can eventually map out the *en face* displacement images over time.

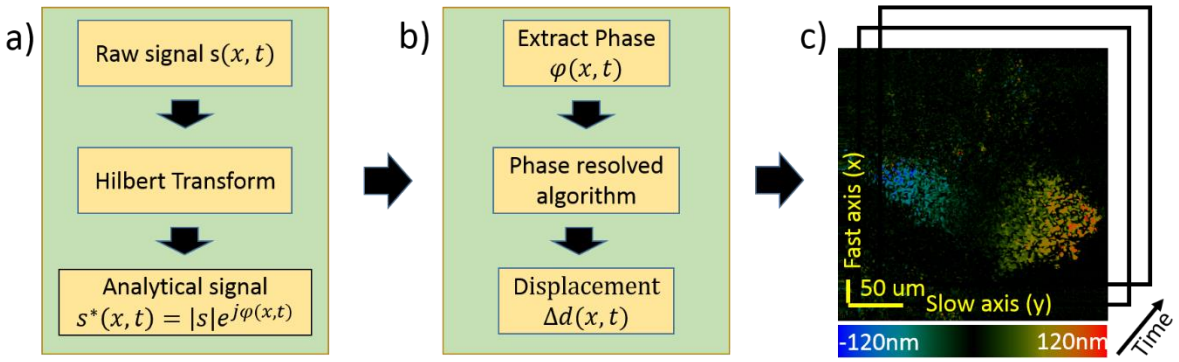

Figure 5.2 Processing algorithm for SEIM system. a) Conversion of the raw signal to its analytical form using the Hilbert Transform. b) Extraction of the phase term and calculation of the displacement using the phase resolved Doppler algorithm. c) *En face* displacement images of a ciliated area over time.

Using a Cooley-Tukey and Bluestein fast Fourier Transform (FFT) to implement the Hilbert transform, the total time complexity to obtain an *en face* displacement map is $O(MN \log_2 N)$, where M is the number of A-lines per image and N is the number of points per A-line. One method to increase the processing speed is to parallelize the algorithm, which can reduce the run time by a factor of MN in theory. First, the parallelized algorithm processes all of the A-lines simultaneously, accelerating by a factor of M. Second, it is possible to break down most steps of each A-line processing into N parallelizable sub-problems, so that the resulting total reduction in run time will be approximately MN. In this study, we utilized two GPU's (graphic processing unit) to parallelize the algorithm and achieved real time displacement imaging of up to 100 fps with 1000 x 2048 pixels.

The *en face* displacement images enable analysis on both the ciliary beat pattern and the CBF. The spatial and temporal pattern can be visualized directly from the temporal *en face* (figure

5.3a) and M-mode images (figure 5.3b). Figure 5.3c shows the displacement at a single ciliated site, and figure 5.3d is the corresponding Fourier domain analysis showing the CBF at the peak of the plot. By performing the Fourier domain analysis over the entire field of view, the spatial CBF can be visualized as demonstrated by figure 5.3e. Additionally, the histogram analysis in figure 5.3f can help visualize the mean and standard deviation of the spatial CBF image.

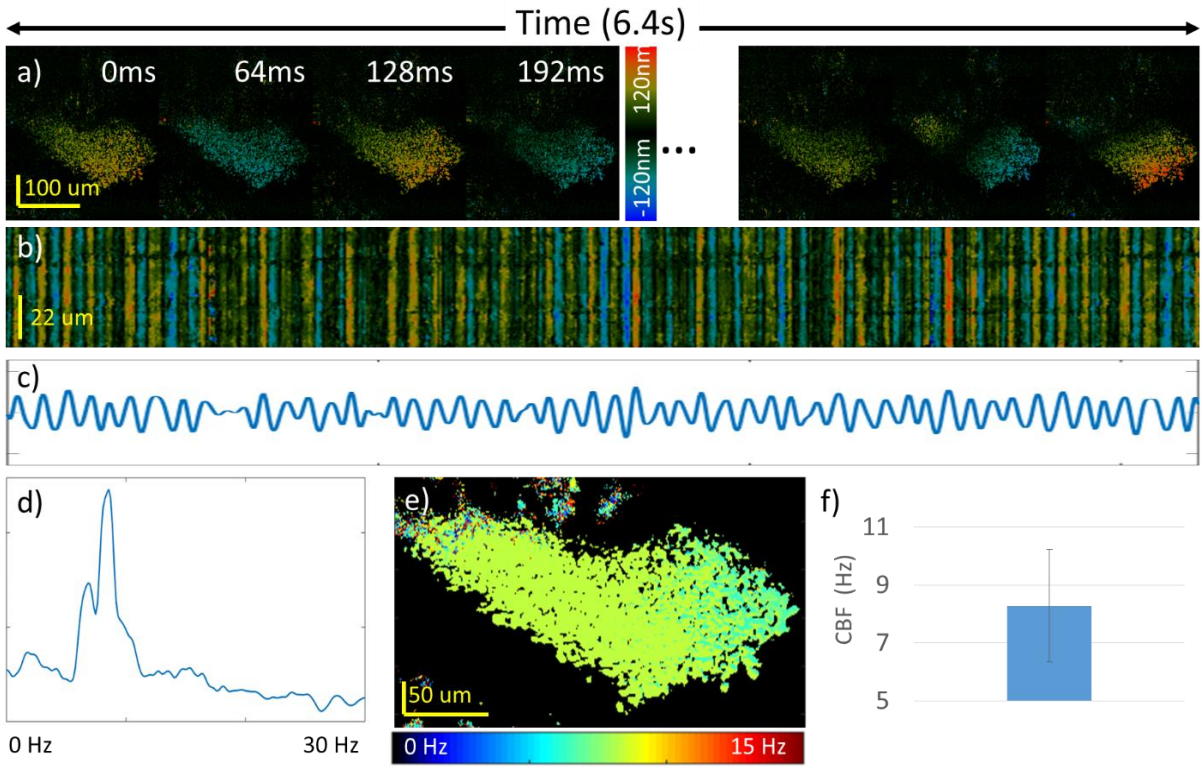

Figure 5.3 Analysis method for spatial ciliary activity. a) Temporal displacement images showing periodical ciliary activity. b) M-mode displacement of a single fast scan. c) Quantitative displacement at a single location. d) Spectrum of the displacement showing the ciliary beat frequency (CBF) at its peak. e) Spatial mapping of CBF. f) Histogram of the CBF.

For this initial feasibility study, variations in the CBF were observed within a spatial region. While some differences in CBF are expected across a sample, it would be worthwhile to more closely analyze the origin of these variations to better understand ciliary motion. It was also obvious that some cilia were beginning to degrade and were no longer moving in a synchronized manner with each other. These randomly moving cilia contributed to noise within the sample and the measured CBF. Future *in-vivo* studies can help better explain the loss of synchronicity and spatial changes in CBF by eliminating the tissue degradation and freshness factors.

The two primary challenges of translating this technology to *in-vivo* studies are the noise factor and the clinical adaptability of the scanner. Bulk motion from breathing is expected to have a large impact on the data. However, since noise from breathing is largely characterized by a low frequency bulk movement, frequency analysis can be utilized to eliminate these factors. The current system sample arm and scanner unit is bulky and unsuitable for *in-vivo* studies. However, a handheld probe based design is currently under fabrication to ensure clinical adaptability in the next study.

5.4 Ciliary activity in the respiratory system

Rabbit tracheal samples were harvested from freshly euthanized male New Zealand white rabbits under the approval of the Animal Care and Use Committee (IACUC) at UC Irvine. The tissues were immediately submerged in Hanks Balanced Salt Solution (HBSS) and kept at room temperature of approximately 23 °C. Soft tissue was carefully dissected from the outer surface of the trachea to ensure an even surface for imaging. The tissue was cut along the long axis of the trachea to reveal the mucosal surface for imaging, and then secured down with pins onto a

silicone-lined petri dish. A layer of HBSS was added to the dish to mimic the natural tissue environment and minimize disruption of ciliary motion. Finally the sample was moved to the imaging stage where it was placed on a temperature-controlled hot plate for temperature regulation during imaging as shown in the figure 5.4.

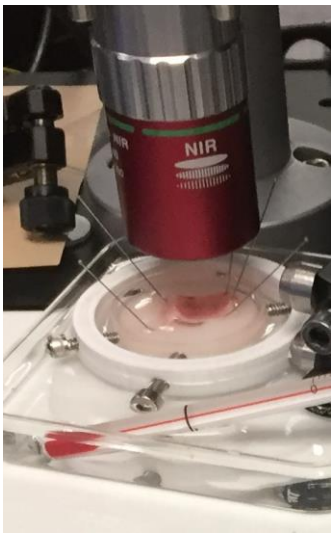

Figure 5.4. Photograph of ex vivo imaging setup.

During imaging, the line scan was made to focus on the cilia layer on the top surface of the trachea sample. In addition to synchronized ciliary motion, some random ciliary movements were also observed at certain parts of the sample. For the purpose of measuring the CBF, we focus on the regions with synchronized motion. The ciliary motion is visualized in real-time and the region of interest can be identified and imaged efficiently.

The tracheal sample was acquired as described in the methods section and a region with synchronized ciliary motion was identified. SEIM Enface imaging was done while increasing the temperature of the sample from room temperature to 33 °C. The raw line-scan Doppler SEIM

images are shown in figure 5.5a-c, where the same area of interest is imaged at 27 °C, 30 °C, and 33°C, respectively. Different colors correspond to the change in the phase amplitude and the direction of the ciliary motion, which is directly proportional to the velocity of the motion. For different temperatures, the time at which the cilia complete a single power stroke cycle can be distinguished. The duration of the phase cycle can be estimated to be approximately 0.132 s for 27°C, 0.11 s for 30 °C, and 0.088 s for 33 °C. These results show that the CBF increases with temperature as expected from previous literature (96).

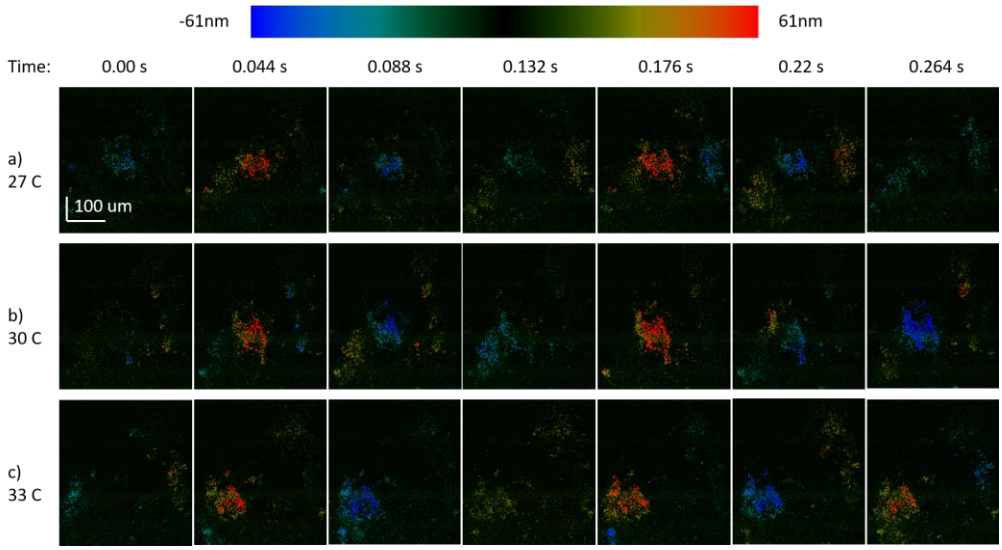

Figure 5.5. Cilia motion at different temperature. a) Synchronized cilia cycle from 0 to 0.2 s at 27 °C, b) at 30 °C, c) at 33 °C.

Since the spatially encoded data is continuously collected over 6 seconds, the temporal data can also be extracted. The temporal profile or M-mode at each spatial location can be measured along the depth direction. It is important to note that the line scan system has advantages in visualizing lateral spatial and temporal information, but sacrifices depth information and can only image superficial structures. However, for thin samples like cilia, tens of microns in depth

are more than sufficient. An example of the temporal profile at one line under the 3 temperature conditions is presented in figures 5.6a-c. The phase is averaged across the entire depth of view and drawn out in figures 5.6d-f. Although the phase amplitude varies depending on the angular fluctuations of the sample and noise, the CBF is mostly consistent. In order to quantitatively determine the CBF at that particular location, a FFT is performed on the phase plot to yield the frequency plots in figures 5.6g-i. The peak frequency occurs at 9 Hz, 12 Hz, and 13 Hz for the 27 °C, 30 °C, and 33 °C cilia samples respectively.

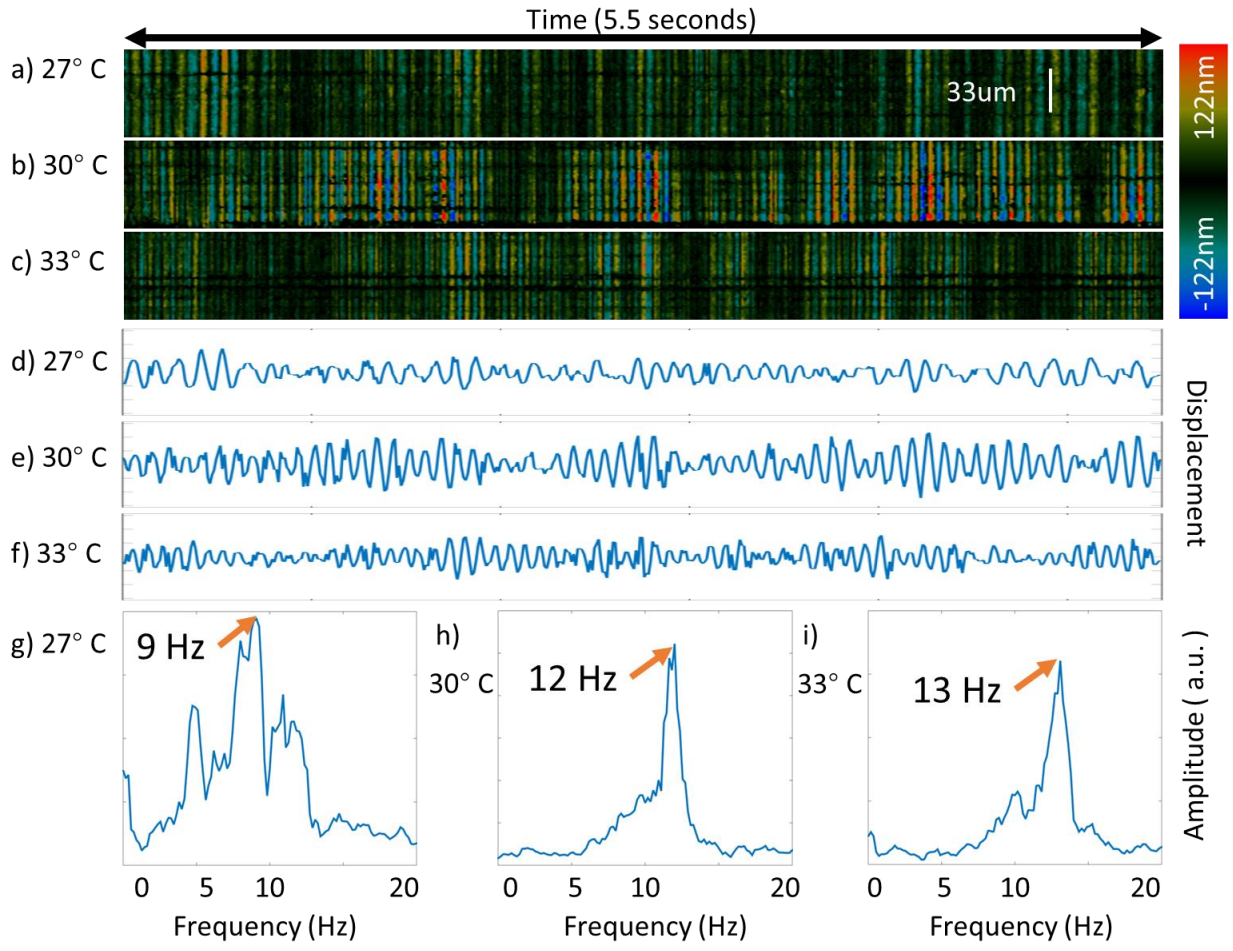

Figure 5.6. Analysis on the airway ciliary movement at a single location. a-c) raw phase data over depth, d-f) mean phase plot of raw data, g-i) Frequency distribution after FFT.

With the same data processing method, the temporal data is analyzed at each spatial location to yield the spatially coded CBF maps as shown in figures 5.7a-c for the three temperatures respectively. The same region was imaged for all three conditions, where there appeared to be 2 separate bodies of synchronized cilia, marked by the yellow and red boxes. Small changes in the CBF can be observed between the two spatial regions at each temperature. With the increase in temperature, the CBF of all cilia increased as expected, and the means and standard deviations of both regions at each temperature have been plotted in figure 5.7d. The mean values ranged between 7.4 Hz and 13 Hz, all reasonable values for mammalian CBF. A general upward trend can be concluded between the CBF and the temperature.

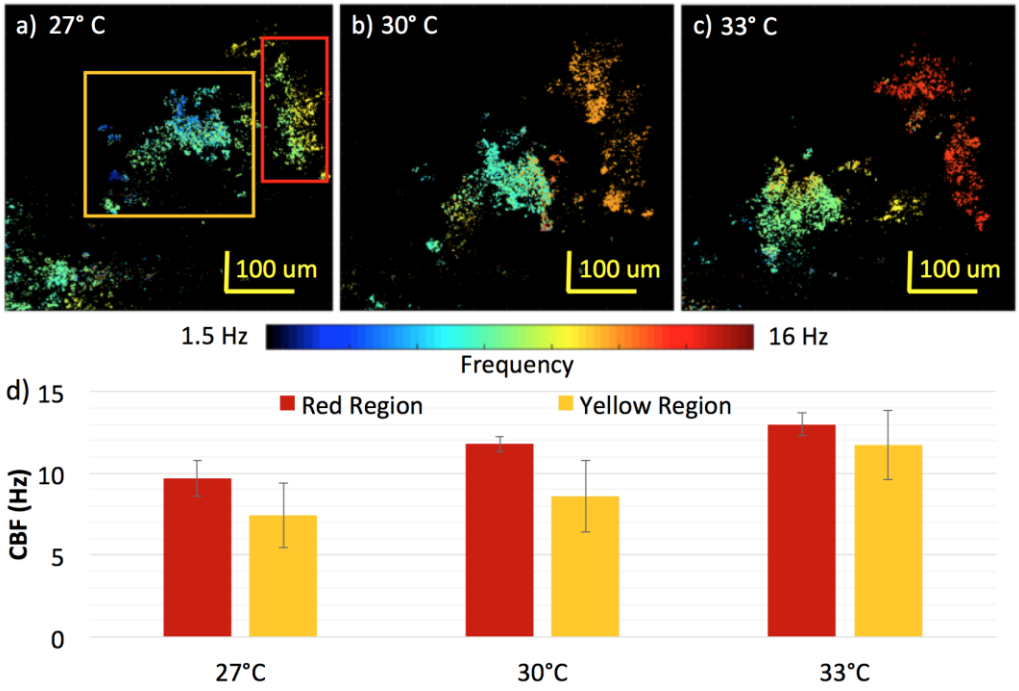

Figure 5.7 Spatial distribution of CBF with changes in temperature. a) at 27 °C, b) at 30 °C, c) at 33 °C with the same corresponding region, d) CBF analysis of yellow and red regions.

For the next experiment, the effects of lidocaine administration were studied. In general, lidocaine is a local anesthetic that is expected to significantly slow down ciliary motion and mucus transport. For this experiment, all samples were kept at 27 °C. A solution of 2% lidocaine was applied to the sample and imaging took place after 5 minutes. The raw enface images for the baseline measurement and after lidocaine application are shown in figures 5.8a and 5.8b, respectively. While the baseline cilia completed a full power stroke cycle in approximately 0.14 s, the lidocaine-treated cilia is not even halfway through the cycle in the same amount of time. Again, the temporal or M-mode data is plotted at every spatial location, yielding in the examples shown in figure 5.8c and 5.8d for the baseline and lidocaine-treated cilia, respectively. From the temporal data, it is evident that the frequency decreased significantly after lidocaine administration. The displacement plot was generated using the average phase over the entire depth and FFT was performed to calculate the frequency peak at each location. Finally, the spatial map can be visualized in figures 5.8e and 5.8f, which are before and after drug administration respectively. The mean and standard deviation for the baseline and treatment data were calculated using the CBF from each spatial location where cilia is present, and plotted in figure 5.8g. The mean CBF before treatment was 7.2 Hz and decreased to 2.7 Hz after treatment. As shown in the spatial map, many of the cilia stopped moving altogether after lidocaine was applied, while others merely slowed down. Only the active cilia were taken into account when calculating the mean CBF and standard deviation.

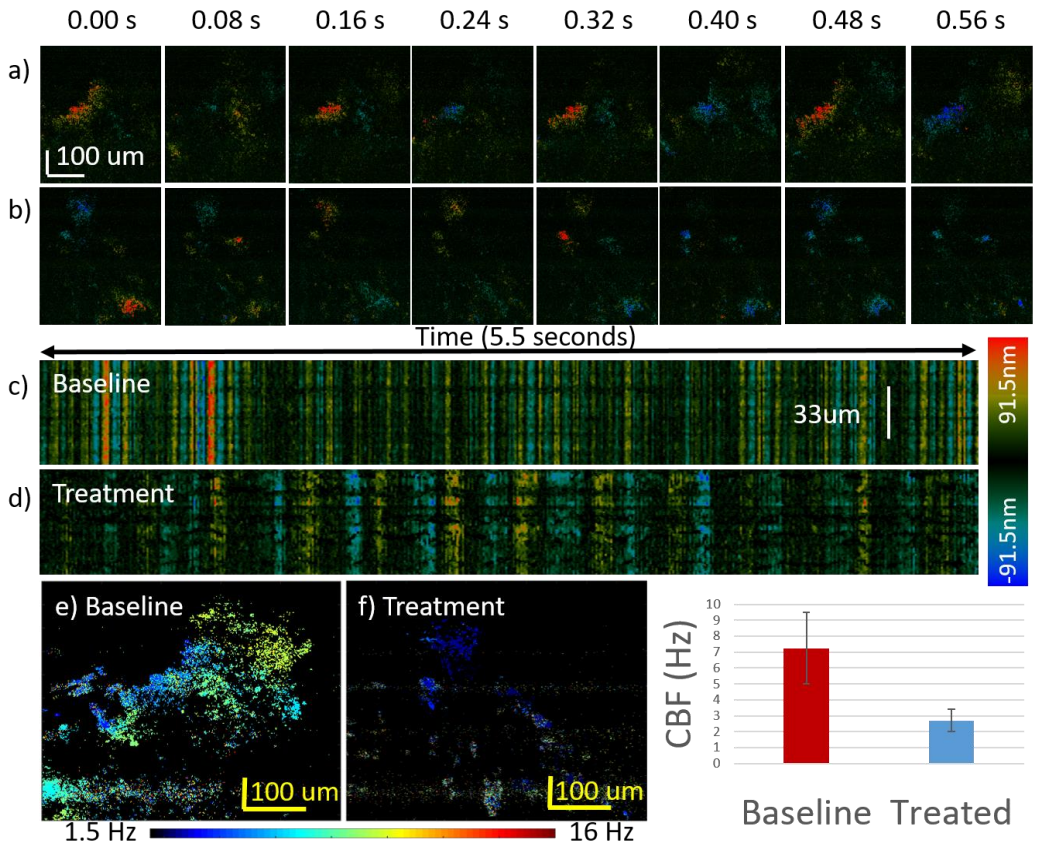

Figure 5.8. Effect of 2% lidocaine treatment on CBF. a) Synchronized cilia cycle from 0 to 0.2 s for baseline sample at 23 C. b) Synchronized cilia cycle from 0 to 0.2 s for treatment sample at 23 C. c) Raw phase data of baseline data. b) Raw phase data after treatment. Note that most of the cilia were no longer active after treatment, and a small region of active cilia was used for analysis. e) Spatial distribution of CBF for baseline sample. f) Spatial distribution of CBF for treatment sample. g) CBF analysis of entire region.

Ciliary activity in response to albuterol, which is commonly used to increase respiratory function, was also investigated to further verify the system effectiveness. According to previous reports about the effects of albuterol on ciliary tissue (96, 161-163), CBF is expected to increase with the introduction of the drug. Similar to the lidocaine experiment, a rabbit trachea sample is

kept at room temperature and the baseline data is first recorded when the sample is placed in HBSS buffer only. Then the buffer is replaced with a 0.3% albuterol solution as mentioned in the methods section, and imaging was performed after approximately 1 minute. As shown in figure 5.9, the spatial CBF for the experimental group increased across the region of interest from a baseline of 5.64 Hz to 6.13 Hz.

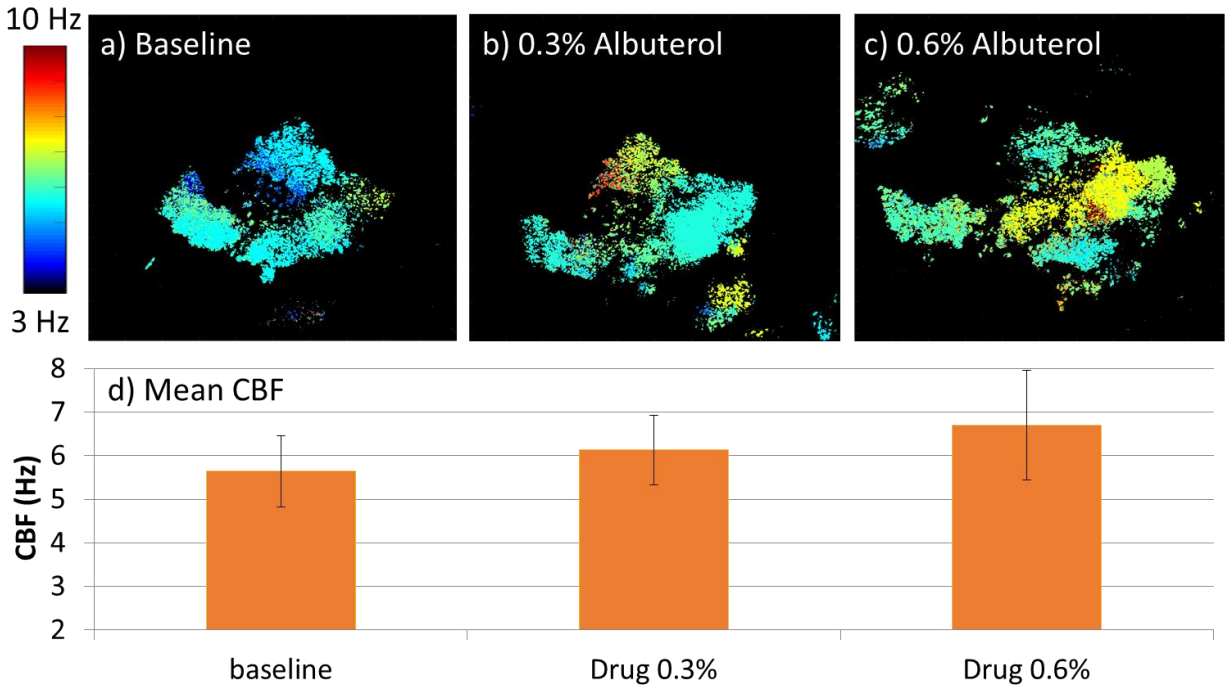

Figure 5.9. Effect of albuterol treatment on CBF. a) Spatial distribution of CBF for baseline. b) Spatial distribution of CBF for sample treated with 0.3% albuterol. c) Spatial distribution of CBF for sample treated with 0.6% albuterol. d) CBF analysis of entire region.

We then added more albuterol to the buffer to achieve a 0.6% drug concentration. As expected, the overall CBF increased again to 6.7 Hz. In addition, more regions of ciliated cells are

activated and contribute to a more synchronized ciliary activity within the same imaging area. The mean and standard deviation values are calculated and plotted in figure 5.9d.

5.5 Ciliary activity in the reproductive system

In order to visualize and register the spatial and temporal ciliary movement, *en face* images have been taken continuously at the surface of the ciliated layer. By integrating the PRD algorithm, the system can provide high contrast between actively moving cilia and the static background. The GPU accelerated imaging program further enables instant feedback (detection of active cilia), which allows for real time positioning and alignment over the entire surface of the sample. During the imaging, we have observed both synchronized and unsynchronized ciliary motion. For studying the spatial CBF, we focus the study only on the areas with synchronized ciliary activity.

To understand the influence of temperature on the oviduct cilia, we have performed SEIM imaging on the oviduct sample with varying temperature conditions at 23 °C, 26 °C, 29 °C, and 32°C, respectively. The preparation of the sample follows the procedure as described in the methods section and *en face* displacement images was taken at a region of synchronized ciliary activity for a period of 6.4 s. Figure 5.10 shows the time-series displacement images at the same region under different temperature conditions, and the colors correspond to the amplitude and direction of the displacement, where black represents minimal displacement while red and blue show opposite displacement directions. The images visualize a full cycle of the synchronized motion from a cluster of active cilia, and the time to complete a power stroke seems to decrease with increasing temperatures.

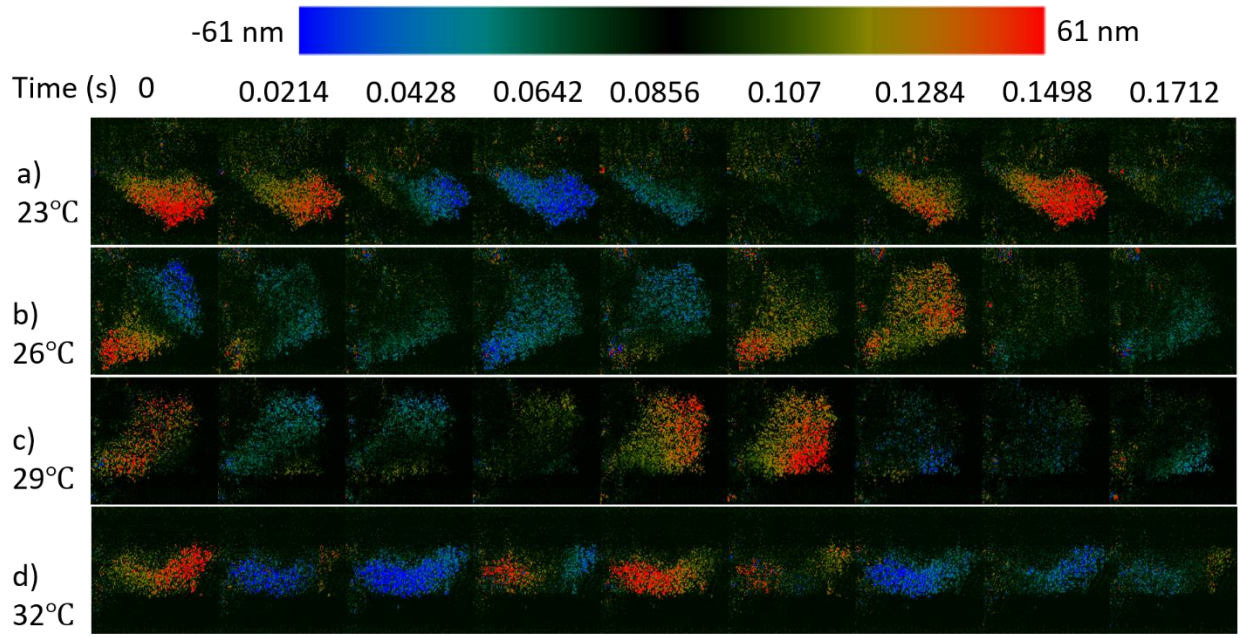

Figure 5.10. Periodical oviduct ciliary activity at different temperature. a-d) Coordinated ciliary beating cycle from 0 to 0.17 s at 23 °C, 26 °C, 29 °C, and 33 °C respectively.

Based on the sampling theory, the resolution of the frequency is proportional to the reciprocal of the sampling time. In order to accurately measure the CBF and differentiate the subtle CBF changes over temperature, the *en face* images were continuously acquired at 94 Hz for 6.4 second, providing a frequency resolution of approximately 0.1 Hz. The M-mode images clearly visualize the complete ciliary beating cycle, demonstrating the sufficiency of the sampling rate. The temporal profile in figure 5.11a is generated by vertically averaging all the M-mode images. Although the magnitude of the ciliary beats fluctuates in the temporal profile, the duration of each cycle seems to be consistent at each temperature. Therefore, it is feasible to use the Fourier transform to analyze the beating frequency. The Fourier transform was then performed on the temporal profile, and the CBF can be identified by the peak. The value of the CBF has been calculated to range from 12Hz to 15Hz with increasing temperatures.

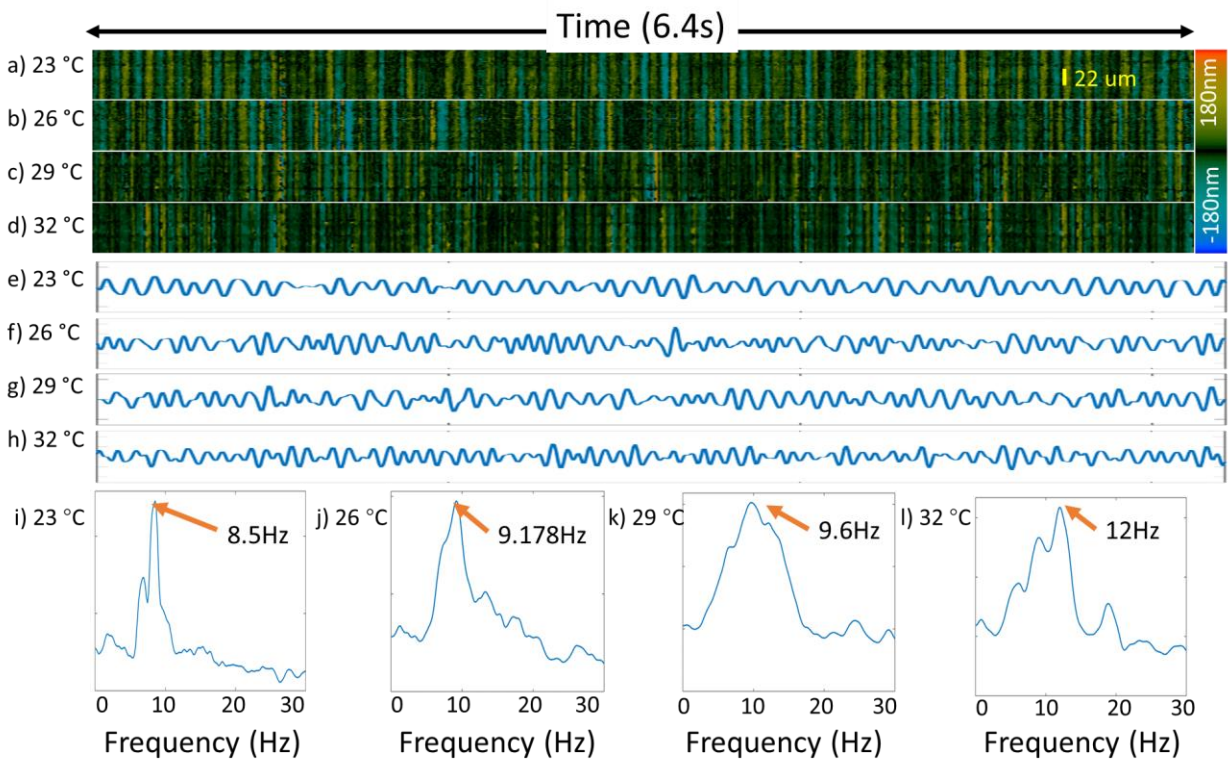

Figure 5.11 Analysis on the oviduct ciliary movement at a single location. a-d) Temporal displacement for an A-line within the ciliated area, e-h) Temporal displacement at the corresponding site, i-l) Spectrum after FFT, where the peak frequency corresponds to the CBF.

By performing the frequency analysis on all of the locations within the ROI, the spatial CBF can be mapped out as shown by figure 5.12a. The color bar on the top corresponds to different CBF. At each temperature, it is obvious that the CBF is mostly uniform within the patch of cilia, indicating synchronized ciliary beats. The region showing a large variance of CBF likely corresponds to asynchronized ciliary motion, which is expected to have varying frequencies. When increasing from 23 °C in figure 5.12a to 26 °C in 5.12b, it seems that the higher temperature played a role in activating more synchronized ciliary cells. Lastly, significant increases in the CBF can be observed from the spatial maps when increasing the temperature

from 23 °C to 33 °C. Figure 5.12e summarizes the mean values of the CBF, and although there are some deviations within each group, the overall trend is consistent. The histogram analysis was performed only in the area with synchronized ciliary motion. We conclude that the temperature has a positive impact on ciliary activity.

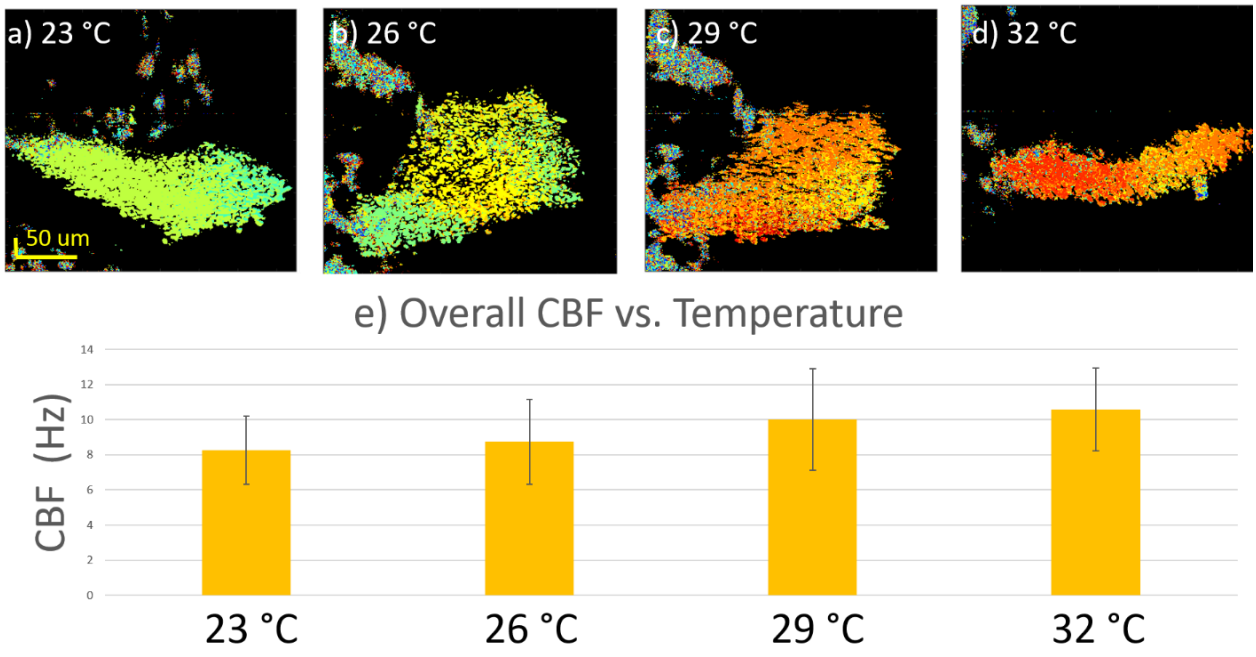

Figure 5.12 Spatial oviduct CBF at different temperature. a-d) Spatial distribution of the CBF at 23 °C, 26 °C, 29 °C, and 33 °C respectively. e) Histogram of the CBF at different temperatures.

According to previous studies, lidocaine is an anesthetic that can depress the ciliary activity in the respiratory tract. Recent studies indicate that it is able to reduce the CBF, and further de-ciliated the epithelium. Since the structure of the oviduct cilia is essentially identical to that of the respiratory cilia, lidocaine is expected to have a similar effect. The lidocaine experiment follows the procedure as describes in the method section, where 2% lidocaine was applied to the sample at room temperature. SEIM images were acquired at a same patch of cilia for a duration

of 6.4 s before and after the lidocaine administration. By performing the Fourier domain analysis on the entire ROI, the spatial CBF maps can be generated as shown by figures 5.13a-b. Figures 5.13a and 5.13b show the spatial CBF distributions at baseline and after lidocaine administration respectively. Lidocaine application decreases the overall CBF. Additionally, the area of active cilia also decreases after lidocaine application, indicating deactivation of the ciliary cells. The results can be summarized in figure 5.13c, which confirms the negative influence of lidocaine on ciliary activity and the feasibility of the SEIM system in detecting changes in the CBF.

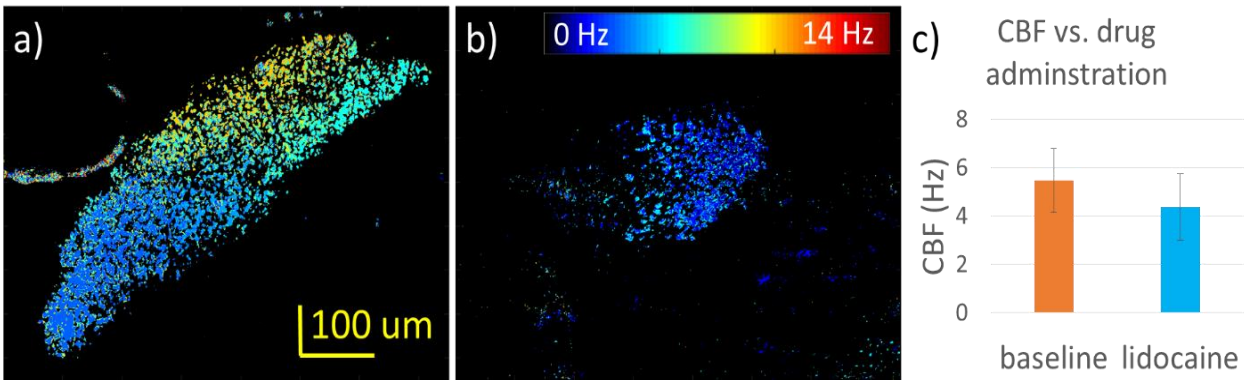

Figure 5.13 Effect of 2% lidocaine administration on the Oviduct CBF. a-b) Spatial CBF maps before and after lidocaine administration. c) Histogram showing the mean and standard deviation of the CBF for the control and experimental conditions.

One major challenge for the clinical translation of this technology is the reduction of bulk motion during the imaging. Because the PRD method is sensitive to bulk motion, it may result in unexpected noise for the CBF measurements. One way to reduce the bulk motion is to mechanically stabilize the imaging probe using an inflatable balloon. However, contact between the balloon and tissue may affect the ciliary activity and introduce error. Since the PRD method measures the sample displacement relative to the reference reflector, we can eliminate the bulk

motion in the measurement by compensating the bulk motion dynamically. In particular, we can measure the bulk motion from a non-ciliated region and use it as the reference to eliminate the bulk motion

5.6 Summary

We have demonstrated a novel method of spatially mapping the CBF and ciliary motion with high speed, high resolution Doppler SEIM. With this line-scan system, we are able to acquire real-time *en face* images of the cilia and analyze the synchronicity of the motion in the trachea and the oviduct. The feasibility of the technique has been verified through the experiments with varying temperatures and drug administration. A general trend was observed between increases in the external temperature and increases in the CBF. In addition, the CBF decreased significantly after application of lidocaine and an increasing trend was observed with the introduction of albuterol. Compared to existing technology, the SEIM system provides a more suitable FOV and the potential for ciliary endoscopy inside the respiratory system and the fallopian tube. Although bulk motion may be an obstacle for future *in-vivo* studies, it can be resolved by a feedback-controlled reference arm or a mechanical stabilizer. This study will serve as a stepping stone toward the clinical translation of the PRD-SS-SEIM technique to aid in the study of CBF as pertaining to the airway and reproductive system.

CHAPTER 8

Summary and Future Directions

8.1 Current study and limitation

This Ph.D. dissertation presented two imaging systems based on the principles of phase-resolved Doppler OCT that cater to unmet needs in the biomedical imaging field. Using the displacement information that was extracted from PRD-OCT, the elasticity of the posterior eye was detected and quantified in both ex vivo and in vivo animal models. PRD-OCT also provides motion detection algorithms that were able to detect the ciliary activity in both the respiratory and reproductive systems.

A method of confocal shear wave OCE imaging was developed to address the early detection of mechanical changes inside the eye globe. With the novel confocal set up, it was possible to minimize the exposure of the ultrasound force to the sensitive retinal layers, while at the same time provide the highly sensitive phase and displacement information required to calculate the elasticity. This was a significant improvement over previous elastography systems, especially in the capability of directly calculating the quantitative Young's modulus of the posterior eye tissue rather than relative values. The ARF-OCE technique developed allows us to image and characterize the biomechanical properties of posterior eye noninvasively. Current limitation of the technique was that the imaging speed of the acquisition camera was too slow to capture the stiffer layers of the retina. In order to provide faster phase imaging, it was necessary to step away from broadband lasers and focus on swept source lasers that were much faster.

In the transition away from broadband lasers, a major hurdle lied in the phase instability of swept source lasers. To address this concern, we developed a method of measuring the phase stability using a simple algorithm to detect the phase jittering of the system. With this technique, we measured two different swept source lasers that were readily available, and concluded that swept source lasers have improved much over the years and may even be superior to broadband lasers in terms of phase stability. With that knowledge, we moved to a swept source based phase resolved imaging system.

The SS-SEIM system was developed and achieved the goal of high resolution en face imaging to meet the needs of ciliary activity tracking. This technology provided high resolution on par with microscopy techniques and also high speed with a line scan sweeping method. We were able to spatially visualize the ciliary beating and their changes over different experimental conditions, matching the expected results as presented in previous literature. We demonstrated the feasibility of the SS-SEIM system in imaging the ciliary health in both the respiratory system and the female reproductive system. However, the current system configuration is somewhat bulky for *in-vivo* study, and requires a floating table to eliminate the bulk motion in the sample which is infeasible for live animals due to their voluntary movement. It is thereby necessary to incorporate the SS-SEIM system in an endoscope design and develop a method to automatically cancel the bulk motion during investigations on live beings.

As a part of this dissertation, both the confocal shear wave ARF-OCE system and the SS-SEIM system underwent development and feasibility studies. With the success of these studies, several

potential projects stemmed and are currently expanding. We will cover a few of these ideas in the next sections.

8.2 Future directions: Spectrally encoded endoscopy

The ultimate goal of SS-SEIM is to perform in vivo diagnosis and tracking of disease. As briefly discussed earlier, the current microscopy setup is much too bulky and cannot be easily adapted for in vivo tissue imaging. As the next step, we proposed a SEIM rigid hand-held probe for *in-vivo* imaging of ciliary activity inside the nasal cavity as shown below, as well as 2 methods of bulk motion removal as discussed below.

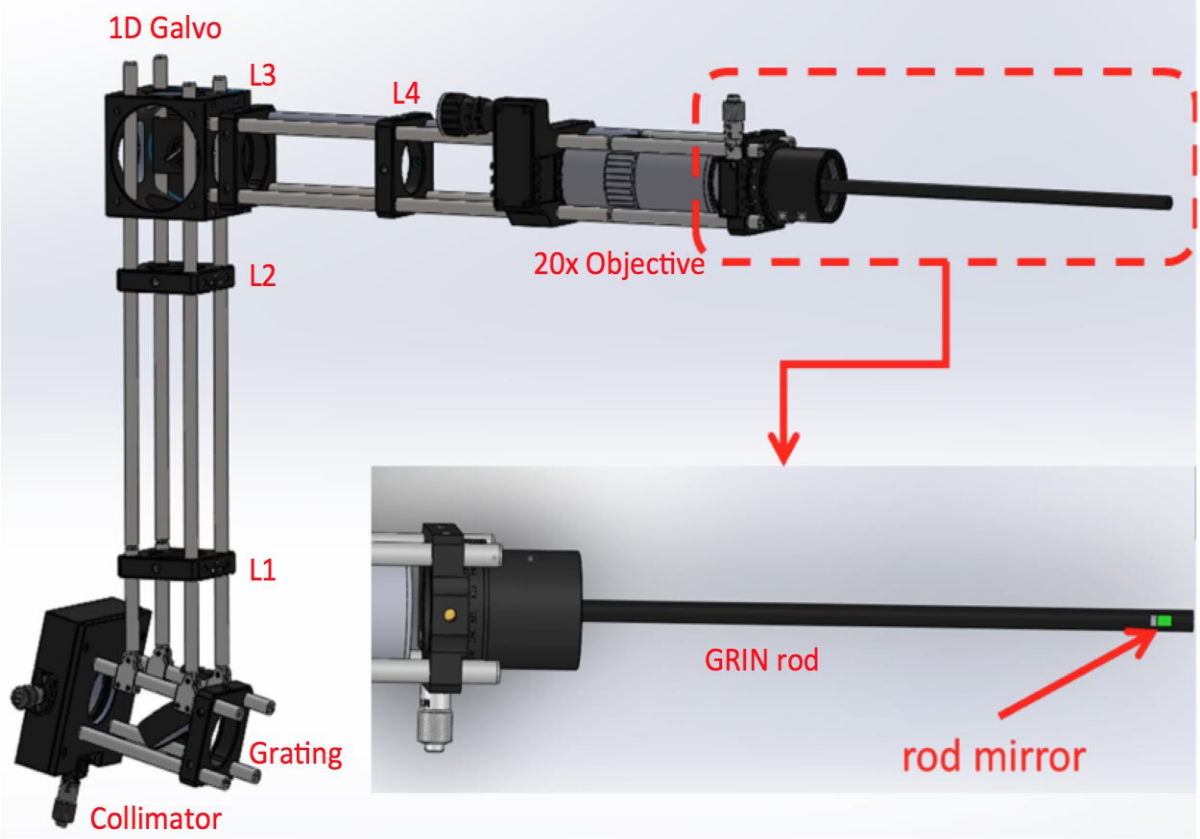

Figure 6.1 Rigid handheld SEIM Probe

Figure 6.1 demonstrates the design of the rigid handheld probe for SEIM imaging. The gratings deflects and scans the collimated light along the fast axis, and the galvanometer mirror acts as the slow scan driver. Two pair of lens L1-L2 and L3-L4 centers the light on the galvanometer mirror and the back focus of the high NA objective, ensuring flat optical illumination on the sample. The GRIN rod relays the optical illumination to the distal end, allows for nasal cavity imaging with high NA illumination. A rod mirror will be mount on the distal end to perform side view imaging. A rotational mount, together with a metal tube will hold the GRIN rod and rod mirror assembly and control the region of interest. The rigid tube was chosen for this application since it allows for more stable imaging than a flexible probe (99) and thereby minimize the bulk motion that may overwhelm the ciliary motion. Other features that may be implemented on the endoscope are a position guiding system on the hand-held probe, a confocal endoscopic camera, and a stabilization system.

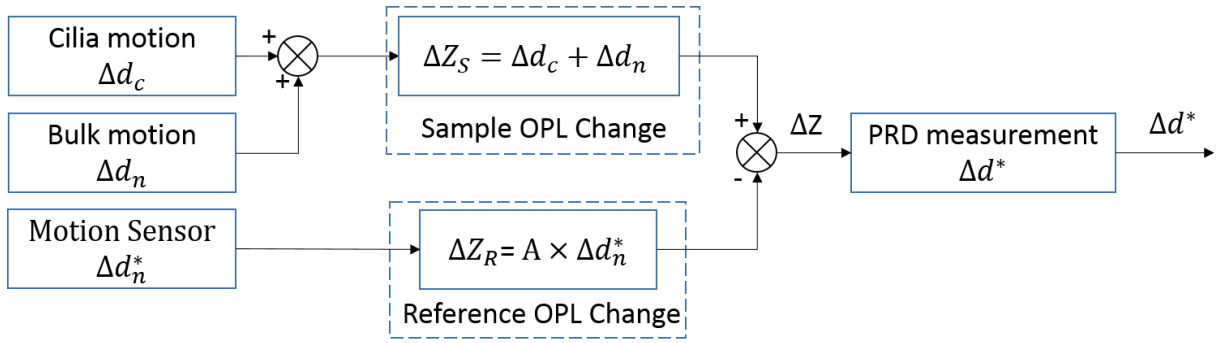

Figure 6.2 Open loop control system. ΔZ_R, ΔZ_s: optical path length change in reference and sample back scattering light respectively, Δd_c, Δd_n: ciliary motion and bulk motion respectively, $\Delta d^*{}_n$: sample motion detected by a motion sensor, Δd^*: sample motion detected by PRD measurement, A: arbitrary constant.

With a handheld portable probe, the bulk motion is expected to increase and create possible issues with data acquisition. Since both ciliary motion Δd_c and bulk motion Δd_n can contribute changes to the optical path length (OPL) Z_S, it is necessary to eliminate the influence of bulk motion in order to obtain PRD measurement on ciliary motion only. To cancel the bulk motion induced OPL change, we can change the OPL of reference arm ΔZ_R along with the bulk motion, so that the total OPL change will only depend on ciliary motion. An open loop control system requires an extra motion sensor to measure the bulk motion Δd_n^* and an actuator to change the reference arm OPL accordingly.

We can further utilize the PRD measurement as the feedback to cancel the bulk motion using a closed loop configuration, which cancels the OPL change induced by the bulk movement. It is possible to extract the bulk motion from the PRD measurement because its characteristics are highly different from ciliary motion in term of intensity, frequency, and spatial distribution. Thereby, the control system can use the extracted bulk motion Δd_n^* to control the reference OPL change so as to minimize the bulk motion induced OPL change. Prior study integrated a balloon stabilizer on the endoscope to ensure stable measurement (99). However, the contact between infiltrated balloon and ciliated tissue may affect the ciliary activity and pose a negative impact on the effective of measurement. Plus, the balloon-based solution may increase the overall screening time in the way that images cannot be taken before the balloon is fully infiltrated. Herein, the OPL control system does not need mechanical stabilizer, so that allows for noncontact real time ciliary imaging.

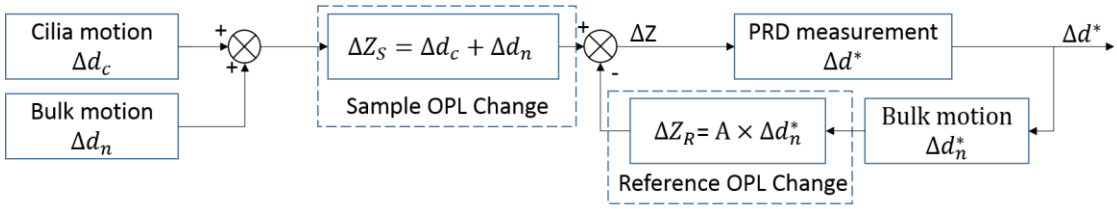

Figure 6.3 Closed-Loop control system. ΔZ_R, ΔZ_s: optical path length change in reference and sample back scattering light respectively, Δd_c, Δd_n: ciliary motion and bulk motion respectively, Δd^*: sample motion detected by PRD measurement, A: arbitrary constant.

8.3 Future directions: Optical nerve head OCE

Our group first demonstrated the feasibility of using confocal shear wave ARF-OCE to map out the mechanical properties of the central retina in excised and *in-vivo* animal tissues. In the next step, we propose to look at the mechanical elasticity of the optic nerve head (ONH) region on the posterior eye, and how it changes during the onset and progression of glaucoma. Several challenges were presented due to the high stiffness of the optic nerve region, the off-center location of the ONH on the posterior eye, and the distortion of the acoustic and optical beams caused by the unique structures of the angled anterior eye. The speed of the shear wave propagation increases with the stiffness, and our OCE system limitation lies in the detection speed of 50 k A-lines per second. In order to capture the high speed propagation, we increased our detection range to 2 mm. The distortion of the ARF-OCE beams were corrected by re-aligning the ultrasound and OCT beams for individual samples while avoiding certain less transparent structures in the anterior eye such as the iris.

Experiments were performed on freshly excised New Zealand White rabbit eyes within 1 hour of death. The anterior portion was kept intact to preserve the structure and intraocular pressure of

the eye. The optic nerve was clipped approximately 3 mm away from the eye globe in order to avoid mechanical damage to the sample. The eye globe was placed in a silicon holder with the optic nerve in direct view, submerged in PBS, and secured onto the imaging stage. The structural OCT image of the entire optic nerve is shown in figure 6.4a, where the dip represents the nerve fiber region. The red box is magnified and shown in figure 6.4b, where the dotted line serves as an approximately boundary between the peripheral retina and the optic nerve head. The shear wave is applied at the dotted line and propagates to the left (peripheral retina) and right (optic nerve) simultaneously. Figures 6.4c-e show the Doppler OCE images at different time points of the wave propagation. It is noted that the wave traveled through the ONH region at a much faster speed, reaching the end of the optic nerve region before getting through half the distance of the peripheral retina region. In order to better analyze the difference, an en face projection of the propagation is shown in figure 6.4f, where the x-axis corresponds to the b-scan location and y-axis is the time. By measuring the ratio of the distance versus time, the velocity of the peripheral retina region was 7.9 m/s, which correlates to a stiffness of 187 kPa. The ONH region had a shear wave velocity of 27.9 m/s, and a stiffness of 2.34 MPa.

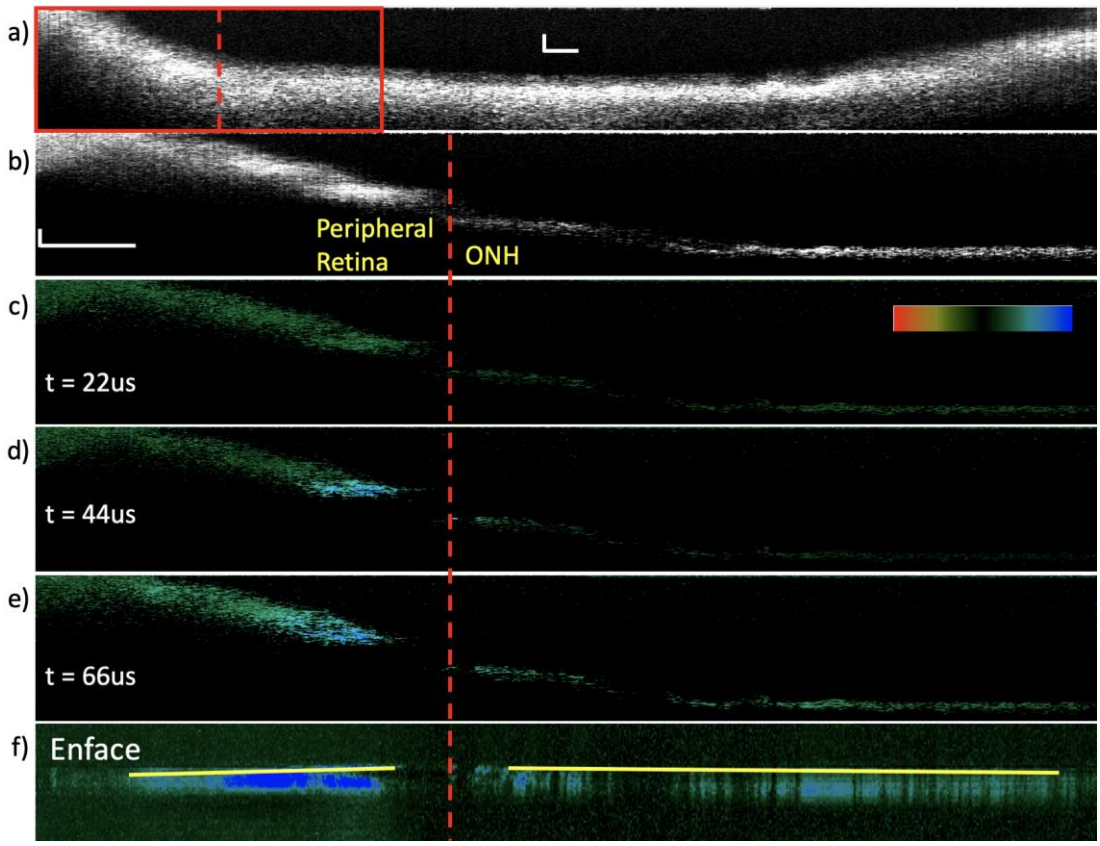

Figure 6.4 Confocal shear wave ARF-OCE results for the optic nerve head (ONH) and adjacent peripheral retina. a) OCT image of optic nerve head region. Red box is magnified in figures b-f. b) OCT image where the shear wave was applied axially at the dotted red line, to the right is the ONH region and left is the peripheral retina. Doppler OCT figures c) 22 us, d) 44 us, and e) 66 us after shear wave is induced. F) En face projection of shear wave propagation over time. Scale bar = 200 um.

The preliminary results confirm the feasibility of using the confocal shear wave ARF-OCE approach to quantify the mechanical elasticity of the ONH to characterize and better understand the mechanisms of glaucoma. For the next step, we propose to set up a simple system to alter the intraocular pressure (IOP), and conduct both *in-vivo* and *ex-vivo* experiments to detect the stiffness of the optic nerve region while controlling the IOP.

8.4 Future directions: Single-shot shear wave ARF-OCE

The current confocal shear wave OCE method successfully reduces the exposure of the tissue to the excitation source compared to compressional wave imaging and modulation methods. However, due to safety concerns with ARF excitation force on the fragile layers of the retina, a future direction is to further reduce the exposure by using a single-shot shear wave excitation pulse. This requires a high image acquisition speed, which has been made possible by the recent development of MHz swept source lasers. Since we have shown through the phase quantification studies that the phase stability of swept source lasers is comparable to that of broadband lasers, this opens up the door for utilizing the MHz swept source lasers in the phase-resolved Doppler imaging and elasticity detection.

The proposed excitation scheme is depicted below in figure 6.5. A single shot ARF beam is exerted on the sample, causing the propagation of shear wave along the x and y axes. With a MHz A-line imaging speed, it is possible to perform fast axis scanning across the entire OCT field of view and calculate the shear wave velocity at each spatial location. With this information, it is possible to obtain an elasticity map of the tissue with a single excitation pulse. This technique will be crucial in the clinical translation of the ARF-OCE technology, due to its safe exposure levels and fast imaging time.

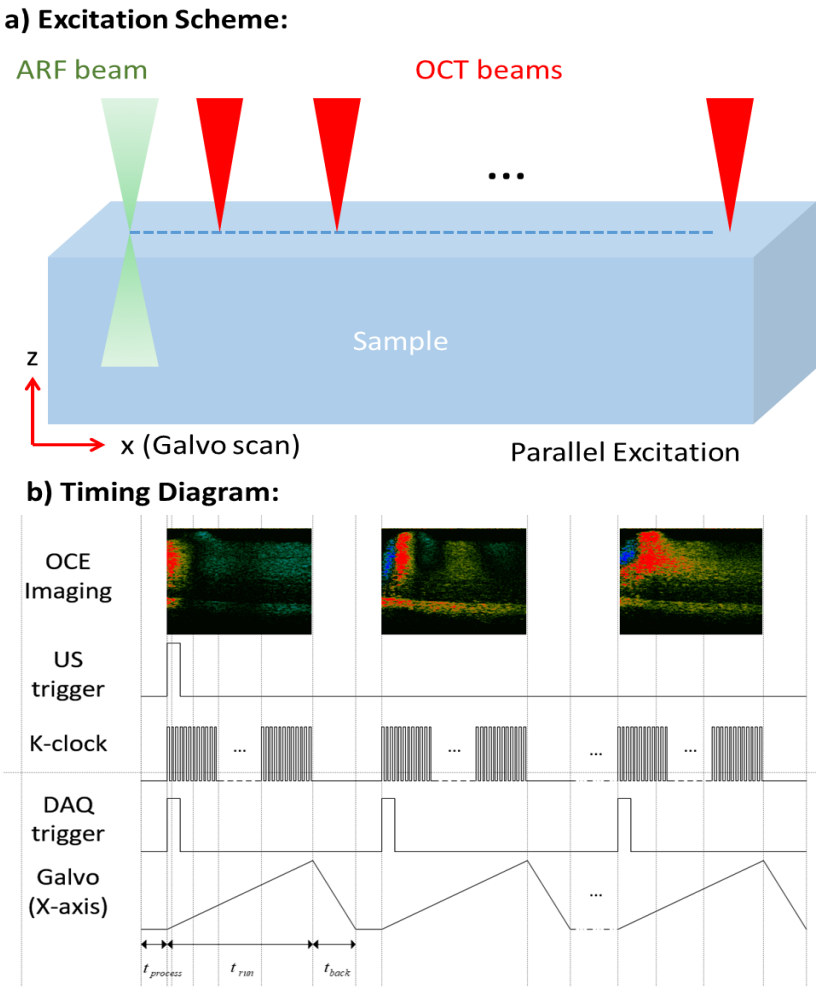

Figure 6.5 Scanning scheme of shear wave tracking in 2D space. (a) Schematic of the ARF excitation and OCT detection. The acoustic force is parallel to the OCT detection beam, and the OCT B-scan is performed along the X axis. (b) Timing diagram

8.5 Summary

This Ph.D. dissertation demonstrated the developments of PRD-OCT systems to provide potential tools for the unmet needs in the field of diagnostic biomedical imaging. Simulations and preliminary clinical studies have revealed early indicators for many irreversible diseases, such as AMD, glaucoma, and ciliary disorder, which cannot be accessed or sufficiently resolved

with traditional method but may be visualized by PRD-OCT. Since PRD-OCT provides micron scale resolution, sub-nanometer displacement sensitivity, depth resolved imaging, and the capability for *in-vivo* investigation, it can be a perfect fit for applications on ocular and ciliated tissue.

According to the principle of PRD-OCT, there are many tradeoffs between its imaging parameters, and it is thereby necessary to analyze the requirements of the applications, identify the priorities of different parameters and strategically design the system to meet the demands. Ocular applications requires micron axial resolution and sufficient imaging depth to encompass the entire ocular layers, while imaging on ciliary activity demands cellular level lateral resolution, fast imaging speed, but does not need depth information. Both of the applications require ultra-sensitive motion detection, which can be sufficiently provided by a phase sensitive PRD-OCT system.

Based on the understandings of these particular applications, we have designed and developed an broadband laser based ARF-OCE system to quantitatively assess the mechanical property of the *in-vivo* posterior eye for the first time. However, the *in-vivo* results have revealed that the speed of the broadband laser based system is not sufficient even for the ocular application. Therefore, we have tried to optimize the imaging speed by using a swept source laser to drive the system. The validation study has suggested that swept source laser can provide faster imaging speed than continuous laser while still maintain a comparable performance on other imaging parameters. This conclusion leads us to develop the SS-SEIM system to visualize the spatial ciliary activity. The system is able to resolve the cellular level periodically ciliary activity at an enface plane, and

has demonstrated the first spatial mapping of the ciliary beating frequency to the best of our knowledge.

Although both the ARF-OCE and SS-SEIM system has been successfully validated through the experiments, there are still few drawbacks that need to be overcome for clinical translations. For ARF-OCE technique, we propose to use a super-fast swept source laser to achieve cross-sectional shear wave visualization with one excitation shot. This will allows us to reduce the radiation dosage and enables the visualization of the fast shear wave propagation in stiff ocular layer. Additionally, we would like to utilize the current ARF-OCE technique to investigate the optical nerve head tissue and study the role of its mechanical property in the pathology of glaucoma. For SS-SEIM system, a rigid endoscope and an automatic control method are designed to allows for *in-vivo* study in nasal cavity and get rid of the bulk motion. The optimization will enables the clinical trials of this technique and provide a powerful tool for the early diagnosis of ciliary disorder.

References

1. Jager RD, Mieler WF, Miller JW. Age-related macular degeneration. New England Journal of Medicine. 2008;358(24):2606-17.
2. Bressler NM, Bressler SB, Fine SL. Age-related macular degeneration. Survey of ophthalmology. 1988;32(6):375-413.
3. Lim LS, Mitchell P, Seddon JM, Holz FG, Wong TY. Age-related macular degeneration. The Lancet. 2012;379(9827):1728-38.
4. Chakravarthy U, Evans J, Rosenfeld PJ. Age related macular degeneration. Bmj. 2010;340:c981.
5. Hee MR, Baumal CR, Puliafito CA, Duker JS, Reichel E, Wilkins JR, Coker JG, Schuman JS, Swanson EA, Fujimoto JG. Optical coherence tomography of age-related macular degeneration and choroidal neovascularization. Ophthalmology. 1996;103(8):1260-70.
6. la Cour M, Kiilgaard JF, Nissen MH. Age-related macular degeneration. Drugs & aging. 2002;19(2):101-33.
7. Krishnan L, Hoying JB, Nguyen H, Song H, Weiss JA. Interaction of angiogenic microvessels with the extracellular matrix. American Journal of Physiology-Heart and Circulatory Physiology. 2007;293(6):H3650-H8.
8. Chen K, Rowley AP, Weiland JD. Elastic properties of porcine ocular posterior soft tissues. Journal of Biomedical Materials Research Part A: An Official Journal of The Society for Biomaterials, The Japanese Society for Biomaterials, and The Australian Society for Biomaterials and the Korean Society for Biomaterials. 2010;93(2):634-45.
9. Sarks S, Arnold J, Killingsworth M, Sarks J. Early drusen formation in the normal and aging eye and their relation to age related maculopathy: a clinicopathological study. British Journal of Ophthalmology. 1999;83(3):358-68.
10. Friberg TR, Lace JW. A comparison of the elastic properties of human choroid and sclera. Experimental eye research. 1988;47(3):429-36.
11. Quigley HAJBjoo. Number of people with glaucoma worldwide1996;80(5):389-93.
12. Quigley HAJIo, science v. Glaucoma: macrocosm to microcosm the Friedenwald lecture2005;46(8):2663-70.
13. Quigley HA, Broman ATJBjoo. The number of people with glaucoma worldwide in 2010 and 20202006;90(3):262-7.
14. Burgoyne CF, Downs JCJJog. Premise and prediction–how optic nerve head biomechanics underlies the susceptibility and clinical behavior of the aged optic nerve head2008;17(4):318.
15. Nguyen TD, Ethier CRJEer. Biomechanical assessment in models of glaucomatous optic neuropathy2015;141:125-38.
16. Sigal IA, Ethier CRJEer. Biomechanics of the optic nerve head2009;88(4):799-807.
17. Burgoyne CF, Downs JC, Bellezza AJ, Suh J-KF, Hart RTJPir, research e. The optic nerve head as a biomechanical structure: a new paradigm for understanding the role of IOP-related stress and strain in the pathophysiology of glaucomatous optic nerve head damage2005;24(1):39-73.
18. Sigal IA, Flanagan JG, Ethier CRJIo, science v. Factors influencing optic nerve head biomechanics2005;46(11):4189-99.

19. Sigal I, Grimm J, Schuman J, Kagemann L, Ishikawa H, Wollstein GJItomi. A method to estimate biomechanics and mechanical properties of optic nerve head tissues from parameters measurable using optical coherence tomography2014;33(6):1381-9.
20. Coudrillier B, Tian J, Alexander S, Myers KM, Quigley HA, Nguyen TDJIo, science v. Biomechanics of the human posterior sclera: age-and glaucoma-related changes measured using inflation testing2012;53(4):1714-28.
21. Girard MJ, Suh J-KF, Bottlang M, Burgoyne CF, Downs JCJIo, science v. Biomechanical changes in the sclera of monkey eyes exposed to chronic IOP elevations2011;52(8):5656-69.
22. Grytz R, Fazio MA, Girard MJ, Libertiaux V, Bruno L, Gardiner S, Girkin CA, Downs JCJJotmbobm. Material properties of the posterior human sclera2014;29:602-17.
23. Fazio MA, Grytz R, Morris JS, Bruno L, Gardiner SK, Girkin CA, Downs JCJB, mechanobiology mi. Age-related changes in human peripapillary scleral strain2014;13(3):551-63.
24. Grytz R, Fazio MA, Libertiaux V, Bruno L, Gardiner S, Girkin CA, Downs JCJIo, science v. Age-and race-related differences in human scleral material properties2014;55(12):8163-72.
25. Fazio MA, Grytz R, Morris JS, Bruno L, Girkin CA, Downs JCJIo, science v. Human scleral structural stiffness increases more rapidly with age in donors of African descent compared to donors of European descent2014;55(11):7189-98.
26. Ethier CR, Johnson M, Ruberti JJARBE. Ocular biomechanics and biotransport2004;6:249-73.
27. Girard MJ, Strouthidis NG, Desjardins A, Mari JM, Ethier CRJJoTRSI. In vivo optic nerve head biomechanics: performance testing of a three-dimensional tracking algorithm2013;10(87):20130459.
28. Woo SL, Kobayashi A, Lawrence C, Schlegel WJAobe. Mathematical model of the corneo-scleral shell as applied to intraocular pressure-volume relations and applanation tonometry1972;1(1):87-98.
29. Gennisson J-L, Deffieux T, Fink M, Tanter MJD, imaging i. Ultrasound elastography: principles and techniques2013;94(5):487-95.
30. Sun C, Standish BA, Yang VXJJobo. Optical coherence elastography: current status and future applications2011;16(4):043001.
31. Manduca A, Oliphant TE, Dresner MA, Mahowald J, Kruse SA, Amromin E, Felmlee JP, Greenleaf JF, Ehman RLJMia. Magnetic resonance elastography: non-invasive mapping of tissue elasticity2001;5(4):237-54.
32. Greenleaf JF, Fatemi M, Insana MJArobe. Selected methods for imaging elastic properties of biological tissues2003;5(1):57-78.
33. Zhu J, Yu J, Qu Y, He Y, Li Y, Yang Q, Huo T, He X, Chen ZJOl. Coaxial excitation longitudinal shear wave measurement for quantitative elasticity assessment using phase-resolved optical coherence elastography2018;43(10):2388-91.
34. Qi W, Li R, Ma T, Kirk Shung K, Zhou Q, Chen ZJApl. Confocal acoustic radiation force optical coherence elastography using a ring ultrasonic transducer2014;104(12):123702.
35. Li J, Wang S, Manapuram RK, Singh M, Menodiado FM, Aglyamov S, Emelianov SY, Twa MD, Larin KVJJobo. Dynamic optical coherence tomography measurements of elastic

wave propagation in tissue-mimicking phantoms and mouse cornea in vivo2013;18(12):121503.
36. He Y, Qu Y, Zhu J, Zhang Y, Saidi A, Ma T, Zhou Q, Chen ZJIJoSTiQE. Confocal Shear Wave Acoustic Radiation Force Optical Coherence Elastography for Imaging and Quantification of theIn VivoPosterior Eye2019;25(1):1-7.
37. Ma T, Qian X, Chiu CT, Yu M, Jung H, Tung Y-S, Shung KK, Zhou QJQiim, surgery. High-resolution harmonic motion imaging (HR-HMI) for tissue biomechanical property characterization2015;5(1):108.
38. Qi W, Chen R, Chou L, Liu G, Zhang J, Zhou Q, Chen ZJJobo. Phase-resolved acoustic radiation force optical coherence elastography2012;17(11):110505.
39. Qi W, Li R, Ma T, Li J, Kirk Shung K, Zhou Q, Chen ZJAPL. Resonant acoustic radiation force optical coherence elastography2013;103(10):103704.
40. Qu Y, He Y, Saidi A, Xin Y, Zhou Y, Zhu J, Ma T, Silverman RH, Minckler DS, Zhou QJIo, science v. In vivo elasticity mapping of posterior ocular layers using acoustic radiation force optical coherence elastography2018;59(1):455-61.
41. Qu Y, He Y, Zhang Y, Ma T, Zhu J, Miao Y, Dai C, Humayun M, Zhou Q, Chen ZJBOE. Quantified elasticity mapping of retinal layers using synchronized acoustic radiation force optical coherence elastography2018;9(9):4054-63.
42. Qu Y, Ma T, He Y, Zhu J, Dai C, Yu M, Huang S, Lu F, Shung KK, Zhou QJIJoSTiQE. Acoustic radiation force optical coherence elastography of corneal tissue2016;22(3):288-94.
43. Zhu J, Qi L, Miao Y, Ma T, Dai C, Qu Y, He Y, Gao Y, Zhou Q, Chen ZJSr. 3D mapping of elastic modulus using shear wave optical micro-elastography2016;6:35499.
44. Zhu J, Qu Y, Ma T, Li R, Du Y, Huang S, Shung KK, Zhou Q, Chen ZJOl. Imaging and characterizing shear wave and shear modulus under orthogonal acoustic radiation force excitation using OCT Doppler variance method2015;40(9):2099-102.
45. Agladioglu K, Pekel G, Altintas Kasikci S, Yagci R, Kiroglu YJTBjor. An evaluation of ocular elasticity using real-time ultrasound elastography in primary open-angle glaucoma2016;89(1060):20150429.
46. Özen Ö, Özer MA, Tosun A, Özen SJMu. Evaluation of the optic nerve and scleral-choroidal-retinal layer with ultrasound elastography in glaucoma and physiological optic nerve head cupping. Medical ultrasonography. 2018;20(1):76-9.
47. Varghese TJUc. Quasi-static ultrasound elastography2009;4(3):323.
48. Song S, Le NM, Huang Z, Shen T, Wang RKJOl. Quantitative shear-wave optical coherence elastography with a programmable phased array ultrasound as the wave source2015;40(21):5007-10.
49. Sebag F, Vaillant-Lombard J, Berbis J, Griset V, Henry J, Petit P, Oliver CJTJoCE, Metabolism. Shear wave elastography: a new ultrasound imaging mode for the differential diagnosis of benign and malignant thyroid nodules2010;95(12):5281-8.
50. Evans A, Whelehan P, Thomson K, McLean D, Brauer K, Purdie C, Jordan L, Baker L, Thompson AJBcr. Quantitative shear wave ultrasound elastography: initial experience in solid breast masses2010;12(6):R104.
51. Arda K, Ciledag N, Aktas E, Arıbas BK, Köse KJAJoR. Quantitative assessment of normal soft-tissue elasticity using shear-wave ultrasound elastography2011;197(3):532-6.
52. Zaleska-DorobiszA U, KaczorowskiB K, PawluśB A, PuchalskaB A, InglotB MJb. Ultrasound elastography–review of techniques and its clinical applications2013;6:10-4.

53. Wang S, Larin KVJJob. Optical coherence elastography for tissue characterization: a review2015;8(4):279-302.
54. Kennedy BF, Kennedy KM, Sampson DDJIJoSTiQE. A review of optical coherence elastography: fundamentals, techniques and prospects2014;20(2):272-88.
55. Dikici AS, Mihmanli I, Kilic F, Ozkok A, Kuyumcu G, Sultan P, Samanci C, Yilmaz MH, Rafiee B, Tamcelik NJIJoR. In vivo evaluation of the biomechanical properties of optic nerve and peripapillary structures by ultrasonic shear wave elastography in glaucoma2016;13(2).
56. Vural M, Acar D, Toprak U, Alp MN, Köz ÖG, Sayin B, Abat GKJMu. The evaluation of the retrobulbar orbital fat tissue and optic nerve with strain ratio elastography2015;17(1):45-8.
57. İnal M, Tan S, Yumusak EM, Şahan MH, Alpua M, Örnek KJMu. Evaluation of the optic nerve using strain and shear wave elastography in patients with multiple sclerosis and healthy subjects2017;19(1):39-44.
58. Zhao Y, Chen Z, Saxer C, Xiang S, de Boer JF, Nelson JSJOl. Phase-resolved optical coherence tomography and optical Doppler tomography for imaging blood flow in human skin with fast scanning speed and high velocity sensitivity2000;25(2):114-6.
59. Zhao Y, Chen Z, Saxer C, Shen Q, Xiang S, de Boer JF, Nelson JSJOL. Doppler standard deviation imaging for clinical monitoring of in vivo human skin blood flow2000;25(18):1358-60.
60. Chen Z, Milner TE, Srinivas S, Wang X, Malekafzali A, van Gemert MJ, Nelson JSJOl. Noninvasive imaging of in vivo blood flow velocity using optical Doppler tomography1997;22(14):1119-21.
61. Chen Z, Milner TE, Dave D, Nelson JSJOl. Optical Doppler tomographic imaging of fluid flow velocity in highly scattering media1997;22(1):64-6.
62. Roy AS, Kurian M, Matalia H, Shetty RJJotmbobm. Air-puff associated quantification of non-linear biomechanical properties of the human cornea in vivo2015;48:173-82.
63. Ambroziński Ł, Song S, Yoon SJ, Pelivanov I, Li D, Gao L, Shen TT, Wang RK, O'Donnell MJSr. Acoustic micro-tapping for non-contact 4D imaging of tissue elasticity2016;6:38967.
64. Knowles MR, Boucher RCJTJoci. Mucus clearance as a primary innate defense mechanism for mammalian airways2002;109(5):571-7.
65. King MJPrr. Physiology of mucus clearance2006;7:S212-S4.
66. Liu L, Chu KK, Houser GH, Diephuis BJ, Li Y, Wilsterman EJ, Shastry S, Dierksen G, Birket SE, Mazur MJPo. Method for quantitative study of airway functional microanatomy using micro-optical coherence tomography2013;8(1):e54473.
67. Ellerman A, Bisgaard HJERJ. Longitudinal study of lung function in a cohort of primary ciliary dyskinesia1997;10(10):2376-9.
68. Smith CM, Djakow J, Free RC, Djakow P, Lonnen R, Williams G, Pohunek P, Hirst RA, Easton AJ, Andrew PWJC. ciliaFA: a research tool for automated, high-throughput measurement of ciliary beat frequency using freely available software2012;1(1):14.
69. Puybareau E, Talbot H, Pelle G, Louis B, Papon J-F, Coste A, Najman L, editors. A regionalized automated measurement of ciliary beating frequency. 2015 IEEE 12th International Symposium on Biomedical Imaging (ISBI); 2015: IEEE.
70. Dalhamn T, Rylander RJN. Frequency of ciliary beat measured with a photo-sensitive cell1962;196(4854):592.

71. Chilvers MA, O'callaghan CJT. Analysis of ciliary beat pattern and beat frequency using digital high speed imaging: comparison with the photomultiplier and photodiode methods2000;55(4):314-7.
72. Ezzati M, Djahanbakhch O, Arian S, Carr BRJJoar, genetics. Tubal transport of gametes and embryos: a review of physiology and pathophysiology2014;31(10):1337-47.
73. Pauerstein CJ, Woodruff JD, Zachary ASJO, survey g. Factors influencing physiologic activities in the fallopian tube; the anatomy, physiology, and pharmacology of tubal transport1968;23(3):215-43.
74. Croxatto HBJRbo. Physiology of gamete and embryo transport through the fallopian tube2002;4(2):160-9.
75. Ikemoto Y, Kuroda K, Kuribayashi Y, Inoue M. Tubal Function Abnormalities with Tubal Patency in Unexplained Infertility. Treatment Strategy for Unexplained Infertility and Recurrent Miscarriage: Springer; 2018. p. 19-31.
76. Kumakiri J, Ozaki R, Takeda S, Malvasi A, Tinelli A. Tubal Pregnancy. Management and Therapy of Early Pregnancy Complications: Springer; 2016. p. 69-104.
77. Li S, Winuthayanon WJJoE. Oviduct: roles in fertilization and early embryo development2017;232(1):R1-R26.
78. Lyons R, Saridogan E, Djahanbakhch OJHru. The reproductive significance of human Fallopian tube cilia2006;12(4):363-72.
79. Panelli DM, Phillips CH, Brady PCJFR, Practice. Incidence, diagnosis and management of tubal and nontubal ectopic pregnancies: a review2015;1(1):15.
80. Halbert S, Tam P, Blandau RJS. Egg transport in the rabbit oviduct: the roles of cilia and muscle1976;191(4231):1052-3.
81. Halbert SA, Becker DR, Szal SEJBor. Ovum transport in the rat oviductal ampulla in the absence of muscle contractility1989;40(6):1131-6.
82. Zhao W, Zhu Q, Yan M, Li C, Yuan J, Qin G, Zhang JJC, Pharmacology E, Physiology. Levonorgestrel decreases cilia beat frequency of human fallopian tubes and rat oviducts without changing morphological structure2015;42(2):171-8.
83. Talbot P, DiCarlantonio G, Knoll M, Gomez CJBor. Identification of cigarette smoke components that alter functioning of hamster (Mesocricetus auratus) oviducts in vitro1998;58(4):1047-53.
84. Shi D, Komatsu K, Uemura T, Fujimori TJGtc. Analysis of ciliary beat frequency and ovum transport ability in the mouse oviduct2011;16(3):282-90.
85. Lyons R, Saridogan E, Djahanbakhch OJHR. The effect of ovarian follicular fluid and peritoneal fluid on Fallopian tube ciliary beat frequency2005;21(1):52-6.
86. Liao SB, Ho J, Tang FJR. Adrenomedullin increases ciliary beat frequency and decreases muscular contraction in the rat oviduct2011;141(3):367-72.
87. Bylander A, Nutu M, Wellander R, Goksör M, Billig H, Larsson DJJRB, Endocrinology. Rapid effects of progesterone on ciliary beat frequency in the mouse fallopian tube2010;8(1):48.
88. Knoll M, Shaoulian R, Magers T, Talbot PJBor. Ciliary beat frequency of hamster oviducts is decreased in vitro by exposure to solutions of mainstream and sidestream cigarette smoke1995;53(1):29-37.
89. Lyons R, Djahanbakhch O, Mahmood T, Saridogan E, Sattar S, Sheaff M, Naftalin A, Chenoy RJHR. Fallopian tube ciliary beat frequency in relation to the stage of menstrual cycle and anatomical site2002;17(3):584-8.

90. Nakahari T, Nishimura A, Shimamoto C, Sakai A, Kuwabara H, Nakano T, Tanaka S, Kohda Y, Matsumura H, Mori HJBr. The regulation of ciliary beat frequency by ovarian steroids in the guinea pig Fallopian tube: interactions between oestradiol and progesterone2011;32(5):321-8.
91. Parrilla E, Armengot M, Mata M, Cortijo J, Riera J, Hueso JL, Moratal D, editors. Optical flow method in phase-contrast microscopy images for the diagnosis of primary ciliary dyskinesia through measurement of ciliary beat frequency. Preliminary results. 2012 9th IEEE International Symposium on Biomedical Imaging (ISBI); 2012: IEEE.
92. Keenan M, Tate TH, Kieu K, Black JF, Utzinger U, Barton JKJBoe. Design and characterization of a combined OCT and wide field imaging falloposcope for ovarian cancer detection2017;8(1):124-36.
93. Wang S, Burton JC, Behringer RR, Larina IVJSr. In vivo micro-scale tomography of ciliary behavior in the mammalian oviduct2015;5:13216.
94. Wang S, Larina IV. In Vivo Imaging of the Mouse Reproductive Organs, Embryo Transfer, and Oviduct Cilia Dynamics Using Optical Coherence Tomography. Mouse Embryogenesis: Springer; 2018. p. 53-62.
95. Wang S, Syed R, Grishina OA, Larina IVJJob. Prolonged in vivo functional assessment of the mouse oviduct using optical coherence tomography through a dorsal imaging window2018;11(5):e201700316.
96. Jing JC, Chen JJ, Chou L, Wong BJ, Chen ZJSr. Visualization and detection of ciliary beating pattern and frequency in the upper airway using phase resolved Doppler optical coherence tomography2017;7(1):8522.
97. Lemieux BT, Chen JJ, Jing J, Chen Z, Wong BJ, editors. Measurement of ciliary beat frequency using Doppler optical coherence tomography. International forum of allergy & rhinology; 2015: Wiley Online Library.
98. Fercher AF, Drexler W, Hitzenberger CK, Lasser TJRopip. Optical coherence tomography-principles and applications2003;66(2):239.
99. Chu KK, Unglert C, Ford TN, Cui D, Carruth RW, Singh K, Liu L, Birket SE, Solomon GM, Rowe SMJBoe. In vivo imaging of airway cilia and mucus clearance with micro-optical coherence tomography2016;7(7):2494-505.
100. Qu Y, Ma T, He Y, Yu M, Zhu J, Miao Y, Dai C, Patel P, Shung KK, Zhou QJSR. Miniature probe for mapping mechanical properties of vascular lesions using acoustic radiation force optical coherence elastography2017;7(1):4731.
101. Ilgayev O, Yelin DJOe. Phase-sensitive imaging of tissue acoustic vibrations using spectrally encoded interferometry2013;21(17):19681-9.
102. Tearney GJ, Webb R, Bouma BJOl. Spectrally encoded confocal microscopy1998;23(15):1152-4.
103. Tearney G, Shishkov M, Bouma BJOl. Spectrally encoded miniature endoscopy2002;27(6):412-4.
104. Huang D, Swanson EA, Lin CP, Schuman JS, Stinson WG, Chang W, Hee MR, Flotte T, Gregory K, Puliafito CAJs. Optical coherence tomography1991;254(5035):1178-81.
105. Fujimoto JG, Pitris C, Boppart SA, Brezinski ME. Optical coherence tomography: an emerging technology for biomedical imaging and optical biopsy. Neoplasia (New York, NY). 2000;2(1-2):9.

106. Chen Z, Milner TE, Srinivas S, Wang X, Malekafzali A, van Gemert MJ, Nelson JSJOl. Noninvasive imaging of in vivo blood flow velocity using optical Doppler tomography. Optics letters. 1997;22(14):1119-21.
107. Chen Z, Zhao Y, Srinivas SM, Nelson JS, Prakash N, Frostig RDJIJoSTiQE. Optical doppler tomography1999;5(4):1134-42.
108. Li J, Ma T, Mohar D, Steward E, Yu M, Piao Z, He Y, Shung KK, Zhou Q, Patel PMJSr. Ultrafast optical-ultrasonic system and miniaturized catheter for imaging and characterizing atherosclerotic plaques in vivo2015;5:18406.
109. Miao Y, Jing JC, Desai V, Mahon SB, Brenner M, Veress LA, White CW, Chen ZJSr. Automated 3D segmentation of methyl isocyanate-exposed rat trachea using an ultra-thin, fully fiber optic optical coherence endoscopic probe2018;8(1):8713.
110. Jing JC, Chen JJ, Chou L, Wong BJ, Chen ZJSr. Visualization and detection of ciliary beating pattern and frequency in the upper airway using phase resolved Doppler optical coherence tomography. Scientific reports. 2017;7(1):8522.
111. Han Z, Li J, Singh M, Wu C, Liu C-h, Wang S, Idugboe R, Raghunathan R, Sudheendran N, Aglyamov SR. Quantitative methods for reconstructing tissue biomechanical properties in optical coherence elastography: a comparison study. Physics in Medicine & Biology. 2015;60(9):3531.
112. He Y, Qu Y, Zhu J, Zhang Y, Saidi A, Ma T, Zhou Q, Chen ZJIJoSTiQE. Confocal Shear Wave Acoustic Radiation Force Optical Coherence Elastography for Imaging and Quantification of theIn VivoPosterior Eye. IEEE Journal of Selected Topics in Quantum Electronics. 2019;25(1):1-7.
113. Qu Y, He Y, Saidi A, Xin Y, Zhou Y, Zhu J, Ma T, Silverman RH, Minckler DS, Zhou QJIo, science v. In vivo elasticity mapping of posterior ocular layers using acoustic radiation force optical coherence elastography. Investigative ophthalmology & visual science. 2018;59(1):455-61.
114. Schmitt JM. Optical coherence tomography (OCT): a review. IEEE Journal of selected topics in quantum electronics. 1999;5(4):1205-15.
115. Jang I-K, Bouma BE, Kang D-H, Park S-J, Park S-W, Seung K-B, Choi K-B, Shishkov M, Schlendorf K, Pomerantsev E. Visualization of coronary atherosclerotic plaques in patients using optical coherence tomography: comparison with intravascular ultrasound. Journal of the American College of Cardiology. 2002;39(4):604-9.
116. Pagnoni A, Knuettel A, Welker P, Rist M, Stoudemayer T, Kolbe L, Sadiq I, Kligman A. Optical coherence tomography in dermatology. Skin Research and Technology. 1999;5(2):83-7.
117. Qu Y, Ma T, He Y, Zhu J, Dai C, Yu M, Huang S, Lu F, Shung KK, Zhou QJIJoSTiQE. Acoustic radiation force optical coherence elastography of corneal tissue. IEEE Journal of Selected Topics in Quantum Electronics. 2016;22(3):288-94.
118. Moon S, Chen Z. Phase-stability optimization of swept-source optical coherence tomography. Biomedical optics express. 2018;9(11):5280-95.
119. Yun S, Tearney G, de Boer J, Bouma B. Pulsed-source and swept-source spectral-domain optical coherence tomography with reduced motion artifacts. Optics Express. 2004;12(23):5614-24.
120. Choi W, Potsaid B, Jayaraman V, Baumann B, Grulkowski I, Liu JJ, Lu CD, Cable AE, Huang D, Duker JS. Phase-sensitive swept-source optical coherence tomography

imaging of the human retina with a vertical cavity surface-emitting laser light source. Optics letters. 2013;38(3):338-40.
121. Choma MA, Sarunic MV, Yang C, Izatt JA. Sensitivity advantage of swept source and Fourier domain optical coherence tomography. Optics express. 2003;11(18):2183-9.
122. Walther J, Mueller G, Morawietz H, Koch EJJoBO. Signal power decrease due to fringe washout as an extension of the limited Doppler flow measurement range in spectral domain optical coherence tomography2010;15(4):041511.
123. Moon S, Chen ZJBoe. Phase-stability optimization of swept-source optical coherence tomography2018;9(11):5280-95.
124. Chen Z, Milner TE, Dave D, Nelson JSJOl. Optical Doppler tomographic imaging of fluid flow velocity in highly scattering media. Optics letters. 1997;22(1):64-6.
125. Zhao Y, Chen Z, Saxer C, Xiang S, de Boer JF, Nelson JSJOl. Phase-resolved optical coherence tomography and optical Doppler tomography for imaging blood flow in human skin with fast scanning speed and high velocity sensitivity. Optics letters. 2000;25(2):114-6.
126. Qu Y, He Y, Zhang Y, Ma T, Zhu J, Miao Y, Dai C, Humayun M, Zhou Q, Chen ZJBOE. Quantified elasticity mapping of retinal layers using synchronized acoustic radiation force optical coherence elastography. Biomedical optics express. 2018;9(9):4054-63.
127. Zhang J, Rao B, Yu L, Chen Z. High-dynamic-range quantitative phase imaging with spectral domain phase microscopy. Optics letters. 2009;34(21):3442-4.
128. Liu G, Chen Z. Advances in doppler oct. Chinese Optics Letters. 2013;11(1):011702.
129. Song S, Xu J, Men S, Shen TT, Wang RKJJob. Robust numerical phase stabilization for long-range swept-source optical coherence tomography2017;10(11):1398-410.
130. Xi J, Huo L, Li J, Li X. Generic real-time uniform K-space sampling method for high-speed swept-Source optical coherence tomography. Optics express. 2010;18(9):9511-7.
131. Braaf B, Vermeer KA, Sicam VAD, van Zeeburg E, van Meurs JC, de Boer JF. Phase-stabilized optical frequency domain imaging at 1-μm for the measurement of blood flow in the human choroid. Optics express. 2011;19(21):20886-903.
132. Gora M, Karnowski K, Szkulmowski M, Kaluzny BJ, Huber R, Kowalczyk A, Wojtkowski M. Ultra high-speed swept source OCT imaging of the anterior segment of human eye at 200 kHz with adjustable imaging range. Optics Express. 2009;17(17):14880-94.
133. Kim S, Raphael PD, Oghalai JS, Applegate BE. High-speed spectral calibration by complex FIR filter in phase-sensitive optical coherence tomography. Biomedical optics express. 2016;7(4):1430-44.
134. Han Z, Li J, Singh M, Vantipalli S, Aglyamov SR, Wu C, Liu C-h, Raghunathan R, Twa MD, Larin KV. Analysis of the effect of the fluid-structure interface on elastic wave velocity in cornea-like structures by OCE and FEM. Laser Physics Letters. 2016;13(3):035602.
135. Han Z, Li J, Singh M, Wu C, Liu C-h, Raghunathan R, Aglyamov SR, Vantipalli S, Twa MD, Larin KV. Optical coherence elastography assessment of corneal viscoelasticity with a modified Rayleigh-Lamb wave model. Journal of the mechanical behavior of biomedical materials. 2017;66:87-94.
136. Tearney G, Shishkov M, Bouma BJOl. Spectrally encoded miniature endoscopy. Optics letters. 2002;27(6):412-4.
137. Tearney GJ, Webb R, Bouma BJOl. Spectrally encoded confocal microscopy. Optics letters. 1998;23(15):1152-4.

138. Yelin D, Bouma B, Iftimia N, Tearney G. Three-dimensional spectrally encoded imaging. Optics letters. 2003;28(23):2321-3.
139. Yelin D, Bouma B, Rosowsky J, Tearney GJOe. Doppler imaging using spectrally-encoded endoscopy2008;16(19):14836-44.
140. Grechin S, Yelin DJOC. Imaging acoustic vibrations in an ear model using spectrally encoded interferometry2018;407:175-80.
141. Ikuta M, Do D, Kang D, Tearney GJ, Brauer JS. Spectrally encoded endoscopic probe having a fixed fiber. Google Patents; 2017.
142. Jones I, Warner M, Stevens J. Mathematical modelling of the elastic properties of retina: a determination of Young's modulus. Eye. 1992;6(6):556.
143. Litwiller DV, Lee SJ, Kolipaka A, Mariappan YK, Glaser KJ, Pulido JS, Ehman RL. MR elastography of the ex vivo bovine globe. Journal of Magnetic Resonance Imaging. 2010;32(1):44-51.
144. Detorakis ET, Drakonaki EE, Tsilimbaris MK, Pallikaris IG, Giarmenitis S. Real-time ultrasound elastographic imaging of ocular and periocular tissues: a feasibility study. Ophthalmic Surgery, Lasers and Imaging Retina. 2010;41(1):135-41.
145. Wang S, Larin KV. Shear wave imaging optical coherence tomography (SWI-OCT) for ocular tissue biomechanics. Optics letters. 2014;39(1):41-4.
146. Zhu J, Miao Y, Qi L, Qu Y, He Y, Yang Q, Chen Z. Longitudinal shear wave imaging for elasticity mapping using optical coherence elastography. Applied physics letters. 2017;110(20):201101.
147. Ford MR, Dupps WJ, Rollins AM, Roy AS, Hu Z. Method for optical coherence elastography of the cornea. Journal of biomedical optics. 2011;16(1):016005.
148. Wang S, Larin KV. Noncontact depth-resolved micro-scale optical coherence elastography of the cornea. Biomedical optics express. 2014;5(11):3807-21.
149. Razani M, Mariampillai A, Sun C, Luk TW, Yang VX, Kolios MC. Feasibility of optical coherence elastography measurements of shear wave propagation in homogeneous tissue equivalent phantoms. Biomedical optics express. 2012;3(5):972-80.
150. Huang S, Piao Z, Zhu J, Lu F, Chen Z. In vivo microvascular network imaging of the human retina combined with an automatic three-dimensional segmentation method. Journal of biomedical optics. 2015;20(7):076003.
151. Grady L. Random walks for image segmentation. IEEE Transactions on Pattern Analysis & Machine Intelligence. 2006(11):1768-83.
152. Cohen E, Agrawal A, Connors M, Hansen B, Charkhkar H, Pfefer J. Optical coherence tomography imaging of retinal damage in real time under a stimulus electrode. Journal of neural engineering. 2011;8(5):056017.
153. Potsaid B, Jayaraman V, Fujimoto JG, Jiang J, Heim PJ, Cable AE, editors. MEMS tunable VCSEL light source for ultrahigh speed 60kHz-1MHz axial scan rate and long range centimeter class OCT imaging. Optical Coherence Tomography and Coherence Domain Optical Methods in Biomedicine XVI; 2012: International Society for Optics and Photonics.
154. Eigenwillig CM, Biedermann BR, Palte G, Huber RJOe. K-space linear Fourier domain mode locked laser and applications for optical coherence tomography2008;16(12):8916-37.
155. Grechin S, Yelin D. Imaging acoustic vibrations in an ear model using spectrally encoded interferometry. Optics Communications. 2018;407:175-80.

156. Ilgayev O, Yelin D. Phase-sensitive imaging of tissue acoustic vibrations using spectrally encoded interferometry. Optics express. 2013;21(17):19681-9.
157. Yelin D, Bouma B, Rosowsky J, Tearney G. Doppler imaging using spectrally-encoded endoscopy. Optics express. 2008;16(19):14836-44.
158. Walther J, Mueller G, Morawietz H, Koch E. Signal power decrease due to fringe washout as an extension of the limited Doppler flow measurement range in spectral domain optical coherence tomography. Journal of Biomedical Optics. 2010;15(4):041511.
159. De Boer JF, Leitgeb R, Wojtkowski M. Twenty-five years of optical coherence tomography: the paradigm shift in sensitivity and speed provided by Fourier domain OCT. Biomedical optics express. 2017;8(7):3248-80.
160. Yun S-H, Tearney GJ, de Boer JF, Iftimia N, Bouma BE. High-speed optical frequency-domain imaging. Optics express. 2003;11(22):2953-63.
161. Frohock JI, Wijkstrom-Frei C, Salathe MJJoAP. Effects of albuterol enantiomers on ciliary beat frequency in ovine tracheal epithelial cells2002;92(6):2396-402.
162. Devalia J, Sapsford R, Rusznak C, Toumbis M, Davies RJPp. The effects of salmeterol and salbutamol on ciliary beat frequency of cultured human bronchial epithelial cells, in vitro1992;5(4):257-63.
163. Seybold Z, Mariassy A, Stroh D, Kim C, Gazeroglu H, Wanner AJJoap. Mucociliary interaction in vitro: effects of physiological and inflammatory stimuli1990;68(4):1421-6.